

8. SITE 861¹

Shipboard Scientific Party²

HOLE 861A

Date occupied: 17 December 1991, 0300³
Date departed: 17 December 1991, 1015
Time on hole: 7 hr, 15 min
Position: 45°51.025'S, 75°41.531'W
Distance between rig floor and sea level (m): 11.31
Total depth (rig floor; m): 1677.5
Number of cores (including cores with no recovery): 1
Total length of cored section (m): 9.5
Total core recovered (m): 9.5
Core recovery (%): 100.0
Oldest sediment recovered:
Depth (mbsf): 9.5
Nature: Silty clay
Youngest age: Quaternary
Oldest age: Quaternary
Comments: Overshot mudline

HOLE 861B

Date occupied: 17 December 1991, 1015
Date departed: 17 December 1991, 1045
Time on hole: 30 min
Position: 45°51.025' S, 75°41.531' W
Distance between rig floor and sea level (m): 11.31
Total depth (rig floor; m): 1672.5
Number of cores (including cores with no recovery): 1
Total length of cored section (m): 9.5
Total core recovered (m): 9.92
Core recovery (%): 105.2
Nature: Silty clay
Youngest age: Quaternary
Oldest age: Quaternary
Comments: Overshot mudline

HOLE 861C

Date occupied: 17 December 1991, 1045
Date departed: 20 December 1991, 1530
Time on hole: 3 days, 4 hr, 45 min
Position: 45°51.025' S, 75°41.531' W
Bottom felt (rig floor; m, drill-pipe measurement): 1663.5

Distance between rig floor and sea level (m): 11.31
Water depth (drill-pipe measurement from sea level (m): 1652.2
Total depth (rig floor; m): 2016.6
Penetration (m): 353.1
Number of cores (including cores with no recovery): 41
Total length of cored section (m): 353.1
Total core recovered (m): 202.17
Core recovery (%): 57.3
Oldest sediment recovered:
Depth (mbsf): 353.1
Nature: Silty claystone
Age: late Pliocene

HOLE 861D

Date occupied: 20 December 1991, 1530
Date departed: 22 December 1991, 2100
Time on hole: 2 days, 5 hr, 30 min
Position: 45°51.008'S, 75°41.499'W
Bottom felt (rig floor; m, drill-pipe measurement): 1663.5
Distance between rig floor and sea level (m): 11.31
Water depth (drill-pipe measurement from sea level (m): 1652.2
Total depth (rig floor; m): 2159.8
Penetration (m): 496.3
Number of cores (including cores with no recovery): 16
Total length of cored section (m): 154.0
Total core recovered (m): 40.65
Core recovery (%): 26.4
Oldest sediment recovered:
Depth (mbsf): 496.3
Nature: Claystone
Age: late Pliocene
Comments: Washed from 0-342.3 mbsf.

Principal Results: Drilling at Site 861 penetrated and sampled forearc basin strata on the middle trench slope of the South American continental margin. These are underlain by deformed sediments that may represent the top of an eastward extension of the accretionary wedge already intersected at Sites 859 and 860.

Three lithologic units were identified at Site 861. Lithologic Unit I was intersected between 0 and 43.8 mbsf. It consists of Quaternary silty clays and clayey silts, containing nannofossils. The depositional environment is one of hemipelagic sedimentation, interrupted by inflow of turbidites with hemipelagic tops. Subunit IIA was cored from 43.8 to 208.9 mbsf and is composed of silty clays and clayey silts of late Pliocene and Pleistocene age that contains intercalations of silt, sand, and gravel layers. This unit has a transitional boundary with Subunit IIB that ranges from 208.9 to 351.9 mbsf. Subunit IIB consists of upper Pliocene claystones and graded siltstones with intercalations of matrix-supported conglomerates. The boundary between Subunits IIA and IIB is not determined by a marked change in rock composition, facies, or depositional environment, but is coincident with a downhole increase in the degree of lithification. The deposition of the sediments of Unit II is in an environment closer to the source area than

¹ Behrmann, J.H., Lewis, S.D., Musgrave, R.J., et al., 1992. *Proc. ODP, Init. Repts.*, 141: College Station, TX (Ocean Drilling Program).

² Shipboard Scientific Party is as given in the list of participants preceding the contents.

³ All times are local, UTC - 3 hr.

that of Unit I, mainly suggested by the presence of coarser clastics and intraformational conglomerates. Lithologic Unit III was cored from 351.9 to 496.3 mbsf, and it consists of hard silty claystone to clayey siltstone. Unit III reflects fine-grained hemipelagic sedimentation with very distal turbidites.

Microfossil preservation in the sediment at Site 861 is poor, but better than at Sites 859 and 860. Pleistocene ages were determined for cores to 168 mbsf. The boundary between lower Pleistocene and upper Pleistocene sediments has been tentatively located at 120 mbsf (nannofossil Zones NN20/NN15). The base of the lower Pleistocene sequence was intersected at 168 mbsf. Below 168 mbsf, there is an apparently continuous upper Pliocene section down to total depth (TD) at 496.3 mbsf.

A reliable evaluation of the magnetostratigraphic data is not possible. Normally polarized overprinting obscures most of the record. However, reversed polarity overprinting, seen near TD in the broken formation, indicates that overprinting mechanisms other than viscous remagnetization operated. A distinct positive anomaly of magnetic susceptibility was found at about 45 mbsf. This anomaly correlates with a high-density, perhaps magnetite-bearing sand layer.

The sediments recovered at Site 861 can be subdivided into three structural domains. Domain I (0–210 mbsf) has horizontal to gently inclined bedding, with the development of an incipient fissility in clay-rich materials below 150 mbsf. Domain II (210–390 mbsf) has gently to moderately inclined sedimentary beds, and isolated deformation bands are found. Domain III (390–496.3 mbsf) has the characteristics of “broken formation” with abundant deformation bands and stratal disruption, similar to the structural associations found in the lower sections of Sites 859 and 860.

Porosities of the sediments show an almost linear downhole decrease from an average 60% near the mudline to about 35% at terminal depth. Anomalously low porosities are found associated with sands near 45 mbsf, and a small downhole offset toward lower porosities is observed at the boundary between lithologic Subunits IIA and IIB (208.9 mbsf). Grain densities show a constant downhole average of 2.75 g/cm³. *P*-wave velocities between about 1.8 and 2.0 km/s are found on cores in the depth range of 250–350 mbsf, and velocities between about 2.1 and 2.45 km/s are found at 460–490 mbsf.

Chemical analyses of interstitial waters and WSTP samples gave no indication of the presence of stable gas hydrates in the form of salinity and chlorinity minima. Generally, interstitial waters at Site 861 are enriched in Na and Cl concentrations, with a maximum of 15% above seawater near terminal depth. Ca contents in the upper 200 mbsf are lower than seawater, perhaps indicating Ca removal in this section by formation of authigenic calcite. A marked discontinuity in Ca content is found at 200 mbsf, below which Ca increased to 16 mM at TD. A maximum in Mg content at 60 mbsf may be related to volcanic ash found in the section at this depth. Sulfate contents are zero or very low, with 10%–15% of seawater concentrations below 200 mbsf. Mg and K profiles suggest that there is a sink for these two elements below terminal depth of the borehole, consistent with alkaline sericitization of continental basement and perhaps exchange with continental saline groundwaters.

Headspace and vacutainer analyses of gases trapped in the core liner provide evidence for a dominantly biogenic gas source down to 200 mbsf. Below this depth, the methane/ethane ratio drops to values between 100 and 1000, indicating a contribution of thermogenic gas in the sediment. The composition of gases and condensates here is very similar to those in the deeper parts of Holes 859B and 860B. Total organic carbon contents are generally lower than 0.5%, except for the upper 20 mbsf with contents between 0.5% and 1.0%. The solid organic matter is immature and has a terrigenous source. The coincidence of immature solid organic matter and thermogenic gaseous hydrocarbons again indicates that the latter have migrated.

Downhole temperatures determined with the WSTP and ADARA tools down to 250 mbsf show an almost linear downhole increase, defining a bulk temperature gradient of about 56°C/km at Site 861. Downhole logging could not be attempted at Site 861 due to an emergency pullout. Rough weather conditions when pulling out made the deployment of a free-fall funnel impossible, and therefore Hole 861D could not be reoccupied.

BACKGROUND AND OBJECTIVES

The continental margin of southern Chile has been the locus of subduction of Pacific oceanic crust throughout the Mesozoic

and Cenozoic, and most probably during the Paleozoic. During the whole of this period, the forearc region of the Andean magmatic arc was subjected to changes in its geometry that should be reflected in its internal structure, and in uplift and subsidence processes on the outer continental shelf. One of the enigmatic features of the Chilean continental margin (Fig. 1) is the absence of a large accretionary prism, and the presence of island-arc-related Mesozoic igneous rocks near the present trench. The latter fact has been interpreted by Miller (1970a) and Rutland (1971) as resulting from subduction-induced tectonic erosion, possibly continuing through most of the Cenozoic. As along the Peruvian segment of the Andean convergent margin (e.g., von Huene and Lallemand, 1990), forearc subsidence is a likely consequence of subduction erosion. Conversely, forearc uplift may be related to tectonic underplating of large masses of sediment. Other causes of forearc subsidence are conceivable, such as subsidence of the downgoing oceanic plate, or upper plate extensional deformation (see discussion in von Huene and Scholl, 1991). Subsidence of the downgoing oceanic slab is likely to occur when progressively older oceanic crust is subducted with time. In the case of the region north of the Chile Triple Junction, the opposite is true: the portion of the Nazca Plate subducted here becomes progressively younger with time, and in the area of Leg 141, oceanic crust as young as Pleistocene is involved in the subduction process. As to upper plate extension in the forearc and its mechanisms and causes, the answer is somewhat less obvious. Landward of the Leg 141 drilling area no obvious evidence exists for large-scale extensional deformation of Cenozoic age in the forearc crust. The only exception may be provided by a north-south trending occurrence of Lower Cretaceous marine volcano-sedimentary rocks around Canal Moraleda east of the Chonos Archipelago (see Mapa Geológico de Chile, 1980). Although not mapped in this way, the structure extending between 44° and 46°S is possibly a graben or half-graben. Overall, the region immediately north of the Chile Triple Junction appears as a favorable area for the documentation of processes of tectonic accretion and tectonic erosion through time, as plate-scale vertical tectonics is unlikely to dilute or obliterate the paleobathymetric signal in the sedimentary biofacies and lithofacies that are expected to return information about vertical crustal movements on the scale of the Southern Chile forearc.

Site 861 is located approximately halfway between the continental shelf edge and the Chile Trench on seismic Line 745 (Figs. 1 and 2). On the seismic section near Site 861 (Fig. 3), a pronounced reflector is found at approximately 800 m below seafloor (mbsf), and a second zone of high reflectivity is seen at about 1100 mbsf. The lower band of reflectors can be traced down from the continental shelf edge and is thought to represent the upper contact of continental basement. The upper reflector has been tentatively interpreted as an unconformity surface within the shelf/slope sediment sequence that overlies basement. Between 300 and 600 mbsf there is a formation rich in pronounced but discontinuous reflectors, which in turn is overlain by a seismically transparent zone approximately 300 m thick. Upslope from Site 861 on seismic Line 745 (Figs. 2 and 3) there is evidence for normal faulting of the sediments overlying acoustic basement, and for offsets of the basement reflector itself. The youngest movements on this fault may have been fairly recent, judging from the break in surface topography upslope from Site 861. As at Sites 859 and 860 on the transect along seismic Line 745, there is a bottom simulating reflector (BSR) in the vicinity of Site 861. Its depth here is approximately 200 mbsf (Fig. 3), and it indicates the possible presence of frozen gas hydrate above this depth. For reasons of safety, Site 861 was chosen to be off the two small topographic highs to the east and the west so as to avoid drilling into an anticlinal BSR configuration.

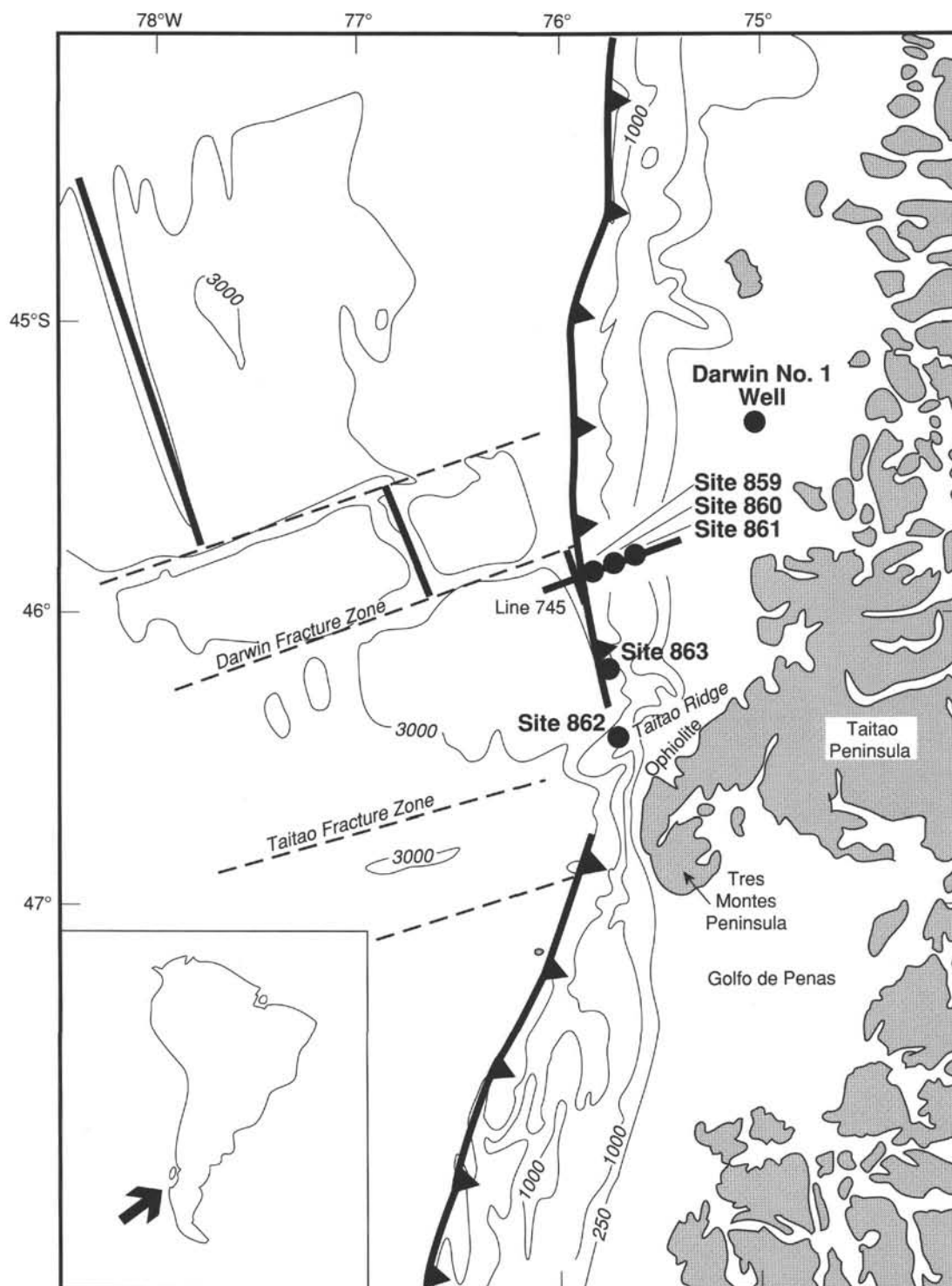


Figure 1. Tectonic-geographic sketch map of the region of the Chile Triple Junction. Locations of seismic Line 745 and Sites 859, 860, and 861 are shown.

The main objectives to be addressed by the drilling at Site 861 were as follows:

1. To determine the age, lithology, depositional history, and the paleobathymetric evolution of the sediments. These four parameters provide valuable clues for deciphering the vertical motion history of this part of the Southern Chile forearc.

2. To test the hypothesis that the landward region of the trench slope is underlain by the Southern Andes continental basement.

3. To gain further insight into the geochemistry and physics of gas-hydrate-bearing sediment.

4. To determine the thermal structure of the middle trench slope.

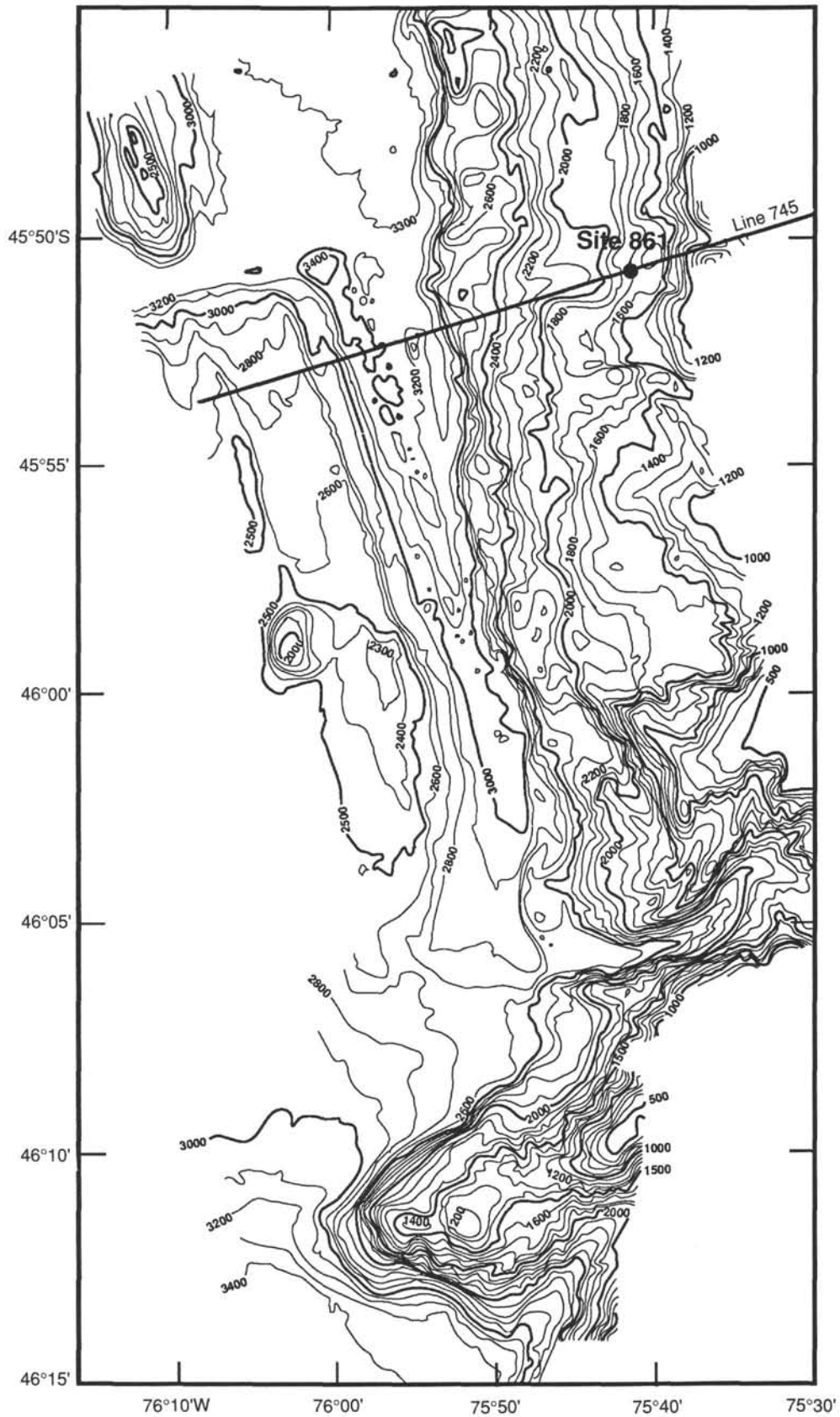


Figure 2. Detailed SeaBeam bathymetric map of the collision zone of the Chile Ridge and Chile Trench. Locations of seismic Line 745 and Site 861 are marked. Contour intervals are 50 m.

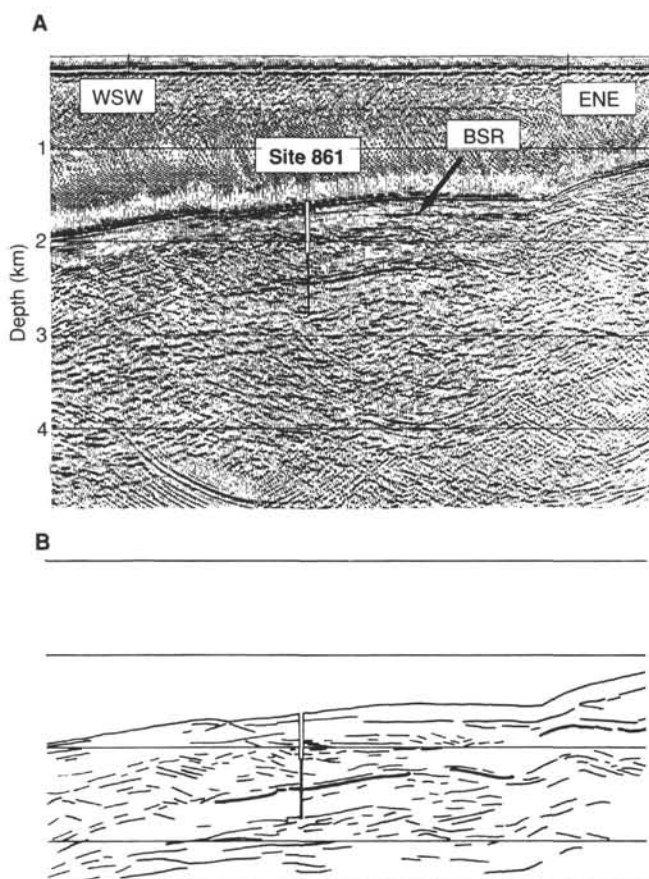


Figure 3. A. Detail of seismic line 745, depth migrated section, no vertical exaggeration, west-southwest to the left. Site 861 is shown with projected (black) and achieved (white) depths of drilling. The bottom-simulating reflector (BSR) is marked. B. Line drawing interpretation of A.

OPERATIONS

Site 861

The 3.5-nm transit from Site 860 to Site 861 was accomplished in dynamic positioning (DP) mode with the ship thrusters and hydrophones down, after tripping out of Hole 860B with a string of logging tools still stuck in the pipe. The seismic survey and beacon drop had already been carried out during the combined survey of proposed Sites SC-1 to -3 prior to operations at Site 859. Operations at Site 861 commenced at 0300 hr (local time is used throughout, local = UTC-3 hr), on 17 December 1991, when the 14-kHz Datasonics commandable/releasable beacon was activated, and DP for Hole 861A began (Table 1).

Hole 861A

The precision depth recorder (PDR) depth for the site was 1690 m below sea level (mbsl), but bottom was tenuously felt by the driller at 1672 m below rig floor (mbrf), and an initial advanced piston corer (APC) core shot to a depth of 1677.5 mbrf returned full, but failed to reveal a clear mudline. Consequently, the bit was pulled above the seafloor, ending Hole 861A at 1015 hr, in preparation for another mudline verification core.

Hole 861B

The drill pipe was lifted 5 m and another APC core was taken. This core barrel was again found to be full, and no mudline was

recovered. The bit was pulled clear of the seafloor again, ending Hole 861B at 1045 hr.

Hole 861C

The drill pipe was lifted an additional 6 m and the mudline for the site was finally established at 1652.2 mbsl with a successful mudline APC core. Piston coring continued through Core 141-861C-10H, where partial stroke and 110,000 lb overpull defined the refusal depth. Both the ADARA temperature and the Tensor orientation tools were used with mixed success on all APC cores after Core 141-861C-2H, although the tools themselves functioned well. Heavy heave conditions caused at least two APC barrels to suffer pre-sheared pins, but the cores recovered did not show ill effects.

Routine extended core barrel (XCB) coring continued down to Core 141-861C-41X at a depth of 353.1 mbsf. Recovery and penetration rates during XCB coring were fair to good, and continuation of coring in that mode allowed for the option of pressure coring system (PCS) coring and heave-decoupled water sampler-temperature probe (WSTP) deployments for optimum investigation of geochemical features in the upper 300+ m of the sediment column, including hydrates assumed to be present because of a strong bottom-simulating reflector (BSR) evident on the seismics.

The PCS was deployed four times, at sub-bottom depths of 71.0, 170.2, 220.1, and 248.3 mbsf. The choice of sub-bottom depths was not as optimized as desired because repeated troubleshooting efforts were required between deployments to determine the cause(s) of mechanical actuation failures that allowed the tool to be recovered with the pressure chamber unclosed. The last two runs did achieve actuation and managed to capture some pressure, but this was significantly less than hydrostatic levels (115 and 190 psi, respectively). Both runs also recovered full (0.86 m or more) cores, but the analyses of gases taken from the cores did not confirm the presence of hydrates nor offer any substantial new information about in-situ gas chemistry.

The WSTP tool (with old Uyeda electronics) was deployed five times in both water sampling and temperature measurement modes and six times as a temperature probe only. Five good water samples were obtained, and temperature results appeared to be very reliable until the final three temperature runs, in which measurements were questionable. It was thought that the probes cracked the formation upon insertion during these unreliable runs.

DP was lost momentarily near the end of the APC coring sequence when the primary beacon began to fail. A standby beacon was dropped and when it too showed signs of erratic behavior, a third beacon was deployed. Dead reckoning kept the ship on location to within 3% of water depth until the first standby beacon finally began to put out a reliable signal and normal DP was resumed. The original and second standby beacons were released three days later when good weather and calm seas offered the opportunity for easy Z-boat recovery.

As at Sites 859 and 860, hydrocarbon gases in Hole 861C were common in all cores, and cores of the softer sediments expanded mildly from the liners. Some heavy hydrocarbon species were observed (C_4 and C_6) but not to alarming levels. The C_1/C_2 ratio (as determined in vacutainer samples) declined steadily until leveling at about 600.

Hole 861C was arbitrarily terminated at 2005.3 mbsl (353.1 mbsf) to change to the rotary core barrel (RCB) coring system for a deep (1200 mbsf) penetration to the projected depth of continental basement. The pipe was pulled clear of the hole while it was displaced with weighted mud for hole abandonment. As at Sites 859 and 860, the hole was not plugged with cement because of the presumed presence of methane hydrates. The drill string

Table 1. Coring summary, Site 861.

Core	Date (Dec 1991)	Time UTC	Depth (mbsf)	Length cored (m)	Length recovered (m)	Recovery (%)	Age
141-861A-1H	17	1315	0.0-9.5	9.5	10.00	105.2	
Coring totals				9.5	10.00	105.2	
141-861B-1H	17	1345	0.0-9.5	9.5	9.92	104.0	
Coring totals				9.5	9.92	104.0	
141-861C-1H	17	1430	0.0-3.0	3.0	3.03	101.0	u. Pleistocene
2H	17	1530	3.0-12.5	9.5	9.83	103.0	u. Pleistocene
3H	17	1615	12.5-22.0	9.5	10.14	106.7	u. Pleistocene
4H	17	1715	22.0-31.5	9.5	9.80	103.0	u. Pleistocene
5H	17	2100	31.5-41.0	9.5	10.61	111.7	u. Pleistocene
6H	17	2220	41.0-50.5	9.5	10.23	107.7	u. Pleistocene
7H	18	0200	50.5-60.0	9.5	11.52	121.2	u. Pleistocene
8H	18	0515	60.0-69.5	9.5	10.42	109.7	u. Pleistocene
9P	18	0630	69.5-71.0	1.5	0.23	15.3	u. Pleistocene
10H	18	0715	71.0-80.5	9.5	8.97	94.4	u. Pleistocene
11X	18	1030	80.5-90.1	9.6	0.05	0.5	u. Pleistocene
12X	18	1245	90.1-99.8	9.7	2.72	28.0	u. Pleistocene
13X	18	1345	99.8-109.4	9.6	1.30	13.5	u. Pleistocene
14X	18	1445	109.4-119.0	9.6	3.16	32.9	u. Pleistocene
15X	18	1700	119.0-128.9	9.9	7.83	79.1	l. Pleistocene
16X	18	1430	128.9-138.7	9.8	7.22	73.7	l. Pleistocene
17X	18	1830	138.7-148.5	9.8	2.67	27.2	l. Pleistocene
18X	18	1915	148.5-158.3	9.8	5.68	57.9	l. Pleistocene
19X	18	2130	158.3-168.2	9.9	0.88	8.9	l. Pleistocene
20P	18	2210	168.2-170.2	2.0	0.00	0.0	u. Pliocene
21X	18	2310	170.2-179.9	9.7	2.71	27.9	u. Pliocene
22X	19	0005	179.9-189.6	9.7	8.82	90.9	u. Pliocene
23X	19	0250	189.6-199.2	9.6	0.00	0.0	u. Pliocene
24X	19	0430	199.2-208.9	9.7	0.30	3.1	u. Pliocene
25X	19	0630	208.9-218.6	9.7	8.67	89.4	u. Pliocene
26P	19	0640	218.6-220.1	1.5	1.00	66.6	u. Pliocene
27X	19	0800	220.1-228.1	8.0	6.35	79.4	u. Pliocene
28X	19	1045	228.1-237.7	9.6	6.76	70.4	u. Pliocene
29X	19	1200	237.7-247.3	9.6	1.67	17.4	u. Pliocene
30P	19	1245	247.3-248.3	1.0	0.68	68.0	u. Pliocene
31X	19	1415	248.3-257.0	8.7	4.17	47.9	u. Pliocene
32X	19	1700	257.0-266.6	9.6	3.06	31.9	u. Pliocene
33X	19	1830	266.6-276.2	9.6	3.10	32.3	u. Pliocene
34X	19	2000	276.2-285.9	9.7	6.47	66.7	u. Pliocene
35X	19	2250	285.9-295.6	9.7	5.18	53.4	u. Pliocene
36X	20	0025	295.6-304.9	9.3	5.74	61.7	u. Pliocene
37X	20	0210	304.9-314.5	9.6	3.12	32.5	u. Pliocene
38X	20	0500	314.5-324.2	9.7	0.37	3.8	u. Pliocene
39X	20	0900	324.2-333.9	9.7	4.45	45.9	u. Pliocene
40X	20	1045	333.9-343.4	9.5	7.26	76.4	u. Pliocene
41X	20	1400	343.4-353.1	9.7	6.00	61.8	u. Pliocene
Coring totals				353.1	202.17	57.3	
141-861D-	Drilled		0.0-342.3				
1R	21	1145	342.3-351.9	9.6	5.26	54.8	u. Pliocene
2R	21	1315	351.9-361.6	9.7	3.28	33.8	u. Pliocene
3R	21	1430	361.6-371.0	9.4	0.00	0.0	u. Pliocene
4R	21	1730	371.0-380.7	9.7	0.00	0.0	u. Pliocene
5R	21	2310	380.7-390.4	9.7	0.00	0.0	u. Pliocene
6R	21	2310	390.4-400.1	9.7	3.67	37.8	u. Pliocene
7R	22	0045	400.1-409.8	9.7	4.30	44.3	u. Pliocene
8R	22	0215	409.8-419.4	9.6	1.22	12.7	u. Pliocene
9R	22	0345	419.4-429.1	9.7	4.97	51.2	u. Pliocene
10R	22	0520	429.1-438.8	9.7	1.68	17.3	u. Pliocene
11R	22	0725	438.8-448.5	9.7	2.61	26.9	u. Pliocene
12R	22	0930	448.5-458.1	9.6	3.63	37.8	u. Pliocene
13R	22	1115	458.1-467.7	9.6	3.82	39.8	u. Pliocene
14R	22	1300	467.7-476.3	8.6	1.32	15.3	u. Pliocene
15R	22	1445	476.3-486.0	9.7	1.85	19.1	u. Pliocene
16R	22	1630	486.0-496.3	10.3	3.04	29.5	u. Pliocene
Coring totals				154.0	40.65	26.4	

was pulled and Hole 861C was completed when the bit cleared the rotary table at 1530 hr, 20 December 1991.

Hole 861D

The vessel was offset 20 m northwest and a standard RCB bottom-hole assembly complete with drilling jars was put to-

gether. The pipe was run in with a center bit in place in the outer core barrel and Hole 861D was spudded at 2015 hr, 20 December 1991. Drilling with the center bit continued to a depth of 1994.5 mbsl (342.3 mbsf) where the center bit was replaced with an RCB core barrel and coring began. A bit deplugger was dropped twice after netting zero recovery for Cores 141-861D-3R to -5R. Both

times a clay plug was removed, but it seemed to reappear between core barrel deployments. Sidewall scraping during heavy heave conditions probably contributed to the bit plugging problem. However, the problem disappeared as suddenly as it had appeared, and RCB coring was conducted with good results to Core 141-861D-16R at 496.3 mbsf. High seas produced heave conditions 21 December very nearly at the heave compensator's stroke limit; however, operations continued without interruption until the weather abated somewhat 22 December. At 1330 hr, 22 December, a medical evacuation emergency was declared by the ship's surgeon, who had been treating the UDI Second Engineer for lung-related illness for several weeks. The doctor determined that an immediate evacuation to the nearest medical facility was necessary in the interest of the crewman's health. The local ship's agent arranged for us to rendezvous with a pilot boat and doctor in the sheltered waters of the Gulf of Corcovado off Puerto Quellon, Chile. No helicopter or small boat was available to serve as the evacuation vehicle because of the distances and weather conditions.

Consequently, Hole 861D was terminated and the drill string was pulled while displacing the hole with barite-weighted mud. The option to deploy a minicone was considered, but was rejected on the grounds of adverse personnel safety due to high seas washing the main deck at the time of the evacuation. The beacon was also left behind as weather and sea conditions made recovery dangerous and unlikely to be successful. Plans were tentatively made to return to the two sites where beacons had been abandoned (860 and 861) during the transit from Puerto Quellon to the next site, if weather conditions allowed for retrieval.

Transit to Puerto Quellon and back to the Chile Triple Junction

The drill string was pulled and the entire selection of drill collars were laid down in the main-floor collar racks in preparation for a bad weather transit north along the coast over some 200 nm to Puerto Quellon. The vessel departed Site 861 at 2100 hr, 22 December. The transit to the medical-evacuation rendezvous was uneventful as the heavy rolls expected from the broadside swells were not as bad as feared. The rendezvous took place on schedule at 1500 hr on December 23 and with a minimum of red tape. The ship returned south along the coast to Sites 861 and 860 where the two previously unreleased beacons were recovered. The ship then proceeded to the waypoint for the start of the presite survey for proposed Site SC-6, and deployed seismic gear.

LITHOSTRATIGRAPHY

Four holes were drilled at Site 861. Recovered intervals at the first three holes can be correlated using a distinctive bed found at Sections 141-861A-1H-2, 95–110 cm, 141-861B-1H-6, 40–55 cm, and 141-861C-2H-4, 30–45 cm (Fig. 4; also see core photographs in the Visual Core Description section, this volume). This correlation suggests that approximately 5.5 m of section recovered in Holes 861B and 861C were not recovered in Hole 861A.

The lithostratigraphy for Site 861 is derived from Holes 861C and 861D. The unit and subunit divisions primarily reflect changes in sediment composition, grain size, and consolidation. The Unit I/Unit II boundary (43.8 mbsf) marks the base of a microfossil-rich, fine-grained sequence, which is underlain by a coarse-grained interval containing significant amounts of sand and gravel-sized materials. This boundary is somewhat gradational, however, in that the pelagic component (nannofossils) persists below this boundary in the coarser units. The coarser materials of Unit II are subdivided at 208.9 mbsf; this boundary marks a change in degree of consolidation, and below it the sediments are termed "stones." As with the earlier Leg 141 sites,

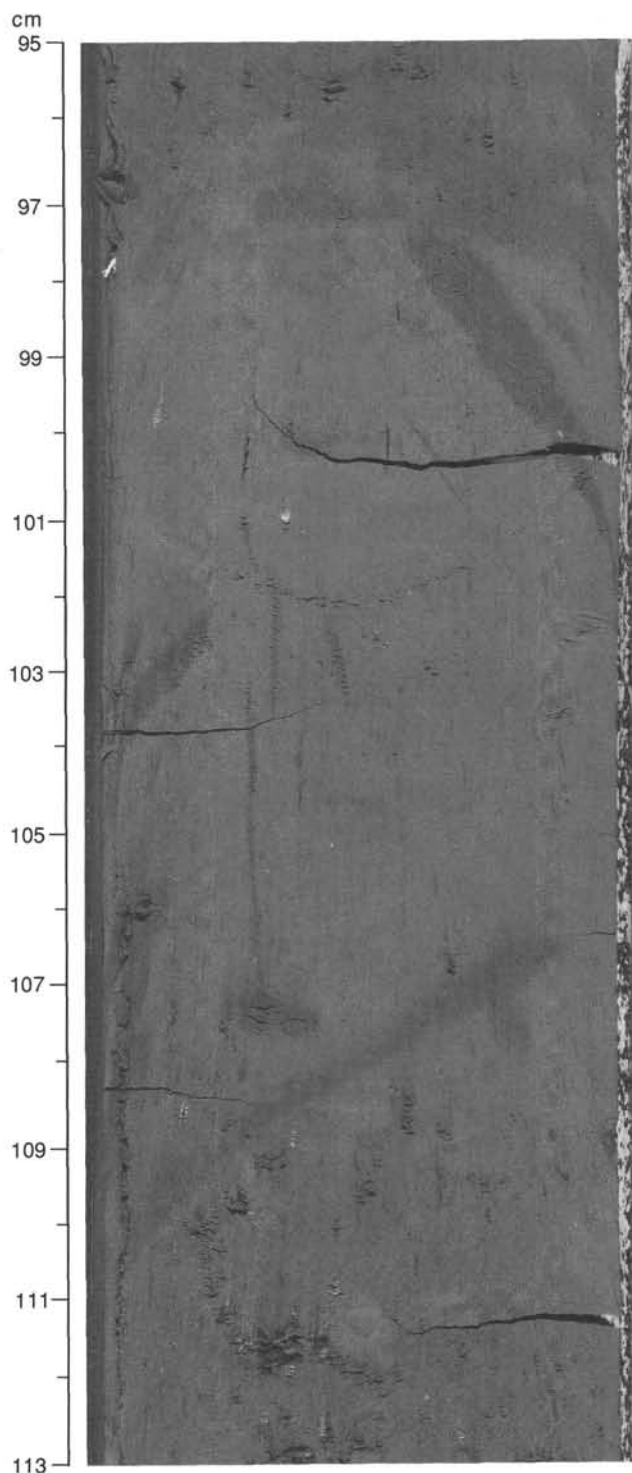


Figure 4. Core photograph, Section 141-861A-1H-2, 95–113 cm. Distinctive, bioturbated, bed of grayish olive (10Y 4/2) clay present in Holes 861A, 861B, and 861C. Isolated dark and light pods have been vertically smeared out along the core during cutting.

this boundary is also somewhat gradational, in that there are a few semilithified intervals above and below it. The Unit II/Unit III boundary at 351.9 mbsf is similar to the Unit I/Unit II boundary in that it marks a change in sediment grain size, from coarse- to finer-grained materials.

There was 100% recovery in Holes 861A and 861B and the upper eight cores in Hole 861C (due to gas expansion, measured recoveries actually exceeded 100% in these cores). After Core 141-861C-10H, recovery at Hole 861C was more sporadic, with zones of low recovery alternating with zones of high recovery, averaging 44%. Recovery markedly decreased in Hole 861D, averaging 26%.

Lithologic Units

Unit I (Cores 141-861A-1H and 141-861B-1H, and Sections 141-861C-1H through -6H-2, 132 cm; age, late Pleistocene; depth, 0–43.8 mbsf)

Unit I occurs in Holes 861A, 861B, and 861C (Table 2). The definition of this unit is based on the continuous section recovered at Hole 861C. This unit consists of variegated (olive gray: 5Y 4/1 and 5Y 3/2; grayish-olive: 10Y 4/2; grayish olive green: 5GY 3/2; dark greenish-gray: 5GY 4/1) silty clay to clayey silt and grayish-olive green (5Y 3/2) nannofossil silt, nannofossil clayey silt, and light olive gray (5Y 5/2) to olive gray (5Y 3/2) silty clay with nannofossils. Minor lithologies include variegated (olive black: 5Y 2/1; grayish-olive green: 5GY 3/2; dark greenish-gray: 5GY 4/1) graded silt and sand beds/laminae that may have sharp bases and rarely exhibit load structures (Fig. 5). These laminae are often mottled or diffuse and have been disseminated/redistributed by bioturbation.

Isolated, black, organic/pyrite-rich, silty pods occur throughout the unit. These may be bioturbation features. Other whitish pods are also scattered throughout the core, of which some are calcareous and others contain concentrations of sponge spicules. These concentrations may be fecal pellets or bioturbation features. Large foraminifers and some shell fragments are present in this unit.

The petrology of these sediments is similar to the fine-grained facies recovered at Sites 859 and 860 (see Lithostratigraphy section, Sites 859 and 860 chapters). Silt-sized components include quartz, feldspar (predominantly plagioclase), rock fragments (metamorphic and chert fragments), colorless to brown to tachylitic glassy volcanic fragments (some pumiceous and commonly microlitic), mica (biotite and muscovite), opaques (including framboidal pyrite), epidote, amphibole, organic matter, and

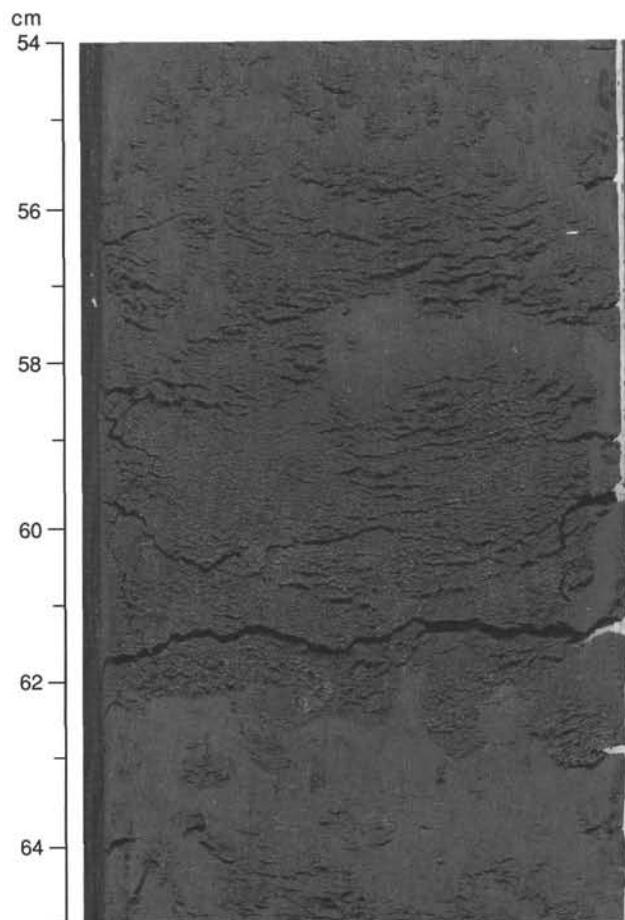


Figure 5. Core photograph, Section 141-861A-1H-5, 54–65 cm. Graded sand to silt bed partially redistributed by bioturbation. Possible load structures at base.

Table 2. Lithostratigraphy, Site 861.

Units	Age	Interval and depth	Lithology
Unit I	late Pleistocene	Cores 141-861A-1H, 141-861B-1H, 141-861C-1H through -6H, Section 2, 132 cm (0–43.8 mbsf)	Silty clay to clayey silt with nannofossils
Subunit IIA	late Pleistocene to late Pliocene	Cores 141-861C-6H-2, 132 cm, through 141-861C-24X*** (43.8–208.9 mbsf)	Silty clay to clayey silt, silt, silty sand, sand, and matrix-rich gravel
Subunit IIB	late Pliocene	Cores 141-861C-25X through -41X, and 141-861D-1R (208.9–351.9 mbsf)	Clayey siltstone to silty claystone, and matrix-supported conglomerate
Unit III	late Pliocene	Cores 141-861D-2R through Core 141-861D-16R (351.9–496.3 mbsf)	Silty claystone to clayey siltstone

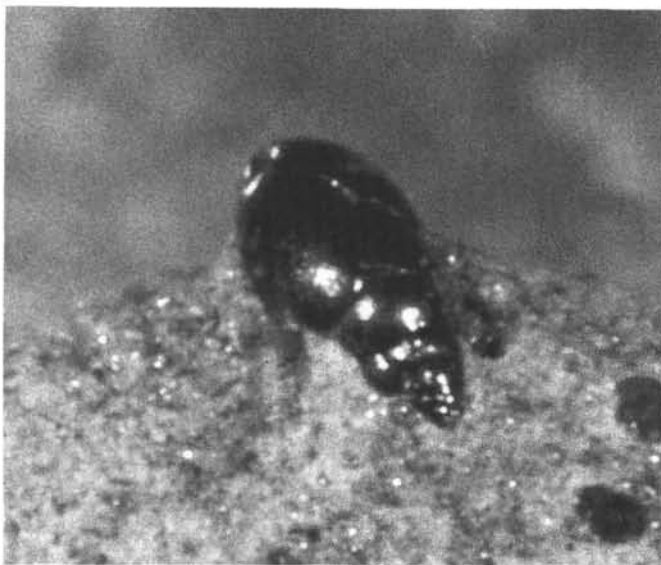
***Note: boundary between Units IIA and IIB is transitional.

micrite (fragmented foraminifers?). Microfossils include foraminifers, calcareous nannofossils, diatoms, radiolarians, siliceous sponge spicules, and silicoflagellates. Diagenetic features include disseminated and concretionary pyrite. Locally, pyrite has replaced microfossils (Fig. 6).

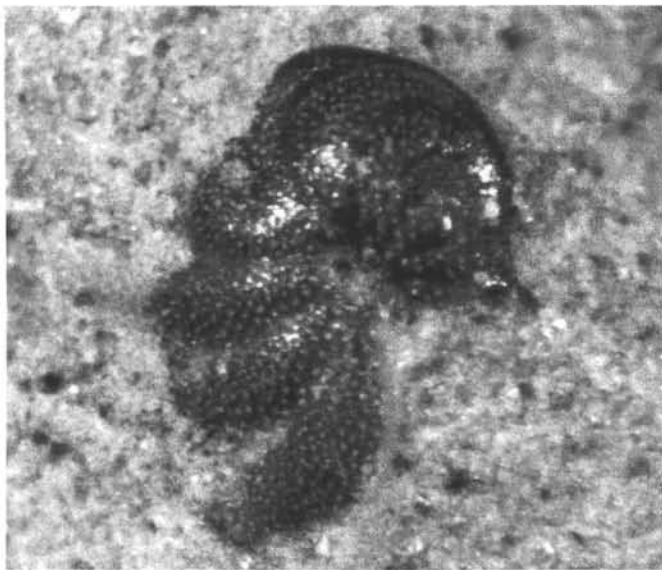
Sedimentary structures present in Unit I include rare lamination and graded beds. Contacts vary from sharp to diffuse, and many contacts defined by thin, silty laminae have been disrupted/redistributed by bioturbation. In Core 141-861C-4H a cyclic repetition occurs, where silty clay passes up from a sharp base into bioturbated nannofossil clayey silt.

Subunit IIA (Cores 141-861C-6H-2, 132 cm, through -24X; age, late Pleistocene to late Pliocene; depth, 43.8–208.9 mbsf)

Lithologies present in Subunit IIA include matrix-rich, olive green (5Y 3/2) granule to pebble gravel, olive gray (5Y 3/2; 5Y 4/1) silty sand and sandy silty clay, olive black (5Y 2/1) silt, olive gray (5Y 3/2 to 5Y 4/1) silty clay to clayey silt, and olive gray (5Y 4/1) to dark gray (N4) clay. Matrix-rich gravels range from matrix- to grain-supported. Gravel units vary in thickness from a few centimeters to more than 1 m. Gravel-sized materials are predominantly granules with some pebbles. Maximum grain sizes vary up to 2.2 cm. The gravel is composed of angular to well-rounded fragments of claystone to silty claystone to siltstone (similar in composition to the matrix), with some wood/plant and shell fragments. The lower contacts of gravel units are sharp,



1 mm



1 mm

Figure 6. Core photograph, Section 141-861C-4H-1, 70–71 cm. Calcareous foraminifers replaced by pyrite (*Bulimina* sp., top; *Planulina wuellerstorfi*, bottom).

whereas the upper contacts tend to be gradational. Minor lithologies include volcanic ash/tuffaceous sand (Fig. 7). The coarser lithologies are interbedded with silty clay and nannofossil silty clay. Some preferentially consolidated silty claystone is present in Core 141-861C-15X. As in Unit I, these fine-grained lithologies have been bioturbated and contain dark streaks of organic matter and small white specks composed of sponge spicules.

Silt- and sand-sized components include quartz, feldspar (predominantly plagioclase), metamorphic rock fragments, colorless

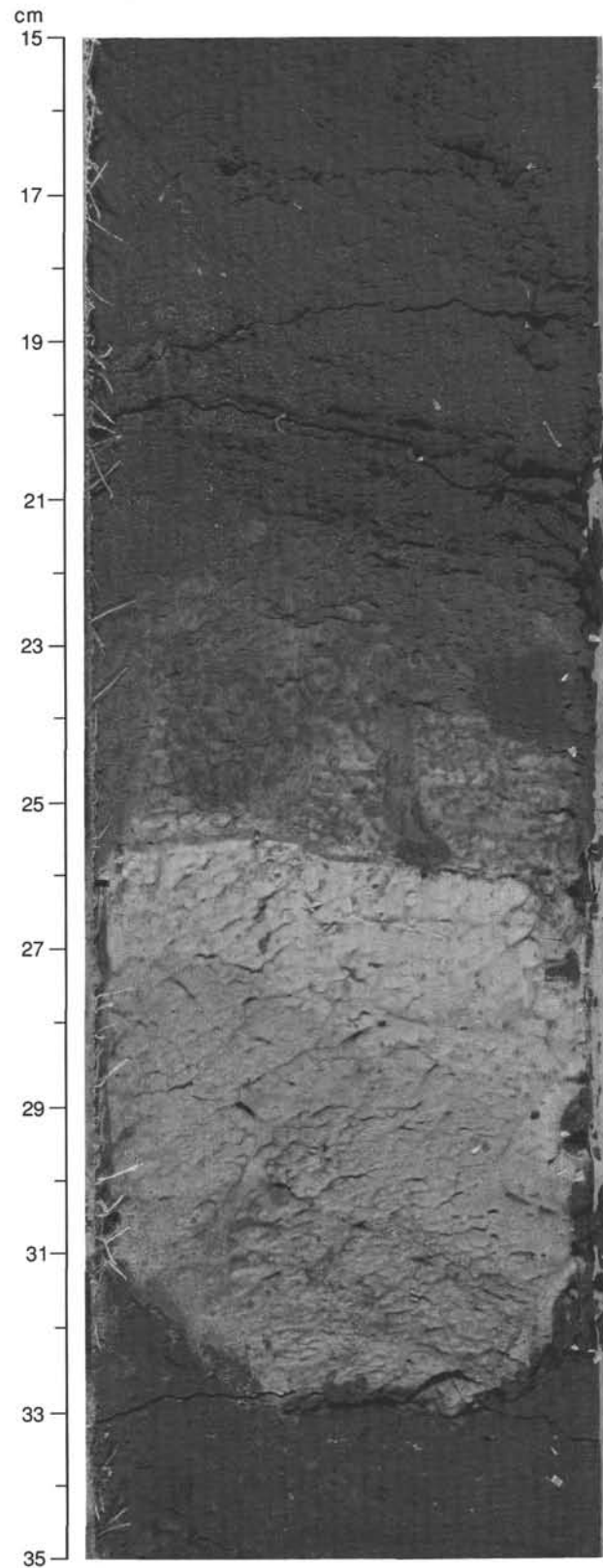


Figure 7. Core photograph, Section 141-861C-8H-5, 15–35 cm. Light olive-gray (5Y 6/1) to light gray (N7), stratified, normally-graded, volcanic ash layer. The top of this bed is bioturbated and overlain by laminated tuffaceous sand (20–21 cm).

to brown to tachylitic glassy volcanic fragments (commonly microclitic), mica (biotite and muscovite), chlorite, opaques (including framboidal pyrite), epidote, amphibole, and pyroxene. Microfossils include foraminifers, nannofossils, diatoms, radiolarians, siliceous sponge spicules, silicoflagellates, and some bioclasts (shell and echinoid fragments). Other components include organic matter. Some wood/plant fragments (Fig. 8) and pelecypod shells and shell fragments are present in the sandy layers.

Subunit IIA is characterized by the presence of several types of sedimentary sequences. In Cores 141-861C-7H and -8H, upward-fining, normally graded cycles with coarser basal portions (sand to gravel) grade upward to laminated and then bioturbated silty clay (Fig. 9). The muddy gravels in Core 141-861C-8H have sharp bases and tops with no grading and no stratification, whereas the gravel units in Core 141-861C-10H are parts of upward-fining successions starting with poorly sorted, matrix-supported, granule to pebble-sized gravel or better-sorted, grain-supported gravel (Fig. 10), and progressing to laminated fine sand, silt, and silty clay (Fig. 11). Partial sequences occur throughout these cores. Graded units present in Core 141-861C-15X exhibit upward-fining sequences that start at a sharp planar-to-scoured base overlain by a muddy granule/sandy unit that fines

upward through sandy silt into cross-laminated-to-laminated silt and clayey silt, capped by bioturbated silty clay (partial Bouma sequences). Some of these cycles begin with a gravel-rich mud (Fig. 12). These cycles are underlain in Cores 141-861C-16X and -17X by a series of graded units similar to those in Core 141-861C-15X, but slightly finer-grained. Most of the units in Cores 141-861C-16X and -17X grade up from sandy silt to silt with only minor bioturbation.

Subunit IIB (Cores 141-861C-25X through -41X, and 141-861D-1R; age, late Pliocene; depth, 208.9–351.9 mbsf)

This subunit can be subdivided into finer- and coarser-grained facies. The fine-grained facies predominantly consists of massive, olive gray (5Y 4/1 to 5Y 3/2) silty claystone to clayey siltstone and claystone. These rocks are structureless, except for a few faint laminations. Minor fine-grained lithologies include interbeds of olive gray (5Y 4/1) siltstone with nannofossils, olive gray (5Y 3/2) nannofossil silty claystone, and silty claystone with nannofossils. Locally, these finer-grained intervals are laminated or bioturbated, with some isolated gravel-sized clasts, pyrite concretions, and shell fragments.

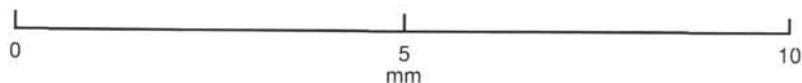


Figure 8. Photomicrograph, thorny twig(?) from Section 141-861C-6H-6, 71–72 cm.

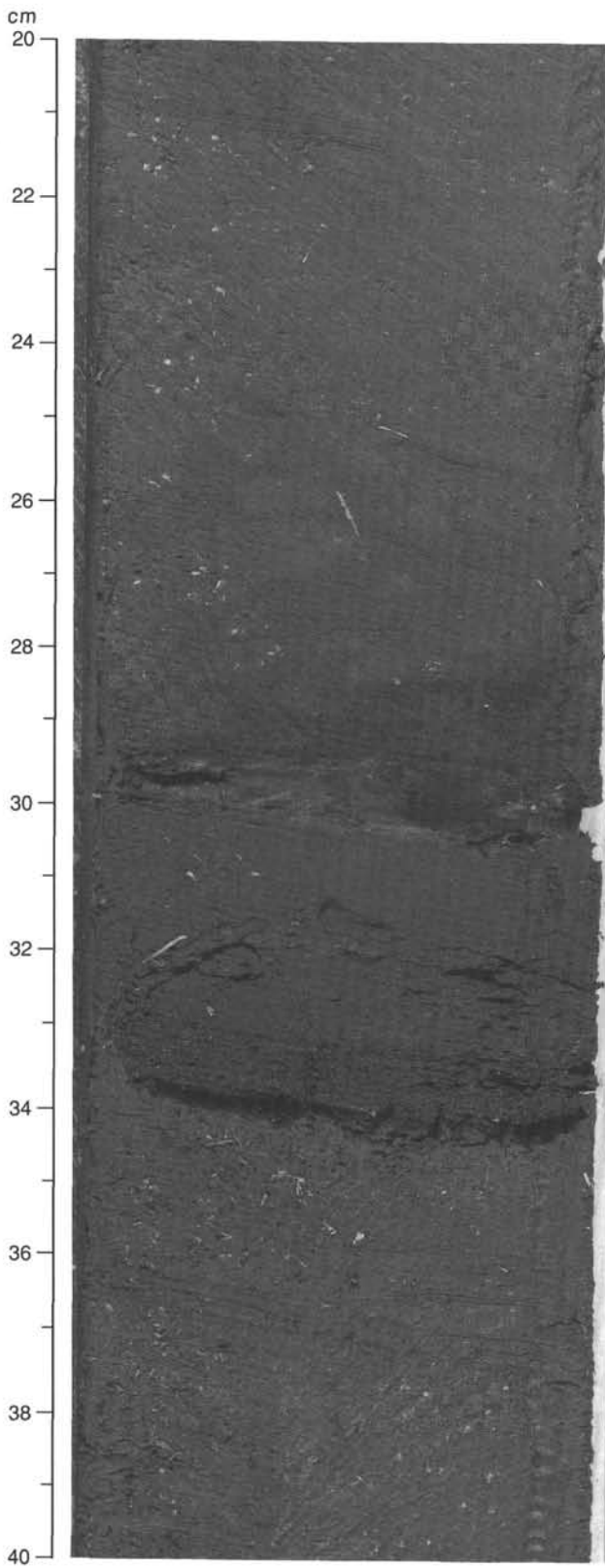


Figure 9. Core photograph, Section 141-861C-7H-8, 20–40 cm. Amalgamated(?) series of graded units from sand (dark) to silty clay (light). Note mottling due to bioturbation at top of second graded unit (25–28 cm).

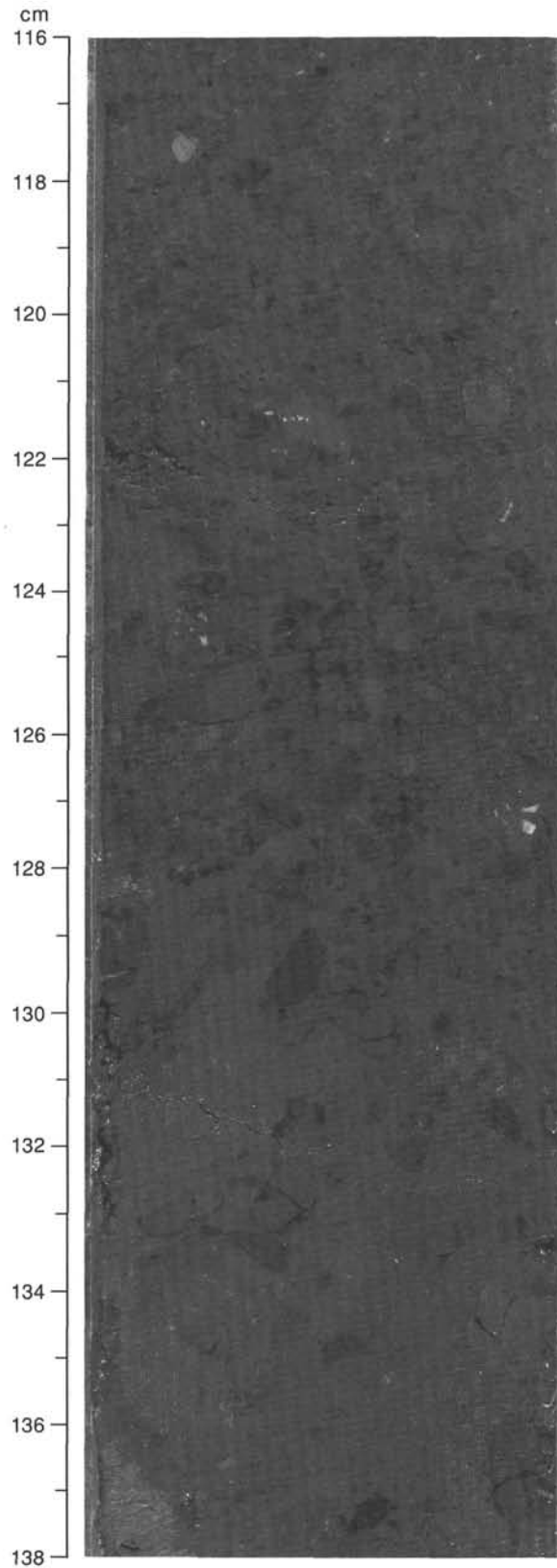


Figure 10. Core photograph, Section 141-861C-10H-3, 116–138 cm, part of a single(?) depositional unit that makes up the majority of this core. The interval shown here is near the base of this unit and shows a gradational change from inversely(?) graded, matrix-supported, pebbly mud (diamictite) to clast-supported, normally graded conglomerate. The base of this unit was removed for an interstitial water sample.

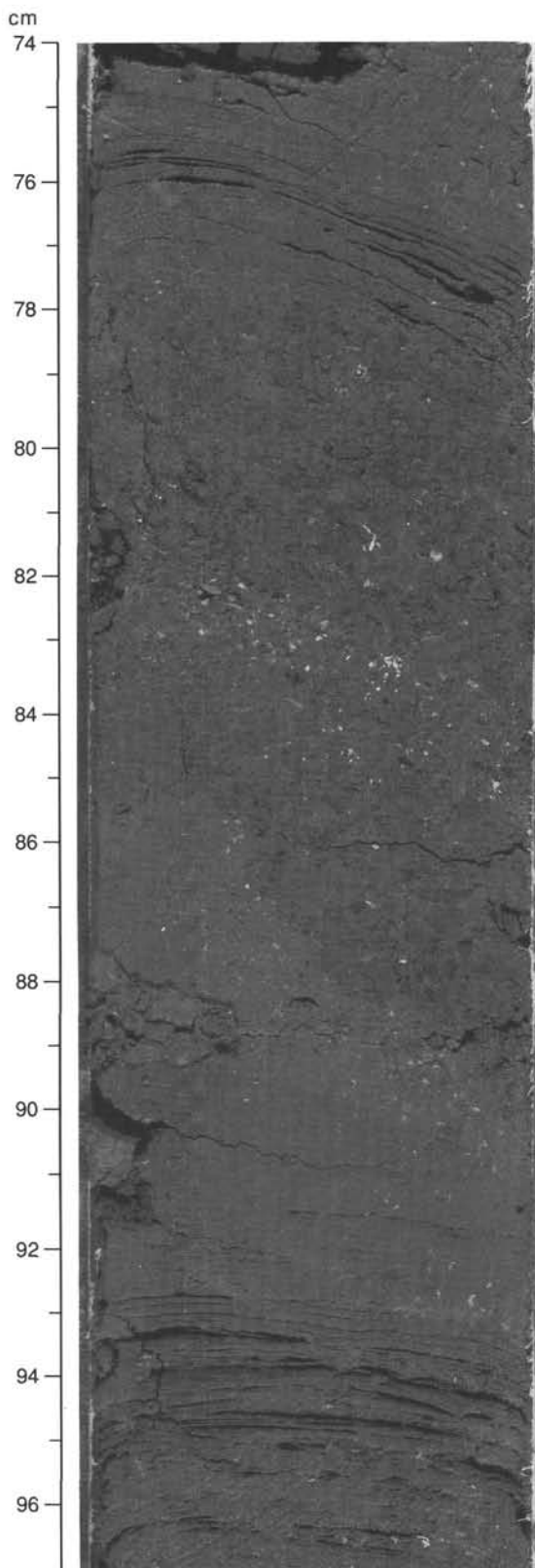


Figure 11. Core photograph, decimeter-scale cycles in Section 141-861C-10H, 74-97 cm. Granule gravel begins at a diffuse contact and fines up into laminated fine-sand to silt. Note laminated top of previous cycle below conglomerate.

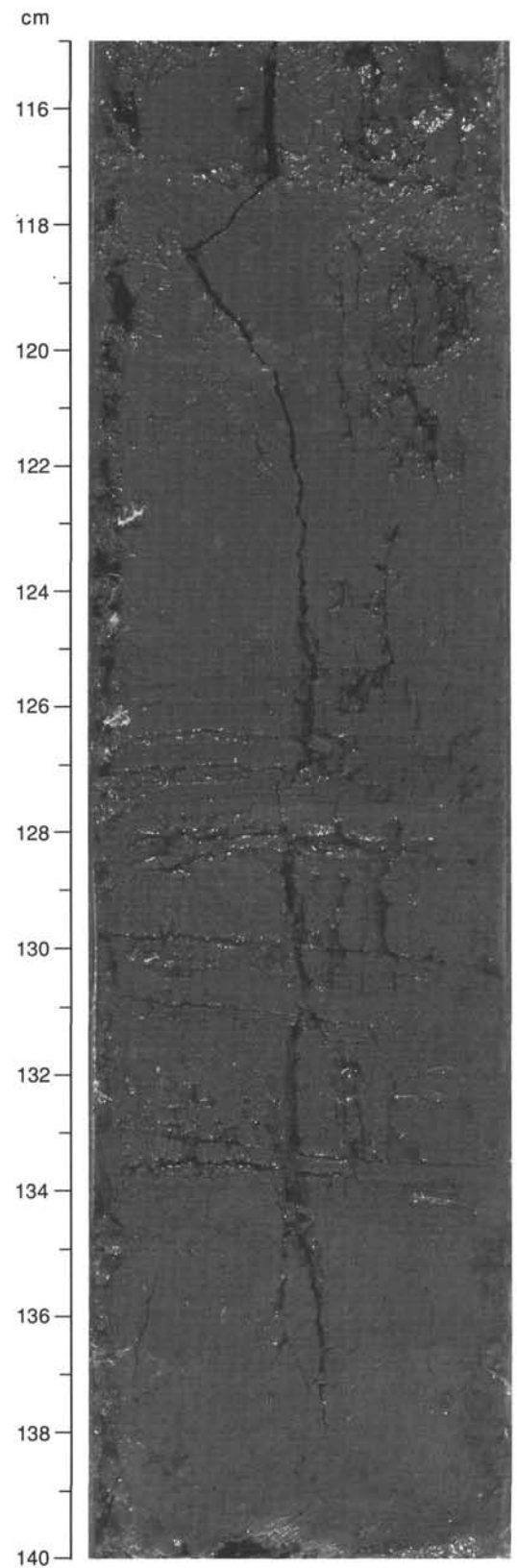


Figure 12. Core photograph, decimeter-scale cycle in Section 141-861C-15X-3, 115-140 cm. In this unit, a granule-rich muddy gravel grades up into cross-laminated (?; 128-134 cm) to laminated (125-128 cm) sandy silt to bioturbated silty clay (note lighter burrows at 120 cm). The base of this unit was removed for an interstitial water sample.

Coarse lithologies include olive gray (5Y 4/1; 5Y 3/2) sandstone, sandy siltstone, clayey sandstone, granule conglomerate, and pebbly mudstone. The conglomerate units are thin- to thickly bedded and range from clast- to matrix-supported. Clast sizes range from granule to pebble with a maximum clast size of 3 cm (Core 141-861C-39X). Clasts are predominantly angular to well-rounded siltstone and claystones, some of them nannofossil-rich. Dark greenish-black (5GY 2/1) clasts are also present in some cores (i.e., Core 141-861C-35X). The matrix consists of silty claystone to clayey siltstone that contains some shell fragments and, rarely, fish debris. The bases of the conglomeratic units are commonly sharp, with sharp to gradational tops.

Silt- and sand-sized components include quartz, feldspar (predominantly plagioclase), colorless to brown glassy volcanic fragments (some pumice), mica (biotite and muscovite), opaques (including framboidal pyrite), epidote, amphibole, pyroxene, and organic matter. Microfossils include foraminifers, nannofossils, diatoms, radiolarians, siliceous sponge spicules, and silicoflagellates. The nannofossil component is often partially to wholly recrystallized to micrite.

Unit III (Cores 141-861D-2R through 141-861D-16R; age: late Pliocene; depth: 409.8–596.3 mbsf)

This unit consists of interbedded olive gray (5Y 3/2; 5Y 4/1; 5Y 3/1) to olive black (5Y 2/1) clayey siltstone to silty claystone and claystone. These lithologies are locally laminated and bioturbated. They contain both disseminated and concretionary pyrites and some shell fragments. Minor lithologies include a thin bed of nannofossil chalk in Core 141-861D-2R, clayey siltstone with nannofossils, nannofossil siltstone, nannofossil clayey siltstone, and massive sandstone.

Silt- and sand-sized components include quartz, feldspar (predominantly plagioclase), rock fragments, colorless (and black) to tachylitic glassy volcanic fragments (commonly microlitic), mica, opaques (including framboidal pyrite), epidote, amphibole, and organic matter. Microfossils include foraminifers, nannofossils, diatoms, radiolarians, and siliceous sponge spicules. The nannofossil component is, in part, recrystallized to micrite.

Sediment Accumulation Rates

The biostratigraphic analysis of Site 861 cores (see below) provides several microfossil age constraints: a 0.25-Ma datum (NN21–NN20 boundary) at 31 to 41 mbsf, the boundary between the upper and lower Pleistocene (≈ 0.45 Ma) at 119 to 129 mbsf, and the boundary between the Pleistocene and Pliocene (≈ 1.6 Ma) at approximately 170 mbsf. In addition, nannofossil and foraminifer assemblages in the lowermost cores from Hole 861D suggest that the base of the section lies just above the upper/lower Pliocene boundary (≈ 3.2 Ma). Estimates of Site 861 apparent sediment accumulation rates (uncorrected for compaction) are plotted in Figure 13. The rates of accumulation in the upper 129 m of section appear to be relatively uniform (260 m/m.y.). Sediment accumulation rates markedly decrease to 44 m/m.y. from 129 to 170 mbsf to rates comparable for this time interval seen at Site 860. Apparent accumulation rates increase for the upper Pliocene, with an estimated value of 200 m/m.y. The apparent increase could represent structural thickening in this lower interval, in analogy to that seen at Site 860, but no clear repetitions of sections or zones of structural disruption (thrusting) similar to that documented for Site 860 were observed in this hole.

X-ray Diffraction Analysis of Sediments

Fifteen samples were selected from Site 861 cores (Holes 861C and 861D) for X-ray diffraction analysis. Bulk powders were prepared and analyzed using the shipboard Philips ADP 3520 X-ray diffractometer. These bulk sediment samples are overall

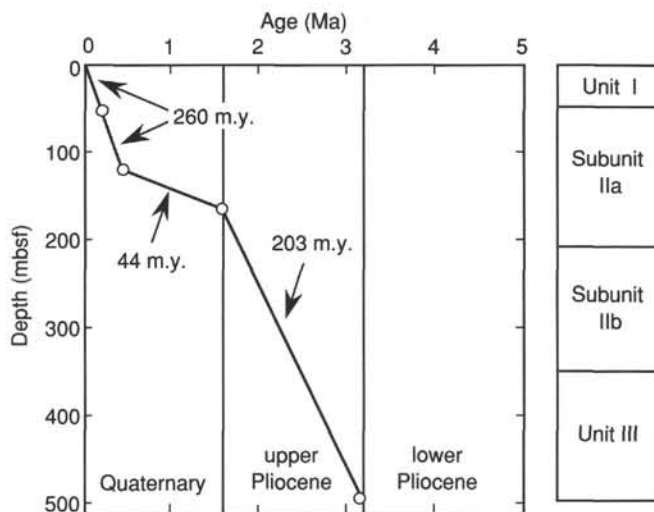


Figure 13. Estimates of apparent sediment accumulation rates at Site 861.

very similar in the presence and relative abundance of mineral phases (Table 3). The dominant phases are quartz and feldspar with only small variations in their abundance. All cores contain an unidentified amorphous phase and a minor to trace amount of hornblende. Calcite is present in trace to minor amounts in many of the samples. Roughly equal proportions of the clay minerals chlorite and illite are present, whereas smectite is not an identifiable component.

Interpretation

The nature of the sediments recovered at Site 861 is consistent with a glacially influenced marine origin. The composition of these sediments suggests a mixed provenance of arc-derived volcanoclastic materials and a lesser proportion of basement-derived materials. The presence of basement-derived materials could be explained by either glacial or nonglacial erosion and transport, whereas explaining the supply of the large volcanoclastic component is not straightforward. Today, the westward dispersion of arc-derived sand- and silt-sized volcanic ash to the Chilean continental slope is minimized by the eastward-prevailing winds and the complex system of inland waterways and subaerial drainage produced by glacial dissection of the coastal regions. Pliocene-Pleistocene volcanic eruptions that breached the ice sheet (or occurred on ice-free volcanoes) could have covered the surrounding glaciated regions with blankets of ash similar in thickness (0.3–0.4 m) to those observed on the recent glaciers in Kamchatka (Vinogradov, 1981). This ash could have been carried as englacial or superglacial sediment many kilometers to the west from the Andean source volcano or volcanic front. Therefore, the mixed provenance of Site 861 silt and sand-sized sediment, along with the poorly sorted nature of the sediments (see discussion in Lithostratigraphy section, Site 859 chapter) suggests a Pliocene/Pleistocene glacial origin for these materials.

Glacial ablation along the shelf edge would serve as a distribution method that could bypass the shelf and funnel sediment out onto the continental slope. Sediment release from ice shelves takes place close to their grounding lines (Drewry, 1986), so that in the case of the Chile margin, if the grounding line were proximal to the shelf edge, large quantities of material could have been released at the shelf edge and redistributed by gravity-flow processes. The grounding line may migrate in response to climate, sea level, and mass balance variations (Drewry, 1986).

Most information about glacial-marine sedimentary environments has come from studies in the Antarctic seas where glacial

Table 3. Mineralogy of sediments from Holes 861C and 861D.

Core, section, interval (cm)	Depth (mbsf)	Nonclay mineral phases (100%)				Phyllosilicates (100%)		
		Quartz	Feldspar	Hornblnd.	Calcite	Amorph.	Chlorite	Illite
141-861C-								
1H-1, 24-26	0.24	4	3	2	2	2	4	4
5H-3, 54-58	33.84	4	3	2	0	2	4	4
10H-4, 44-46	75.94	4	3	1	0	2	4	4
15X-3, 62-64	122.62	4	4	2	0	2	4	4
21X-2, 68-70	172.38	4	4	1	0	2	4	4
25X-1, 93-95	209.83	4	3	1	0	2	4	4
31X-2, 72-74	250.52	4	4	2	1	2	4	4
35X-2, 40-42	286.93	4	3	1	0	2	4	4
40X-2, 36-38	335.76	3	4	1	1	2	4	4
41X-2, 87-89	345.77	4	3	1	1	2	4	4
141-861D-								
1R-2, 24-26	344.04	4	4	1	0	2	4	4
6R-2, 18-20	391.45	4	3	2	1	2	4	3
10R-1, 77-79	429.87	4	4	1	0	2	4	4
15R-1, 47-49	476.77	4	3	1	0	2	4	4
16R-1, 119-121	487.19	4	4	1	0	2	4	4

Numbers indicate: 4. dominant, 3. secondary, 2. minor, 1. trace phases, 0. phase absent.

diamicts (matrix-supported to pebbly gravels) are restricted to a narrow zone just seaward of the calving line (Anderson, 1983; Wright et al., 1983). These poorly sorted sediments pass seaward into sediments with better sorting and stratification.

The lithologies and sequences observed in Site 861 cores could be explained using an inter-canyon gravity-flow model proposed by Wright and Anderson (1982) for sediments deposited in the Weddell Sea (Fig. 14). In their model, slumps/slides of glacial-

marine sediments originate along the outer shelf and move downslope. As the resulting debris flow travels downslope, it entrains fluid and becomes partially suspended, fluidized, and sorted. Some fine-grained sand and mud may be sheared from the head of the debris flow, forming a cap of turbulently suspended sediment above the flow. The debris flow may continue downslope, eventually producing fine-grained turbidites. These turbidites are deposited within 10 km of the shelf break, on slopes

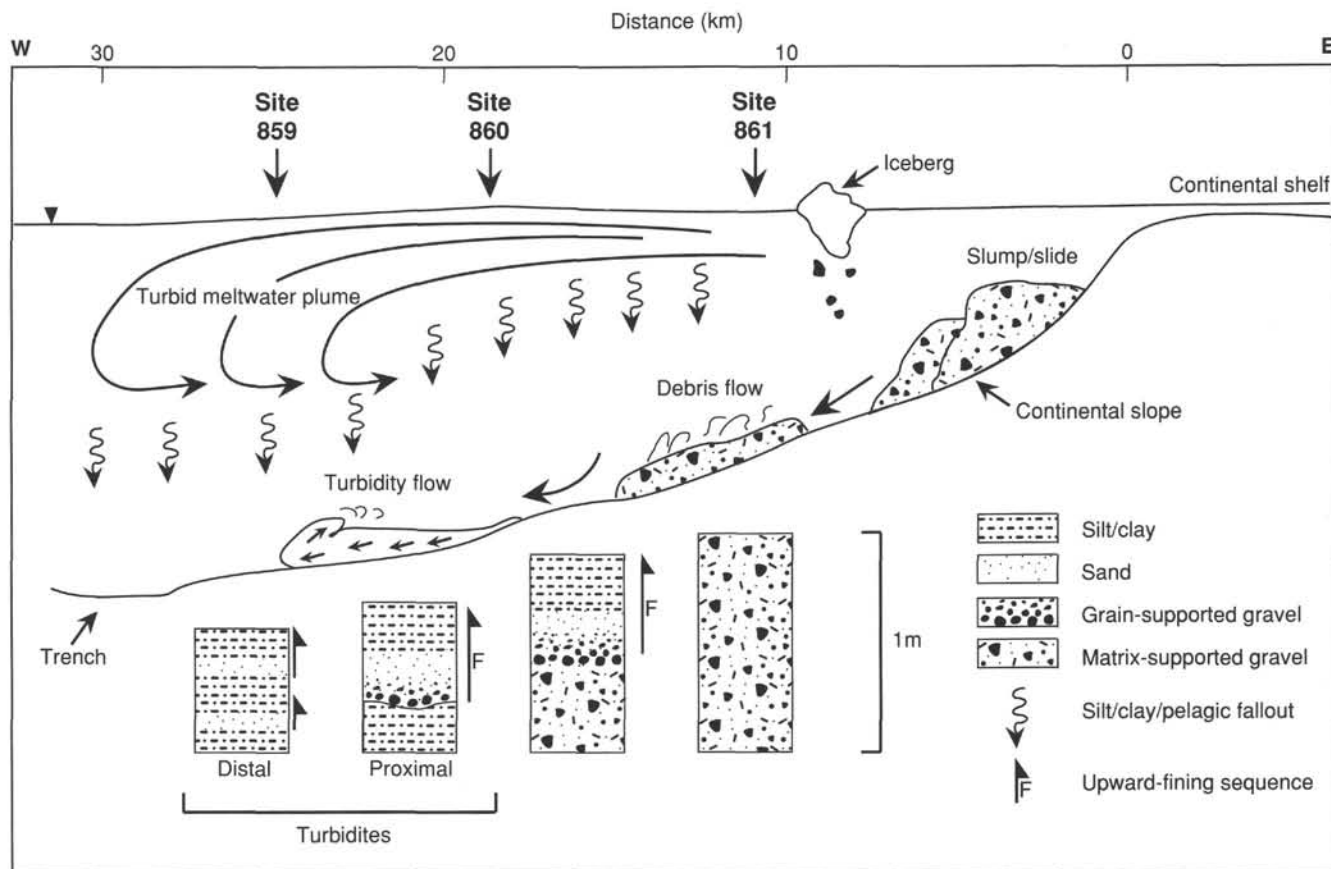


Figure 14. Possible depositional model for sediments recovered at Sites 859, 860, and 861. Figure modified from depositional model proposed by Wright and Anderson (1982) for Weddell Sea sediments. The scale of the various gravity-flow processes is exaggerated.

with gradients averaging 5° to 9°; deposition is controlled by upper slope irregularities, such as those produced by slump deposits, which form local base levels for turbidite deposition (Wright and Anderson, 1982). A similar glacial-marine, slope-deposit model has been proposed by Miall (1983, 1985) for ancient sequences. Because both of these models concern passive margin sequences, the added slope instability due to seismicity must be taken into account when applying these models to active continental margins such as the South American margin.

According to the model proposed by Wright and Anderson (1982), the massive-to-thin ungraded, matrix (mud)-supported conglomerates (debris flows/diamicts) of Subunit IIB are more proximal units, and these pass into more distal facies (sandy/silty turbidites displaying partial Bouma sequences) in Subunit IIA, and perhaps into extremely distal facies represented by the partially redistributed silty laminae in Unit I (muddy turbidites). Transitional facies are recorded in sequences that pass upward from a matrix-supported gravel unit (debris flow/diamict) into a grain-supported gravel (Fig. 10) and then a graded unit (Fig. 12). In light of this model, uphole changes in sedimentation at Site 861 could be explained by successive periods of glacial advance and ablation during the Pliocene/Pleistocene (Rabassa and Clapper-ton, 1990). More information is needed about the onshore Pliocene/Pleistocene record of glacial advance and retreat along the continental margin to test the validity of this glacial model for the sedimentary sequence recovered at Site 861.

In more temperate, nonpolar glacial environments, meltwater plays a more important role in supplying sediment to the ocean; the rapid sediment supply produces silts and clays with only minor ice-rafted debris, in contrast to the matrix-supported to pebbly gravel units (diamicts), which are more prevalent in polar environments (Anderson, 1983). Therefore, depending on the glacial affinity of Chile during the Pliocene/Pleistocene (temperate vs. polar), some of the graded units could have been initiated by sudden high-discharge events within the ice sheet (jökulhlaups), or perhaps be related to seasonal high flow/discharge of meltwater. High apparent sedimentation rates could reflect proximity to a glacial meltwater stream system, which could blanket the slope and its basins with silt and clay via settling from sediment-laden, turbid plumes. In southern Alaska, a temperate glacial regime exists, and clayey silt is carried seaward as suspended sediment plumes from glacier termini or rivers (Molnia, 1983). Estimates of sedimentation rates at this margin range from 0 to 29 mm/yr (Molnia, 1983). The rates estimated for Pliocene-Pleistocene sediment accumulation at Sites 859, 860, and 861 lie well within this range.

BIOSTRATIGRAPHY

Introduction

Site 861 is the easternmost site of the Leg 141 west-east transect along approximately the 45°S parallel. This site, which is located most landward and at the shallowest water depth, displays the most frequent and abundant microfossil occurrences of the three sites along the transect (Fig. 15). However, the overall pattern of microfossil occurrence within the sediments at Site 861 is low. This is probably due to a combined effect of dilution and dissolution.

Sediments recovered from the seafloor to 496.3 mbsf, the deepest penetration at Site 861, represent a stratigraphic sequence from the Quaternary through Pliocene (Figs. 16 and 17).

Although the occurrence of diatoms and radiolarians is slightly more frequent than at Sites 859 and 860, in general, biogenic silica at Site 861 can be regarded as a minor or trace component of the sediment. Consequently, these taxa are of limited stratigraphic

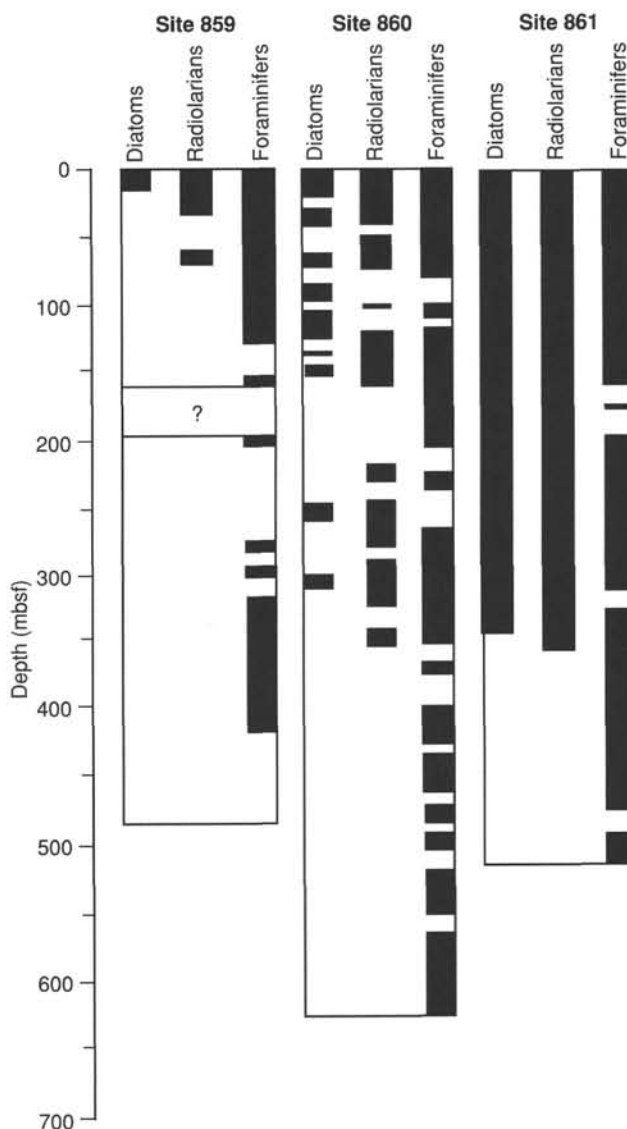


Figure 15. Qualitative occurrence charts for microfossil groups investigated on board for sites along the 45°S east-west transect.

value. Foraminifers are few, with the exception of the upper Pleistocene portion where they are more common. The consistent occurrence of benthic foraminifers throughout the sequence (96% of the core-catcher samples) permits determination of the water depth at the time of their deposition in the sediment. The calcareous nannofossils investigated by shore-based studies (C. Müller) are generally few to rare in the Pleistocene sequence, but become more common with slightly more diversified assemblages within the Pliocene sequence.

Based on the results obtained by the different fossil groups, age discrepancies exist for the Pleistocene sequence. Further investigations will be necessary.

Diatoms

Three core-catcher samples (141-861C-1H-CC, -7H-CC, and -8H-CC) are assigned to the *Pseudoeunotia doliolus* Zone (NTD 17) at Site 861 based on the rare occurrence of *P. doliolus* without *Nitzschia reinholdii* and *Nitzschia fossilis*. In low latitudes, the base of NTD 17 is placed in the lower portion of the Brunhes Chron and has an estimated age of 0.65 Ma (Burckle, 1977).

Hole 861C

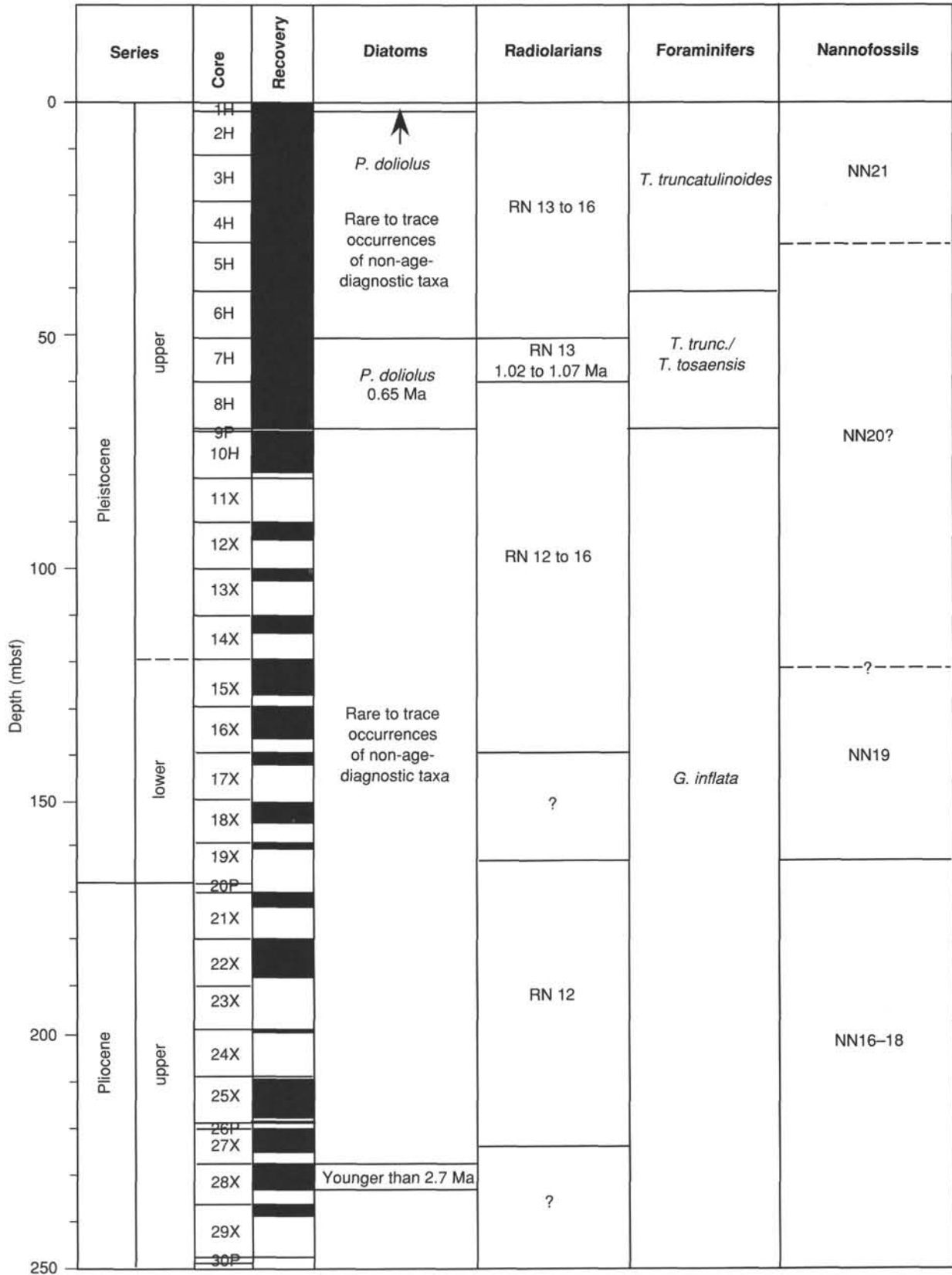


Figure 16. Summary of biostratigraphic age for the sediments recovered at Hole 861C.

Hole 861C

		Series	Core	Recovery	Diatoms	Radiolarians	Foraminifers	Nannofossils
Depth (mbsf)	Pliocene upper		31X		Rare to trace occurrences of non-age-diagnostic taxa	?	<i>G. inflata</i>	NN16-18
			32X					
			33X					
			34X					
			35X					
			36X					
			37X					
			38X					
			39X		Barren			
			40X					
			41X					
							Barren	

Figure 16. (Continued).

Diatoms were encountered in all core-catcher samples from the top down to 328 mbsf (Sample 141-861C-38X-CC), whereas below this level samples were barren. All diatom-bearing samples, apart from those assigned to NTD 17, contain only traces or rare occurrences of non-age-diagnostic taxa, with the exception of a few scattered occurrences of *Nitzschia kerguelensis*. Sample 141-861C-28X-CC is the lowermost sample that contains a few *N. kerguelensis*, which indicates that sediments at 235 mbsf are younger than 2.7 Ma.

Radiolarians

Radiolarians of moderate-to-poor preservation are found in all of the core-catcher samples from the top down to 362 mbsf (Sample 141-861D-2R-CC) at Site 861. Below 410 mbsf the cores are barren of radiolarians. Radiolarian age assignments were possible from the top of Hole 861C to Sample 141-861C-2X-CC (228 mbsf) with an interruption by one interval consisting of non-age-diagnostic assemblages (Fig. 16). Below 228 mbsf, although radiolarians are present, the assemblages consist of poorly preserved non-age-diagnostic taxa, and hence no relevant age information can be provided. This interval is followed by a barren zone extending to the bottom of Hole 861D.

Preservation of radiolarians improved progressively along the west to east transect from Site 859 through Site 860 to Site 861 (i.e., moving landward) (Fig. 15). This can be explained in terms of either productivity or preservation. Currently available data suggest that differences in thermal activity (i.e., distance from the rift center) may be one of the most important factors that contribute to the preservation conditions. It has been observed that the higher the thermal activity, the lower the porosity (see porosity data in Fig. 42 in Physical Properties section, this chapter).

Samples 141-861C-1H-CC through -6H-CC can be assigned to the *Anthocyrtdium angulare* (RN13) to *Buccinosphaera invaginata* (RN16) Zones of the Pleistocene to Holocene mainly by the occurrences (few to rare) of *Lamprocyrtis nigrinae*. This

assignment is supported by co-occurring taxa such as *Eucyrtidium erythromyrtax* and *Antarctissa denticulata*.

Sample 141-861C-7H-CC contains a few *Lamprocyrtis neohetroporos* and rare *L. nigrinae* that place the age of this sample (if they are not reworked) close to the datum level 1.07–1.02 Ma (Nigrini, 1991). The former species is the ancestor of the latter and these two taxa are, in normal circumstances without reworking, found together only at or in the vicinity of the evolutionary transition.

Samples 141-861C-8H-CC to -16X-CC are assigned to the *Pterocanium prismatium* (RN12) to *Buccinosphaera invaginata* (RN16) Zones of the upper Pliocene to Holocene. Representative taxa in this interval, consisting of poorly preserved radiolarians, include *Cycladophora davisiana davisiana*, *A. denticulata*, and *Spongurus (?) pylomaticus*. Samples 141-861C-17X-CC through -19X-CC are represented only by stratigraphically insignificant taxa and thus no relevant age can be provided other than to indicate that they are in the Pliocene or younger. Samples 141-861C-20X-CC through -22X-CC are assignable to the *P. prismatium* (RN12) of the upper Pliocene as they contain the age marker *Lamprocyrtis hetroporos* together with *Axoprunum angelinum*, and *C. d. davisiana*, which were also found in Samples 141-861C-24X-CC and -27X-CC. Below this interval the core-catcher samples down to 362 mbsf are represented only by non-age-diagnostic taxa, followed by a barren zone through to the bottom of Hole 861D (496 mbsf).

Planktonic Foraminifers

Planktonic foraminifers are abundant and well preserved in Hole 861C from the top down to Sample 141-861C-5H-CC (Tables 4 and 5). Below this sample down to Sample 141-861C-20P-CC, well-preserved planktonic foraminifers are mostly common. Below Sample 141-861C-20P-CC and throughout the whole sequence penetrated in Hole 861D they are rare and poorly preserved.

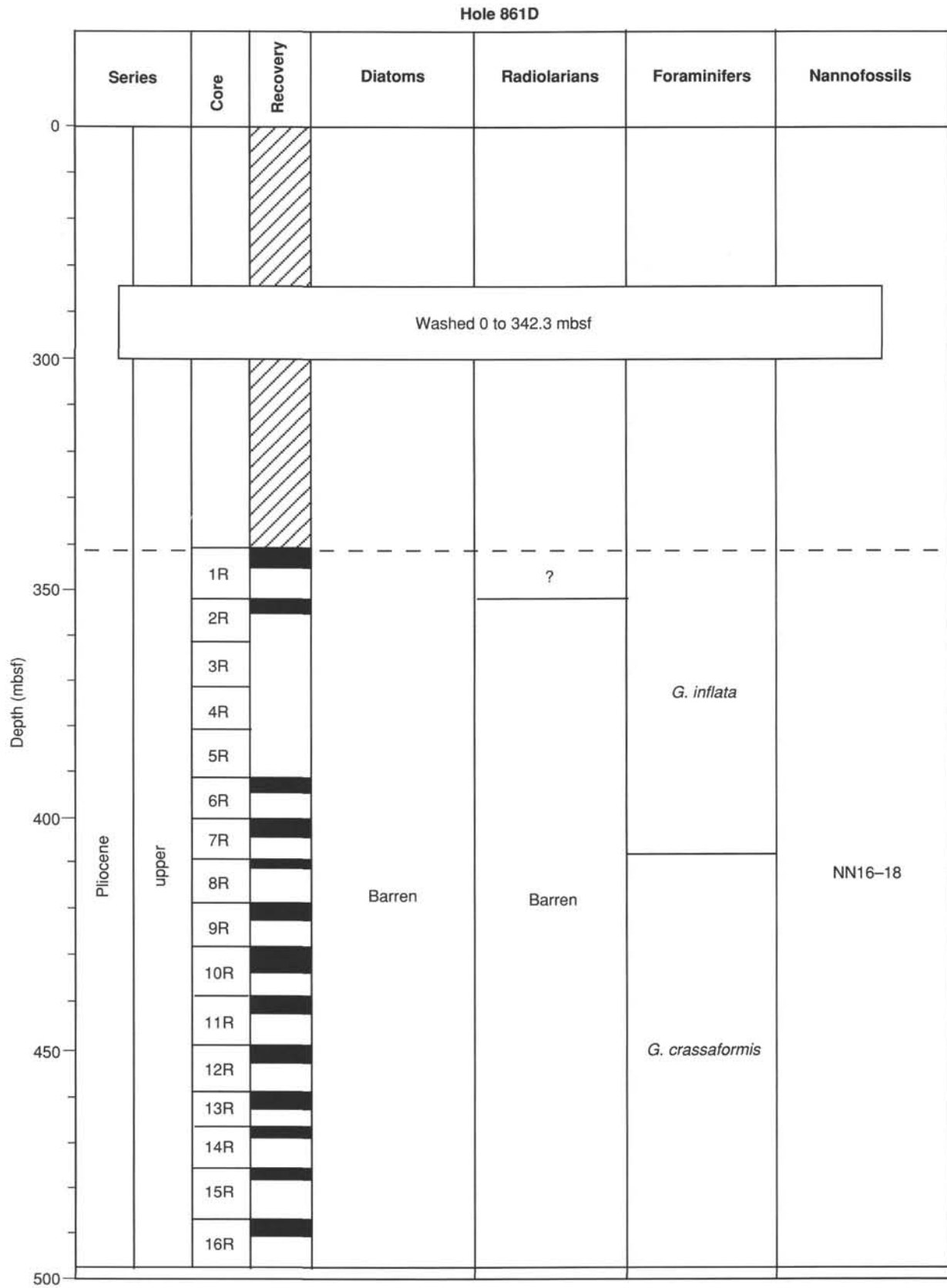


Figure 17. Summary of biostratigraphic age for the sediments recovered at Hole 861D.

Table 4. Occurrence, preservation, and estimated relative abundance of planktonic foraminifers of samples from Hole 861C.

Sample	Depth (mbsf)	Abundance	Preservation	<i>T. truncatulinoides</i>	<i>T. tosaensis</i>	<i>O. universa</i>	<i>G. bulloides</i>	<i>B. digitata</i>	<i>G. cariacensis</i>	<i>N. dutertrei</i>	<i>G. inflata</i>	<i>G. scitula</i>	<i>G. crassaformis</i>	<i>G. crassula</i>	<i>N. pachyderma D</i>	<i>N. pachyderma S</i>	Paleotemperatures	Zones
141-861C-1H-CC	3.00	A	G	G		R	R	R	C	R	C	R	R				Subtropical	<i>Truncorotalia truncatulinoides</i>
2H-CC	12.50	A	G	F			C	R	R		C	R		R	R		Warm to temperate	
3H-CC	22.00	A	G	F		R	A		R		A		R					Cold to temperate
4H-CC	31.50	A	G	R			R				A							
5H-CC	41.00	A	G	F		R	C				A	R	R					
6H-CC	50.50	F	M	R	R		C				F			C	R			
7H-CC	60.00	C	G	R	R	R	F				C							
8H-CC	69.50	C	G	R	R		R				C							
9P-CC, 14 cm	69.64	C	G			R	F	R			C							
9H-CC	69.73	C	G				C				C	R						
10H-CC	79.97	C	G				R				C	R						
11X-CC	80.55	C	G								R							
12X-CC	92.82	C	G				C				R	R		R	R			
13X-CC	101.10	R	M				R				R			R	F			
14X-CC	112.54	F	M				R				R			R	F			
15X-CC	126.83	C	G				R				F			R				
16X-CC	136.12	R	P				R				R			R				
17X-CC	141.37	C	G				F				R			R				
18X-CC	154.18	C	G				F				F	R		R				
19X-CC	159.18	F	G				R				R			R				
20P-CC	170.20	C	G				F				F			R				
21X-CC	172.91	B									F			R				
22X-2, 89 cm	182.29	C	G			R	C				R	R	R	R				
22X-CC	188.72	B																
24X-CC	199.50	R	G				F				F							
25X-CC	217.57	R	P									R				R		
27X-CC	226.45	R	M				R					R				F		
28X-CC	234.86	R	P				R							R		R		
29X-CC	239.37	R	M			R								R				
31X-CC	252.47	R	P								R			R		R		
32X-CC	260.06	R	M				F									F		
33X-CC	269.70	R	M				R					R						
34X-CC	282.67	R	M								R					F		
35X-CC	291.08	R	P				R				R							
36X-CC	301.34	R	P				R				R							
37X-CC	308.02	R	P								R					R		
38X-CC	314.87	R	P								R					R		
39X-CC	328.65	R	P			R					R	R						
40X-CC	341.16	R	P			R	R				R							
41X-CC	349.40	B									R							

Table 5. Occurrence, preservation, and estimated relative abundance of planktonic foraminifers of samples from Hole 861D.

Sample	Depth (mbsf)	Abundance	Preservation	<i>O. universa</i>	<i>G. bulloides</i>	<i>G. inflata</i>	<i>G. crassaformis</i>	<i>N. pachyderma D</i>	<i>G. cassula</i>	<i>G. cf. sphericomiozea</i>	<i>N. pachyderma S</i>	Paleotemperatures	Zones
141-861D-1R-CC	347.56	R	M			R						Cold to temperate	<i>G. inflata</i>
2R-CC	355.18	B				R							
6R-CC	394.07	R	P		R	R				R		Cold to temperate	<i>G. crassaformis</i>
7R-CC	404.40	R	P		R	R							
8R-CC	411.02	R	P	R	R	R							
9R-CC	424.37	R	P		R	R				R			
10R-CC	430.78	R	P	R		R	R						
11R-CC	441.41	R	P		R								
12R-CC	452.13	R	P			R				R			
13R-CC	461.92	R	P			R		R	R	R			
14R-CC	469.02	B											
15R-CC	478.15	R	P			R				R			
16R-CC	489.04	R	P										

served. The entire residue was picked out to acquire enough foraminifer specimens.

The drilled sequences of Holes 861C and 861D are sediments containing assemblages of foraminifers of the Pleistocene and Pliocene. The LOD of *Truncorotalia tosaensis* in Sample 141-861C-6H-CC (50.5 mbsf) marks the boundary between the *Truncorotalia truncatulinoides*/*T. tosaensis* overlap-Zone and the *T. truncatulinoides* Zone. The *Globoconella inflata* Zone extends from Sample 141-861C-9P-1, 14 cm (69.64 mbsf), in Hole 861C through Sample 141-861D-7R-CC (404.40 mbsf) in Hole 861D, where the FOD of *G. inflata* marks the boundary between the *G. inflata* Zone and the *Globoconella crassaformis* Zone.

Paleotemperatures appear to be reflected in the assemblages containing planktonic foraminifers. Subtropical water masses are indicated in Sample 141-861C-1H-CC by the occurrence of *Beella digitata*, *Globigerina cariacensis*, *Neogloboquadrina dutertrei*, and the absence of *N. pachyderma*. The sequence of Pleistocene sediments extending from Samples 141-861C-2H-CC to -9H-3, 140–143 cm, is characterized by assemblages that are typical for warm-water masses, containing abundant *Globoconella inflata*, *Globigerina bulloides*, and a few specimens of *Orbulina universa*, *T. truncatulinoides*, and *T. tosaensis*. The transition zone between warm- and cold-water masses with warm temperate to cold-water temperatures is characterized by the occurrence of *G. inflata* (Bé and Tolderlund, 1971) and *N. pachy-*

derma in its sinistral coiling direction. This paleoenvironmental condition is represented by the assemblages of Samples 141-861C-9H-CC through -40X-CC, and it is also observed in the whole sequence drilled in Hole 861D.

Benthic Foraminifers

Benthic foraminifers (Table 6) are abundant or common and well preserved in Hole 861C sequences down to Sample 141-861C-20P-CC. Below this interval they become rare, and preservation is moderate or poor. *Bulimina mexicana*, *Uvigerina peregrina*, *Uvigerina cushmani*, *Planulina wuellerstorfi*, and *Hoeglundina elegans* are commonly encountered. Their Holocene bathymetry indicates an upper through middle bathyal environment. *U. proboscidea* and *U. hispida* both occur in Sample 141-861C-1H-CC and *Pyrgo murrhina* is rare in the interval between Sample 141-861C-1H-CC and -9H-3, 140–143 cm. They are bathyal taxa (van Morkhoven et al., 1986). *Bolivina costata* occurs in rare to few abundances in Hole 861C between Samples 141-861C-6H-CC and -16X-CC. This species dominates in Holocene oceans in mid- to outer-shelf biotopes and becomes rare below 150 through

2000 m water depths (Resig, 1990). *Uvigerina senticosa*, present in Hole 861C from the top down to Sample 141-861-16X-CC, represents an outer to middle bathyal environment. Below Sample 141-861C-17X-CC some taxa are observed that characterize middle bathyal to abyssal conditions. Sample 141-861C-20P-CC contains *U. senticosa*, which lives in Holocene benthic environments in water depths deeper than 2400 m (Boersma, 1984). *Melonis pompilioides* is scattered below Section 141-861C-18X-CC. The deep-water ecotype *M. pompilioides sphaeroides* occurs in Sample 141-861C-38X-CC. *Bolivina costata* does not occur below Sample 141-861C-16X-CC. Similar things were observed for the assemblages of Hole 861D (Table 7). At that site the observed deep-water species are *Uvigerina senticosa*, *Pyrgo murrhina*, *M. pompilioides*, and a reliable indicator for abyssal water depths, *M. pompilioides sphaeroides*. Therefore, the sediments below Sample 141-861C-16X-CC in Hole 861C and the entire sequence drilled in Hole 861D show abyssal to middle bathyal conditions. In contrast, the Pleistocene assemblages show middle bathyal to upper bathyal conditions. Samples containing taxa indicative of shelf deposition are marked in Table 6 by asterisks. They are common in the sequence from the top of the Hole 861C through

Table 6. Occurrence, preservation, and estimated relative abundance of selected benthic foraminifers of samples from Hole 861C.

Sample	Depth (mbsf)	Abundance	Preservation	Displaced sediments	<i>Bulimina mexicana</i>	<i>Uvigerina peregrina</i>	<i>Planulina wuellerstorfi</i>	<i>Pyrgo murrhina</i>	<i>Melonis pompilioides</i>	<i>Melonis pomp. sphaeroides</i>	<i>Uvigerina proboscidea</i>	<i>Uvigerina hispida</i>	<i>Uvigerina cushmani</i>	<i>Uvigerina senticosa</i>	<i>Hoeglundina elegans</i>	<i>Noninella cf. turgida</i>	<i>Bolivina costata</i>	<i>Rosalina peruviana</i>	<i>Bulimina marginata</i>	<i>Nodogenerina bradyi</i>	<i>Macronia</i> sp.	Paleoenvironment
141-861C-1H-CC	3.00	A	G	*	F	F	F	R			R	F		F	R	R		F				
2H-CC	12.50	A	G	*	F	R	R					R			R	R						
3H-CC	22.00	A	G	*	F	F	F	R				F		F	R	R						
4H-CC	31.50	A	G	*	F	R	R					F		F	R	R						
5H-CC	41.00	A	G	*	R	R	F					F		F	R			R				
6H-CC	50.50	F	M			R	R															
7H-CC	60.00	C	G			F	R	R														
8H-CC	69.50	C	G		C	C								R			R					
9P-CC, 14 cm	69.64	C	G		F	C	F	R					F	R			R					
9H-CC	69.73	C	G	*	R	C	R					R		R			R	R				
10H-CC	79.97	C	G			R						R		R			R	F				
11X-CC	80.55	C	G	*	R		R					C		R			R	F	R			
12X-CC	92.82	C	G	*	F							C		R			R	R	R			
13X-CC	101.10	R	M	*	R							R		R	R		R	R	R			
14X-CC	112.54	F	M	*	R	R	R					F		R	R		R	R	R			
15X-CC	126.83	C	G	*	R	R	R					F		R	R		R	R	R			
16X-CC	136.12	R	P	*	R	R						F		R	R		F	R	R			
17X-CC	141.37	C	G			R						F		R	R							
18X-CC	154.18	C	G		F	F						R		R	R							
19X-CC	159.18	F	G		F	F		R				R		R	R							
20P-CC	170.20	C	G	*	C	F	R					R	R	R	F				R			
21X-CC	172.91	B																				
22X-2,89 cm	182.29	F	M		F	F		R						F								
22X-CC	188.72	B																				
24X-CC	199.50	R	G			F						R	F									
25X-CC	217.57	R	M		R	R							R									
27X-CC	226.45	R	M		R	R														R	R	
28X-CC	234.86	R	M		R															R	R	
29X-CC	239.37	R	P		R	R														R	R	
31X-CC	252.47	R	M	*		R									R					R	R	
32X-CC	260.06	R	M		R	R														R	R	
33X-CC	269.70	R	M		R	R	R		R											R	R	
34X-CC	282.67	R	M		R	R						R										
35X-CC	291.08	R	P																			
36X-CC	301.34	R	M																			
37X-CC	308.02	R	P		R																	
38X-CC	314.87	R	P		R			R		R				R								
39X-CC	328.65	R	M		F		R	R		R										R	R	
40X-CC	341.16	R	P		R	R	R															
41X-CC	349.40	R	P																			

Middle to upper bathyal

Abyssal to middle bathyal

Table 7. Occurrence, preservation, and estimated relative abundance of selected benthic foraminifers of samples from Hole 861D.

Sample	Depth (mbsf)	Abundance			Preservation	<i>Bullimina mexicana</i>	<i>Uvigerina peregrina</i>	<i>Planularia wuellerstorfi</i>	<i>Pyrgo murrhina</i>	<i>Melonis pompilioides</i>	<i>Melonis pomp. sphaeroides</i>	<i>Uvigerina senticosa</i>	<i>Hoeglundina elegans</i>	<i>Nodogenerina bradyi</i>	<i>Maerionia</i> sp.	Paleoenvironments
		R	P	F												
141-861D-1R-CC	347.56	R	P			R						R	R			Abyssal to middle bathyal
2R-CC	355.18	R	P													
6R-CC	394.07	R	M		R			R	R	R			R	R		
7R-CC	404.40	R	P			R	R							R		
8R-CC	411.02	R	M		R									R		
9R-CC	424.37	R	P					R						R		
10R-CC	430.78	R	P										R	R		
11R-CC	441.41	R	P						R		R		R			
12R-CC	452.13	R	P		R				R		R					
13R-CC	461.92	R	P								R			R		
14R-CC	469.02	B														
15R-CC	478.15	R	P	F				R					R			
16R-CC	489.04	R	P													

Sample 141-861C-16X-CC, are scattered in the deeper part, and occur in Samples 141-861C-29P-CC and -31X-CC. Displaced taxa were not observed in the assemblages of Hole 861D.

Calcareous Nannofossils

Results from Hole 861C were obtained by investigation of 41 core-catcher samples. Nannofossils are generally few to rare. They become more common within the Pliocene sediments. Their scarcity is most probably the result of dilution by a significant influx of detrital material. The low-diversity of the assemblages is caused primarily by low-water temperatures and secondarily by selective dissolution.

Cores 141-861C-1H to -4H belong to the upper Pleistocene (*Emiliania huxleyi* Zone, NN21). Well-preserved nannofossils are common, with the following assemblages: *Helicosphaera carteri*, *Coccolithus pelagicus*, *Cyclococcolithus leptoporus*, *Gephyrocapsa oceanica*, *Gephyrocapsa ericsonii*, and *Emiliania huxleyi*. *Oolithothus fragilis* and *Pontosphaera syracusana*, which normally indicate warmer water temperatures, are extremely rare in Samples 141-861C-1H-CC and -3H-CC. Sporadic reworked species from older strata were observed. Samples 141-861C-5H-CC to -6H-CC are poor in nannofossils. *Coccolithus pelagicus*, a cold-water type, is the most common species. This circumstance might be due to a relative enrichment due to selective dissolution of the more fragile species. Sample 141-861C-7H-CC is barren of nannoplankton. The interval from Core 141-861C-8H to -13X (69.50 – 101.10 mbsf) is very poor in nannofossils, with the following species present: *Gephyrocapsa ericsonii*, *Gephyrocapsa oceanica*, *Coccolithus pelagicus*, and *Cyclococcolithus leptoporus*. This interval probably still belongs to the upper Pleistocene (Zone NN20). However, the assemblages are too poor to give a precise age. The diatom *Pseudoemuntia doliolus* Zone corresponding to the upper part of Zones NN19–NN21, was recognized in Sample 141-861C-8H-CC. However, radiolarian and foraminifer assemblages indicate that this interval falls in the lowermost Pleistocene. Nannofossils are more common from Cores 141-861C-15X to -19X. The interval belongs most probably to the lower Pleistocene (Zone NN19), as suggested by the very rare appearance of *Pseudoemiliania lacunosa* and the presence of a larger variety of the genus *Gephyrocapsa* similar to *Gephyrocapsa oceanica*. Additional *Cyclococcolithus macintyreii* was not observed. It might be that the lowermost part of the

Pleistocene is missing as indicated by the absence of *Helicosphaera sellii* that has its last occurrence at 1.2 Ma.

The Pliocene was recognized over the interval from Cores 141-861C-20X to -41X by the presence of *Cyclococcolithus macintyreii* and a very small variety of the genus *Gephyrocapsa*.

Hole 861D was washed down to 342.30 mbsf. The results obtained from this hole are based on the investigation of 16 core-catcher samples. The entire sequence is assigned to the upper Pliocene (Zones NN 16 - NN 18). A further subdivision is impossible. Nannofossils are rare to common. The assemblage consists of the following species: *Helicosphaera carteri*, *Helicosphaera sellii*, *Coccolithus pelagicus*, *Pseudoemiliania lacunosa*, *Cyclococcolithus macintyreii*, *Cyclococcolithus leptoporus*, *Gephyrocapsa* sp., and rare specimens of *Baarudosphaera bigelowi*, *Pontosphaera pacifica*, *Discolithina japonica*, *Syracosphaera pulchra*, and *Syracosphaera mediterranea*. The more common occurrence of *Pontosphaera pacifica* and *Discolithina japonica* within the upper Pliocene has also been observed from many other areas. A few specimens of the small variety of *Reticulofenestra pseudoumbilica* were also found in the sequence cored at Hole 861D. Very rare, reworked nannofossils from the middle to lower Miocene were found. The oldest sediments from Hole 861D are not older than 3.4 Ma.

PALEOMAGNETISM

Introduction

Magnetic remanence measurements using the pass-through cryogenic magnetometer were performed on APC, XCB, and RCB archive-half sections from Holes 861A, 861B, 861C, and 861D. Both Holes 861A and 861B were terminated after a single core failed to record the mudline; Hole 861C penetrated to 353 mbsf and Hole 861D recovered core from 342 to 486 mbsf. Alternating field (AF) demagnetization measurements were conducted at 10 and 15 mT on these sections at intervals of 10 cm. Orientation was successfully performed on APC Cores 141-861C-7H, -8H, and -10H with the Tensor tool. Discrete samples were also measured; stepwise AF demagnetization with very closely spaced intervals was continued up to 60 mT on the discrete samples. Magnetic susceptibility measurements on the multisensor track (MST) were performed routinely on whole-round sections.

Remanence and Susceptibility—Continuous Sections

Figure 18 records the variation with sub-bottom depth of natural remanent magnetization (NRM) inclination before demagnetization, and inclination and intensity after 15-mT demagnetization of the archive-half sections in Hole 861C. Even after demagnetization, most of the sequence remains normally polarized. In relatively young sediments of normal polarity, it can be difficult to distinguish whether the magnetization is one acquired originally in a direction close to that of the present-day field or whether it is a recently acquired overprint. Following 15-mT demagnetization, some parts of the sequence show a dispersal of inclination values and a spread to positive inclinations (i.e., reverse polarities) accompanied by a 5- to 10-fold decrease in intensity (e.g., over the intervals 40–60, 170–190, and 325–350 mbsf). It may also be the case that intervals in which the inclination tends toward low absolute values after demagnetization are reversely polarized, even if the inclination remains negative. Such an analysis suggests that the magnetic record is heavily overprinted. Consequently, our ability to define a magnetostratigraphy was severely limited.

Comparison of demagnetized intensity records reveals that the first 6–7 m of the sequence from Holes 861B and 861C are missing from Hole 861A. Figure 19 shows the correlation of an

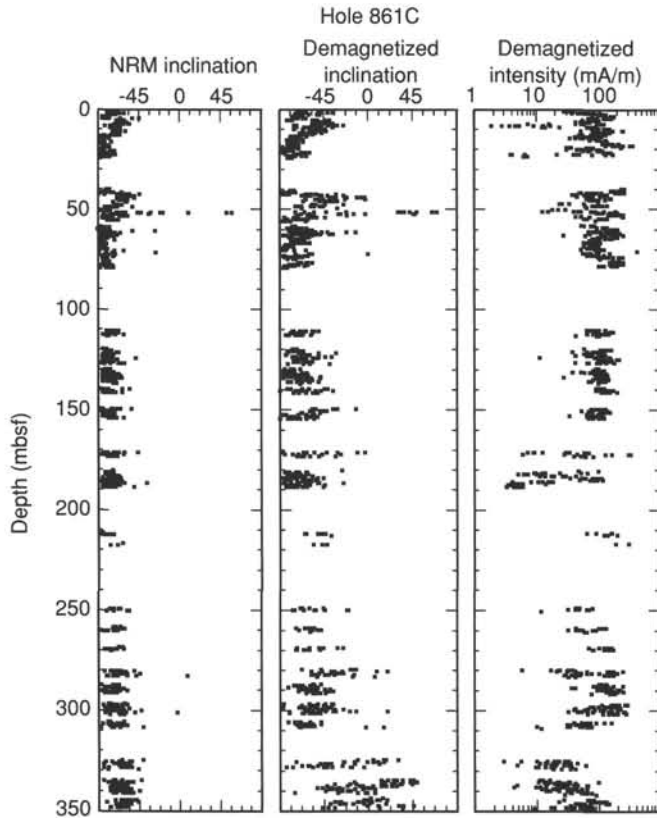


Figure 18. NRM inclination, demagnetized inclination, and demagnetized intensity for Hole 861C.

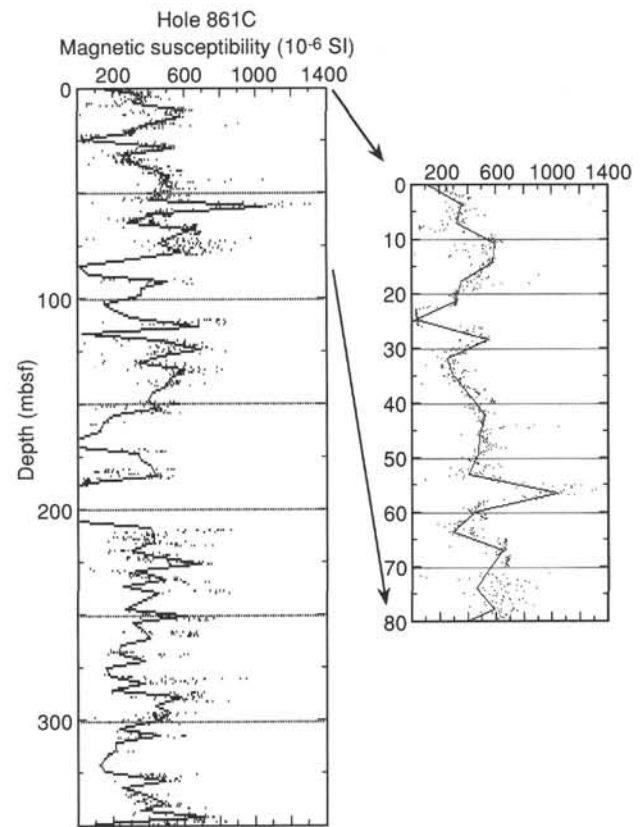


Figure 20. Magnetic susceptibility (SI) vs. depth for Hole 861C.

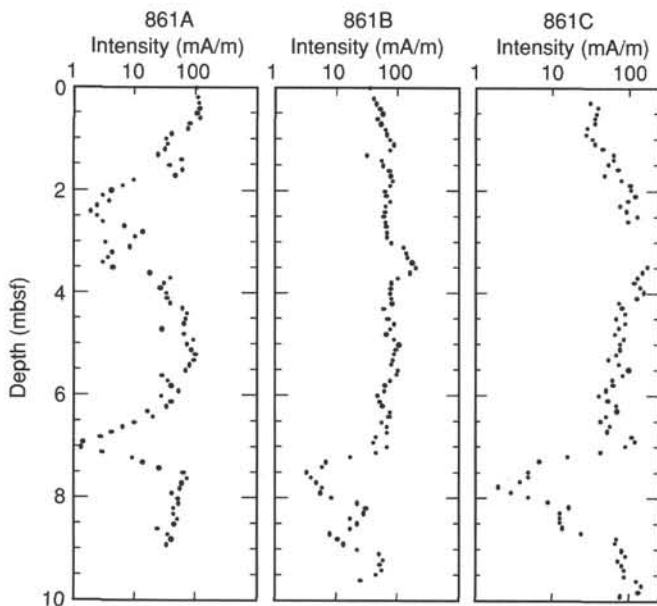


Figure 19. Intensity after 15-mT demagnetization for Holes 861A, 861B, and 0–10 mbsf from Hole 861C.

interval exhibiting a characteristic pattern of low intensity after 15-mT demagnetization, which occurs at around 7.5–8 mbsf in Holes 861B and 861C and at about 2.5 mbsf in Hole 861A.

Figure 20 shows the record of magnetic susceptibility in Hole 861C. Although it is discontinuous and irregular, average suscep-

tibility seems to be between 400 and 500×10^{-6} SI. In the upper part of the hole are three large (but very narrow) peaks at about 19–20, 45, and 55 mbsf. As we observed in Hole 860B, these susceptibility peaks correspond to sand layers in which presumably there are higher ferromagnetic mineral concentrations. Below 80 mbsf the susceptibility varies between 10 and 80 mbsf, with an average of 460×10^{-6} SI.

Demagnetization of Discrete Samples

Demagnetization of discrete samples from Hole 861C is illustrated in Figure 21. Inclination in Samples 141-861C-12X-2, 3–5 cm, -14X-2, 9–11 cm, -15X-4, 7–9 cm, and -16X-4, 83–85 cm, from the upper structural domain (see Structural Geology section, this chapter) remains steeply negative despite demagnetization to 40–60 mT. Below 25 mT a soft component is removed. Above this demagnetization level the remanence vectors trend along a roughly linear path toward the origin of the Zijderveld plot, and so define a characteristic remanence (ChRM). The inclination of the ChRM is approximately what would be expected for the normal dipole field.

Sample 141-861C-41X-2, 25–27 cm, was taken in the middle structural domain at 345.15 mbsf, corresponding to a zone of shallow-negative to positive inclination. This sample clearly displays a reversed polarity ChRM with a large normal overprint, confirming the suspicion that normal overprinting obscures reversed polarity intervals in the 15-mT cryogenic magnetometer record. Sample 141-861D-16R-3, 30–32 cm, from the broken formation, is also clearly overprinted, but this overprint is of reversed polarity. VRM can only result in a normal polarity overprint; thus, the behavior of this sample indicates that another remagnetization process must have taken place, at least near TD in the broken formation.

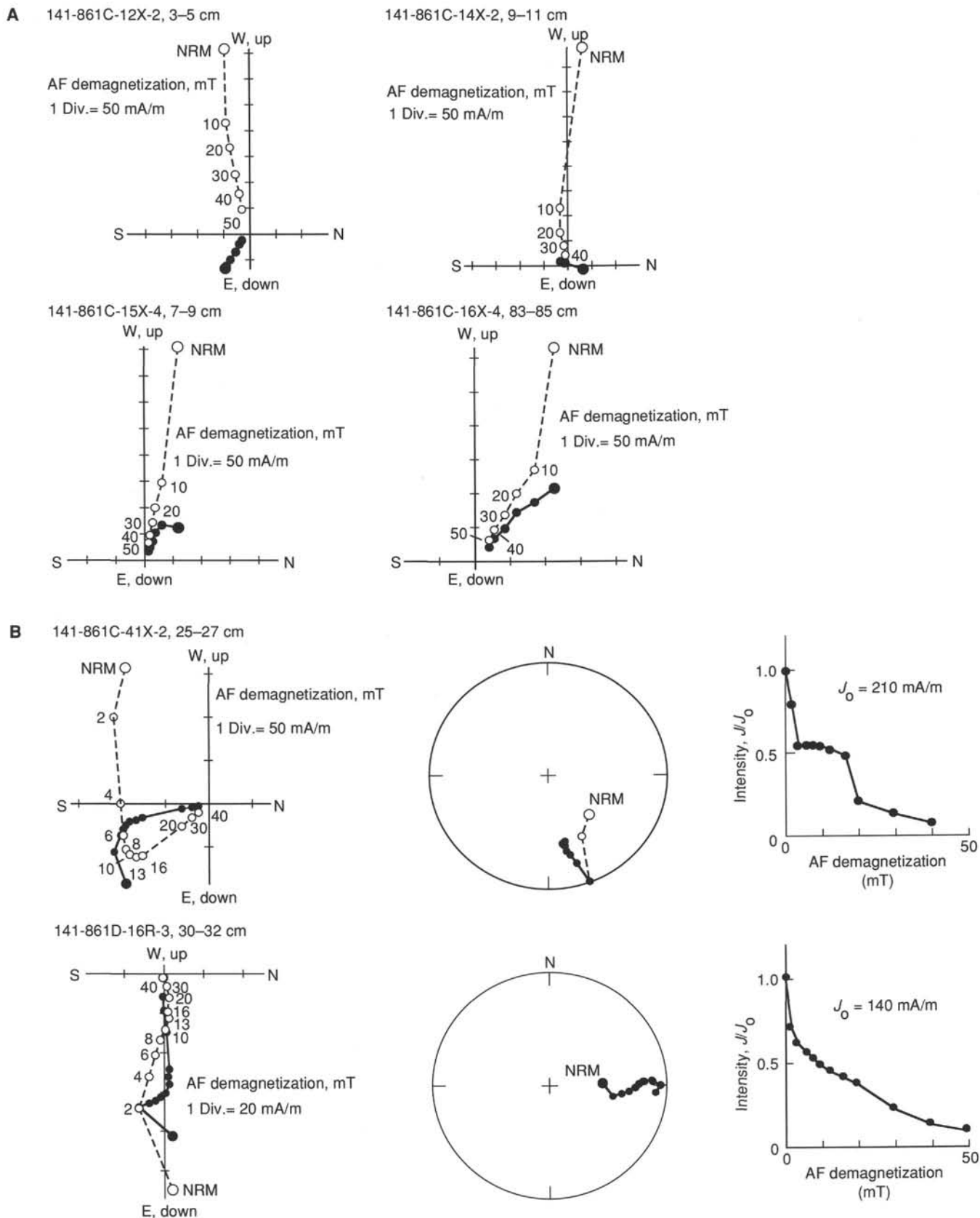


Figure 21. A. Zijderveld plots of discrete samples from the upper structural domain at Site 861. Open symbols are on the vertical/north-south plane, closed symbols on the horizontal plane. B. Zijderveld, stereogram, and intensity plots of Sample 141-861C-41X-2, 25–27 cm, from the middle structural domain, and Sample 141-861D-16R-3, 30–32 cm, from the broken formation. Open stereogram symbols are upper hemisphere, closed stereogram symbols are lower hemisphere.

STRUCTURAL GEOLOGY

Summary

The structural stratigraphy at Site 861 (Fig. 22) is similar to that described at Site 860 (see Structural Geology section, Site 860 chapter, this volume). An upper domain of flat to shallowly bedded sediments (0–210 mbsf), containing few mesoscopic structures, overlies a domain of flat to moderately dipping bedded sediments that contain isolated deformation bands (210–420 mbsf). Below 420 mbsf, deformation bands form intense networks. Bedding surfaces are less commonly observed and more variable in dip. The change from isolated to intense deformation bands is transitional over 30 m (390–420 mbsf). Strata are disrupted, and by comparison with Site 860 the lowermost domain (420–496.3 mbsf) is probably a broken formation. No major thrusts can be constrained within the succession at Site 861, although shear-zone-type fabrics similar to those at Site 860 occur at 489 mbsf, close to the deepest level penetrated.

Detailed structural data recorded on spreadsheets for Holes 861A, 861B, 861C, and 861D are presented in Table 8. Although multishot and Tensor tools were run on Cores 141-861C-7H, -8H, and -10H, the bedding in these cores is close to flat lying and rotation of the data has little effect on the distribution. Rotations have not been applied to data presented.

Upper Domain

Bedding orientations in the core reference frame are shown in Figure 23. Most of the bedding has true dips of less than 15°. The steeper bedding observed (up to 44° true dip) is concentrated in the upper part of Hole 861C and in Holes 861A and 861B, suggesting that these may relate to near-surface slump folds such as those observed at Sites 859 and 860. No mesoscopic structures such as faults or folds were observed in this domain. Fragments within drilling breccias in the deeper XCB cores of this domain (Cores 141-861C-18X through -24X) exhibit an incipient fissility related to increasing degree of lithification at this depth.

Middle Domain

The first deformation band, observed in Sample 141-861C-25X-2, 65–67 cm, is used to define the upper boundary of the middle domain. Bedding in the middle domain is flat to moderately dipping (Fig. 24). Deformation bands in this domain are similar to those observed in the thrust stack domain of Site 860 (see Structural Geology section, Site 860 chapter, this volume). Deformation bands comprise anastomosing, fine (generally <0.5 mm) dark seams. At Site 861, the transition from isolated deformation bands to intense networks appears to be transitional. For example, two sets of deformation bands are observed within Sample 141-861D-6R-2, 25–29 cm, below which the style changes back to isolated single deformation bands for the rest of that core.

Pyrite is observed throughout Site 861 below Section 141-861C-3H-6, 56–61 cm. Most pyrite is disseminated or in concretions. In Sample 141-861C-32X-1, 105–106 cm, fine framboidal pyrite fills a 2-mm-thick planar zone that may be a deformation band. Many deformation bands at deeper levels contain fine (submillimeter) pyrite.

Broken Formation

Cores below about 420 mbsf contain intense networks of deformation bands. The first appearance of an intense network of deformation bands is in Sections 141-861D-9R-1, 46 cm, through -9R-2, 13 cm. Although many lithologic boundaries coincide with deformation bands and strata have been disrupted (e.g., Section

141-861D-13R-1, 49–59 cm), unmodified bedding surfaces are observed with a range of orientations from shallow to steep (Fig. 25). Flat-lying graded bedding is observed at Section 141-861D-10R-1, 47–51 cm.

Deformation bands exhibit much the same mesoscopic characteristics as deformation bands in the broken formation at Site 860 (see Structural Geology section, Site 860 chapter, this volume), although some variations are observed. For example, in Sample 141-861C-32X-1, 105–106 cm, a thin deformation band is surrounded by 0.3 mm of breccia that extends for at least 4 mm along the deformation band (Fig. 26).

Deformation band orientations exhibit no overall pattern (Fig. 27). Rotary drilling in Hole 861D caused considerable disturbance so that, generally, the deformation band networks are poorly preserved. Together with the shallow penetration of the broken formation, this means that it is not possible to establish domains of contrasting strain and kinematics on the 10 to 100 m scale, as was possible at Site 860 (see Structural Geology section, Site 860 chapter, this volume).

In Sections 141-861D-13R-1, 49 cm, through -14R-1, 62 cm, steeply dipping, interconnected, curvilinear deformation bands offset shallowly dipping deformation bands and lithologic layering with mixed reverse and normal separations. In turn, the steep set of deformation bands is offset by isolated steep deformation bands having a planar geometry. In Section 141-861D-14R-1, 90–100 cm, steeply dipping deformation bands are cut by shallowly dipping deformation bands with mixed separations.

The most coherent sequence of broken formation structures is observed in Sections 141-861D-16R-2, 20 cm, through -3, 40 cm. In the upper part of this interval (Fig. 28), steep anastomosing deformation bands spaced 1–4 mm apart are cut by a set of planar shallow deformation bands spaced 8–15 mm apart with reverse separations of up to a centimeter. Dipping shallowly in a direction opposite to the main set of shallow deformation bands are finer and more widely spaced deformation bands. These cut the steep deformation bands, giving rise to normal separations up to a few millimeters and usually terminating against the main set of shallow deformation bands. The base of this unit is a fault (or a deformation band: the surface is not exposed), with a shallow dip opposite to the dip of the main set of shallow deformation bands. Below the fault is a 15-cm unit with very few deformation bands, bounded at the base by a discrete, 0.5– to 1-mm-thick, steeply dipping, planar deformation band or fault with strike orthogonal to the higher fault and most of the other structures (Fig. 29). Below this feature, a set of anastomosing deformation bands oriented subparallel to the main set of shallow deformation bands higher in the hole persists for more than 20 cm (Figs. 29 and 30). The shallow anastomosing deformation bands are cut by a few discrete, moderate to steeply dipping, planar deformation bands with normal separations. The base of this sequence is a 2-mm-thick, planar deformation band that is subparallel to the shallow anastomosing set. Below this are relatively few deformation bands forming a widely spaced orthogonal set (Fig. 31).

The two sections having dense arrays of deformation bands are consistent with a simple shear origin. In the upper of these units, reverse shear is constrained by the reverse separation senses exhibited by the main set of shallow deformation bands, together with a Riedel I geometry of the less-dominant set of shallow deformation bands. The anastomosing deformation bands in the lower sheared unit are sub-parallel to the reverse shear plane of the upper sheared unit and are also likely to have a reverse sense of motion. The intervening regions between the sheared units have undergone little deformation. These units are separated from the sheared units by planar deformation bands that must have accommodated significant displacement and acted as mechanical discontinuities.

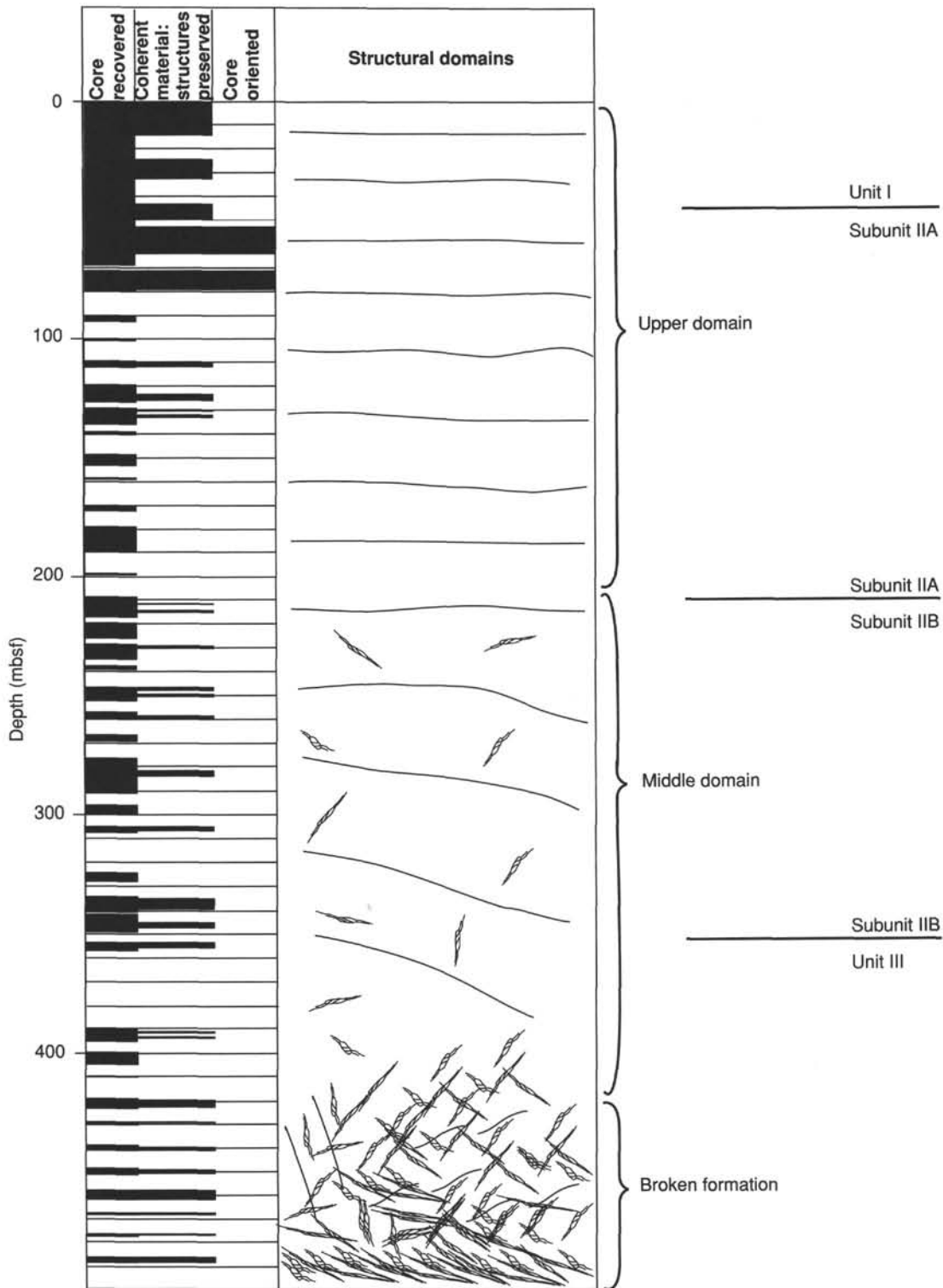


Figure 22. Schematic illustration of major structural features and changes at Site 861, plotted vs. depth. The first three columns show distribution of sediment recovery, the distribution of material sufficiently coherent to make structural observations, and the distribution of material in which structural measurements could be reoriented into a geographical reference frame. Approximate boundaries of lithostratigraphic units are shown for reference.

Table 8. Tabulation of detailed structural data on a section-by-section basis for Holes 861A through 861D.

Core, section, interval (cm)	Depth (msf)	X-ref hand sheets	Photo?	ID	Identifier	Thickness (cm)	Core face orientation		Corrected core ref. frame			Comments
							App dip	Direction	Strike	Dip	Dir.	
141-861A-												
1H-1, 137-141		1		B	Bedding		29	270	185	29	W	
1H-2		NIL										
1H-3, 18-19		2		B	Bedding		3	90	86	38	S	
1H-4, 101-102		3		B	Bedding		0	90	90	6	S	
1H-5, 62-62		4		B	Bedding		9	90	0	9	E	
1H-6		NIL										
1H-7		NIL										
1H-CC		NIL										
141-861B-												
1H-1		NIL										
1H-2		NIL										
1H-3		NIL										
1H-4, 38-40		1		B	Bedding		13	270	113	30	S	
1H-4, 112-112		2		B	Bedding		6	90	27	7	E	
1H-5, 11-13		3		B	Bedding		30	270	220	37	W	
1H-5, 62-64		4		B	Bedding		28	90	323	34	E	
1H-5, 98-100		5		B	Bedding		2	270	258	9	N	
1H-6, 41-42		6		B	Bedding		21	90	12	21	E	
1H-6, 56-57		7		B	Bedding		12	270	125	20	S	
1H-6, 91-92		8		B	Bedding		14	270	209	16	W	
1H-6, 115-116		9		B	Bedding		14	270	145	17	W	
1H-7, 7-8		10		B	Bedding		17	270	164	18	W	
1H		NIL										
141-861C-												
1H-1	0	NIL										
1H-2	1.5	NIL										
1H-CC	2.77	NIL										
2H-1, 95-96	3.95	1		B	Bedding		27	270	199	28	W	
2H-2, 19-20	4.69	2		B	Bedding		2	90	68	5	S	
2H-2, 31-33	4.81	3		B	Bedding		5	90	71	15	S	
2H-2, 70-71	5.2	4		B	Bedding		11	270	138	15	W	
2H-2, 119-120	5.69	5		B	Bedding		1	90	63	2	S	
2H-2, 148-149	5.98	6		B	Bedding		8	90	75	28	S	
2H-3, 57-59	6.57	7		B	Bedding		2	270	108	6	S	
2H-3, 121-122	7.21	8		B	Bedding		2	90	78	9	S	
2H-4, 22-23	7.67	9		B	Bedding		14	90	40	18	E	
2H-4, 31-32	7.71	10		B	Bedding		15	90	28	17	E	
2H-4, 95-96	8.35	11		B	Bedding		2	90	76	8	S	
2H-4, 131-133	8.71	12		B	Bedding		16	270	157	17	W	
2H-5, 63-64	9.53	13		B	Bedding		1	90	277	8	N	
2H-5, 144-145	10.34	14		B	Bedding		3	270	239	6	N	
2H-6, 56-58	10.96	15		B	Bedding		5	90	302	9	N	
2H-7	11.9	NIL										
2H-CC	12.4	NIL										
3H-1	12.5	NIL										
3H-2	13.85	NIL										
3H-3, 99-100	16.34	1		B	Bedding		5	90	69	14	S	
3H-4	16.8	NIL										
3H-5, 44-45	18.54	2		B	Bedding		11	90	10	11	E	
3H-6, 23-24	19.83	3		B	Bedding		15	270	142	19	W	
3H-7	21.1	NIL										
3H-CC	21.7	NIL										
4H-1, 148-150	23.48	1		B	Bedding		12	270	198	13	W	
4H-2, 28-30	24.78	2		B	Bedding		11	90	32	13	E	
4H-2, 53-53	24.03	3		B	Bedding		4	90	56	7	S	
4H-2, 104-104	24.54	4		B	Bedding		2	270	100	11	S	
4H-2, 127-129	24.77	5		B	Bedding		16	270	163	17	W	
4H-3, 2-3	25.02	6		B	Bedding		5	270	180	5	W	
4H-3, 46-47	25.46	7		B	Bedding		6	270	171	6	W	
4H-3, 63-64	25.63	8		B	Bedding		11	270	200	12	W	
4H-3, 78-80	25.78	9		B	Bedding		2	270	135	3	N	
4H-3, 127-129	26.27	10		B	Bedding		4	270	194	4	W	
4H-4, 30-31	26.8	11		B	Bedding		12	90	351	12	E	
4H-4, 32-33	26.82	12		B	Bedding		7	270	215	9	W	
4H-4, 103-104	27.53	13		B	Bedding		3	270	93	41	S	
4H-5, 32-32	28.32	14		B	Bedding		2	270	117	4	S	
4H-5, 95-95	28.95	15		B	Bedding		4	270	110	12	S	
4H-6, 20-22	29.7	16		B	Bedding		2	90	272	44	N	
4H-6, 36-37	29.86	17		B	Bedding		9	270	117	19	S	
4H-6, 46-48	29.96	18		B	Bedding		11	270	190	11	W	
4H-6, 74-75	30.24	19		B	Bedding		4	90	64	9	S	Part of fold?
4H-6, 82-82	30.32	20		B	Bedding		3	90	285	11	N	Part of fold?
4H-6, 83-83	30.33	21		B	Bedding		33	90	163	34	W	Part of fold?
4H-6, 88-90	30.38	22		B	Bedding		16	90	353	16	E	Part of fold?
4H-6, 107-107	30.57	23		B	Bedding		1	90	278	7	N	
4H-7, 2-2	31.02	24		B	Bedding		1	270	252	3	N	
4H-CC, 30-30	31.4	25		B	Bedding		2	270	124	4	S	
5H-1	31.5	NIL										
5H-2	31.5	NIL										
5H-3	33	NIL										

Table 8 (continued).

Core, section, interval (cm)	Depth (mbsf)	X-ref hand sheets	Photo?	ID	Identifier	Thickness (cm)	Core face orientation		Corrected core ref. frame			Comments
							App dip	Direction	Strike	Dip	Dir.	
141-861C-(Cont)												
5H-4	34.5	NIL										
5H-5	36	NIL										
5H-6	37.5	NIL										
5H-7, 9-10	39.09	1		B	Bedding		9	90	326	11	E	
5H-7, 85-86	39.85	2		B	Bedding		10	270	123	18	S	
5H-8, 53-56	41	3		B	Bedding		10	90	67	25	S	
5H-CC	41	NIL										
6H-1	41	NIL										
6H-2, 131-135	43.81	1		B	Bedding		2	90	79	10	S	
6H-3, 18-19	43.18	2		B	Bedding		13	270	197	14	W	
6H-3, 82-86	43.82	3		B	Bedding		50	270	165	5	W	
6H-4, 9-10	44.49	4		B	Bedding		3	90	76	12	S	
6H-5	45.9	NIL										
6H-6, 47-48	47.87	5		B	Bedding		16	270	157	17	W	
6H-7	48.9	NIL										
6H-CC	50.4	NIL										
7H-1	50.5	NIL										
7H-2	51.6	NIL										
7H-3, 29-30	52.99	1		B	Bedding		4	270	244	9	N	
7H-3, 65-66	53.35	2		B	Bedding		11	270	232	18	N	
7H-3, 134-137	54.04	3		B	Bedding		3	270	127	5	S	
7H-4, 81-82	54.51	4		B	Bedding		3	90	297	7	N	
7H-5	55	NIL										
7H-6, 50-51	56.7	5		B	Bedding		5	90	291	14	N	
7H-6, 64-67	56.84	6		B	Bedding		12	90	342	13	E	
7H-6, 85-86	57.05	7		B	Bedding		8	90	32	9	E	
7H-6, 123-125	57.43	8		B	Bedding		7	90	315	10	N	
7H-7, 17-18	57.87	9		B	Bedding		9	90	336	10	E	
7H-7, 63-66	58.33	10		B	Bedding		10	270	197	10	W	
7H-7, 111-112	58.81	11		B	Bedding		2	90	304	4	W	
7H-7, 117-118	58.87	12		B	Bedding		8	90	312	12	N	
7H-7, 139-140	59.09	13		B	Bedding		6	90	304	11	N	
7H-8, 29-30	59.49	14		B	Bedding		5	90	305	9	N	
7H-8, 47-48	59.67	15		B	Bedding		7	90	337	8	E	
7H-CC	59.7	NIL										
8H-1, 15-16	60.15	1		B	Bedding		10	270	154	11	W	
8H-1, 54-55	60.54	2		B	Bedding		4	90	37	5	E	
8H-1, 117-118	61.17	3		B	Bedding		3	90	72	9	S	
8H-2, 58-59	62.08	4		B	Bedding		9	90	38	11	E	
8H-2, 125-126	62.75	5		B	Bedding		7	90	344	7	E	
8H-3, 12-13	63.12	6		B	Bedding		7	90	60	14	S	
8H-3, 41-42	63.41	7		B	Bedding		5	90	50	8	S	
8H-3, 62-63	63.62	8		B	Bedding		5	90	338	5	E	
8H-3, 76-77	63.76	9		B	Bedding		8	270	143	10	W	
8H-3, 97-98	63.97	10		B	Bedding		10	90	26	11	E	
8H-3, 129-130	64.29	11		B	Bedding		6	90	40	8	E	
8H-3, 132-133	64.32	12		B	Bedding		7	90	30	8	E	
8H-4, 61-65	64.91	13		B	Bedding		13	90	21	14	E	
8H-4, 121-122	65.51	14		B	Bedding		3	90	59	6	S	
8H-5, 18-21	65.98	15		B	Bedding		10	90	305	12	N	
8H-6	67.3	NIL										
8H-7	68.8	NIL										
8H-CC	69.3	NIL										
9P-CC	69.5	NIL										
10H-1, 24-24	71.24	1		B	Bedding		1	90	63	2	S	
10H-1, 95-95	71.95	2		B	Bedding		6	90	18	6	E	
10H-1, 101-101	72.01	3		B	Bedding		8	90	32	9	E	
10H-1, 138-138	72.38	4		B	Bedding		16	90	14	16	E	
10H-2, 13-14	72.63	5		B	Bedding		8	90	32	9	E	
10H-2, 40-43	72.95	6		B	Bedding		2	90	82	14	E	
10H-2, 71-71	73.21	7		B	Bedding		4	90	27	4	E	
10H-2, 92-92	73.42	8		B	Bedding		2	90	45	3	E	
10H-2, 112-112	73.62	9		B	Bedding		3	90	63	7	S	
10H-2, 119-119	73.69	10		B	Bedding		6	90	27	7	E	
10H-2, 128-128	73.78	11		B	Bedding		9	90	48	13	S	
10H-3, 6-6	74.06	12		B	Bedding		5	90	50	8	E	
10H-4, 22-22	75.72	13		B	Bedding		13	90	43	17	E	
10H-4, 52-52	76.02	14		B	Bedding		12	90	33	14	E	
10H-4, 74-76	76.24	15		B	Bedding		25	90	21	26	E	
10H-4, 97-97	76.47	16		B	Bedding		4	90	57	6	S	
10H-4, 137-137	76.87	17		B	Bedding		4	90	315	6	E	
10H-5, 50-50	77.5	18		B	Bedding		13	90	343	14	E	
10H-6	78.5	NIL										
10H-CC	80	NIL										
12X-1	90.1	NIL										
12X-2	91.6	NIL										
12X-CC	93.1	NIL										
13X-1	99.8	NIL										
13X-CC	101.2	NIL										
14X-1, 118-120	110.58	1		B	Bedding		15	270	201	16	W	

Table 8 (continued).

Core, section, interval (cm)	Depth (mbsf)	X-ref hand sheets	Photo?	ID	Identifier	Thickness (cm)	Core face orientation		Corrected core ref. frame			Comments
							App dip	Direction	Strike	Dip	Dir.	
141-861C-(Cont)												
14X-2, 15-17	111.05	2		B	Bedding		23	90	14	24	E	
14X-CC	112.4	NIL										
15X-1	119	NIL										
15X-2	120.5	NIL										
15X-3, 82-83	122.82	1		B	Bedding		7	90	23	8	E	
15X-3, 87-89	122.87	2		B	Bedding		2	90	78	9	S	
15X-4, 80-80	124.3	3		B	Bedding							
15X-5	125	NIL										
15X-6	126.5	NIL										
15X-CC	128	NIL										
16X-1, 131-131	130.21	1		B	Bedding		4	90	66	10	S	
16X-2, 136-137	131.76	2		B	Bedding		5	270	219	6	W	
16X-3, 92-93	132.82	3		B	Bedding		4	270	240	8	N	
16X-3, 128-129	133.18	4		B	Bedding		5	270	230	8	N	
16X-4	133.4	NIL										
16X-5, 103-105	135.93	5		B	Bedding		3	90	326	4	E	
16X-CC	136.4	NIL										
17X-1, 104-104	139.74	1		B	Bedding		2	270	258	9	N	
17X-2	140.2	NIL										
17X-CC	141.7	NIL										
18X-1	148.5	NIL										
18X-2	150	NIL										
18X-3	151.5	NIL										
18X-4	153	NIL										
18X-CC	154.5	NIL										
19X-1	158.3	NIL										
19X-CC	159.8	NIL										
21X-1	170.2	NIL										
21X-2	171.7	NIL										
21X-CC	173.2	NIL										
22X-1	179.9	NIL										
22X-2	181.4	NIL										
22X-3	182.9	NIL										
22X-4	184.4	NIL										
22X-5	185.9	NIL										
22X-6	187.4	NIL										
22X-CC	188.9	NIL										
24X-CC	199.2	NIL										
25X-1	208.9	NIL										
25X-2	210.4	NIL										
25X-3	211.9	NIL										
25X-4	213.4	NIL										
25X-5	214.9	NIL										
25X-6	216.4	NIL										
26X-CC	218.6	NIL										
27X-1	220.1	NIL										
27X-2	221.6	NIL										
27X-3, 65-70	223.75	1		B	Bedding		24	270	232	36	N	
27X-4	224.6	NIL										
27X-5	226.1	NIL										
27X-CC	227.6	NIL										
28X-1, 94-98	229.04	1		B	Bedding		19	270	191	19	W	
28X-2	229.6	NIL										
28X-3	231.1	NIL										
28X-4	232.6	NIL										
28X-5	234.1	NIL										
28X-CC	225.6	NIL										
29X-1	237.7	NIL										
29X-CC	239.2	NIL										
30P-CC, 35-36	247.65	1		D	Dark seam	2	37	90	2	37	E	
31X-1	248.3	NIL										
31X-2, 35-38	250.15	1		D	Dark seam		14	90	352	14	E	
31X-2, 35-38	250.15	2		D	Dark seam		40	90	331	44	E	
31X-2, 35-38	250.15	3		B	Bedding		10	90	304	7	N	
31X-2, 56-60	250.36	4		D	Dark seam		8	270	225	11	W	
31X-3	251.3	NIL										
31X-CC	252.8	NIL										
32X-1, 104-105	258.04	1		D	Dark seam		18	90	38	22	S	
32X-1, 108-108	258.08	2		D	Dark seam		2	90	76	8	S	
32X-2, 20-20	258.7	3		D	Dark seam							
32X-CC	260	NIL										
33X-1	266.6	NIL										
33X-2	268.1	NIL										
33X-CC	269.6	NIL										
34X-1	276.2	NIL										
34X-2	277.7	NIL										
34X-3	279.2	NIL										
34X-4	280.7	NIL										
34X-5	282.2	NIL										
34X-6, 17-24	283.87	1		D	Dark seam	0.1						

Table 8 (continued).

Core, section, interval (cm)	Depth (mbsf)	X-ref hand sheets	Photo?	ID	Identifier	Thickness (cm)	Core face orientation		Corrected core ref. frame			Comments
							App dip	Direction	Strike	Dip	Dir.	
141-861C-(Cont)												
34X-CC	285.2	NIL										
35X-1	285.9	NIL										
35X-2	287.4	NIL										
35X-3	288.9	NIL										
35X-4	290.4	NIL										
35X-CC	291.9	NIL										
36X-1, 133-134	296.93	1		B	Bedding	28	90	316	36	E		
36X-1, 44-47	296.04	2		B	Bedding	17	270	187	17	N		
36X-2	297.1	NIL										
36X-3, 63-72	299.23	3		B	Bedding	4	90	286	15	N		
36X-4	300.1	NIL										
36X-CC	301.6	NIL										
37X-1	304.9	NIL										
37X-2, 50-50	306.9	1		B	Bedding	8	270	194	8	W		
37X-2, 90-90	307.3	2		B	Bedding	4	90	333	4	E		
37X-2, 111-114	307.51	3		B	Bedding	2	270	252	6	N		
37X-CC	307.9	NIL										
38X-CC	314.5	NIL										
39X-1	324.2	NIL										
39X-2	325.7	NIL										
39X-3	327.2	NIL										
39X-4	328.7	NIL										
39X-CC	330.2	NIL										
40X-1	333.9	NIL										
40X-2, 88-90	336.28	1		B	Bedding	38	90	347	39	E		
40X-3	336.9	NIL										
40X-4, 31-35	338.71	2		B	Bedding	12	270	198	13	W		
40X-5	339.9	NIL										
40X-6, 25-30	341.65	3		B	Bedding	24	270	170	26	W		
40X-CC	342.9	NIL										
41X-1	343.4	NIL										
41X-2	344.9	NIL										
41X-3, 44-46	346.84	1		B	Bedding	3	270	243	7	N		
41X-3, 60-70	347	2		D	Dark seam	11	90	324	13	E		
41X-3, 60-70	347	2		D	Dark seam	7	90	65	16	S		
41X-3, 90-95	347.3	3		D	Dark seam	38	90	15	39	E		
41X-4	347.9	NIL										
41X-CC	349.4	NIL										
141-861D-												
1R-1, 123-125	343.53	1		B	Bedding	16	90	49	23	S		
1R-2, 22-29	344.02	2		B	Bedding	25	90	332	28	E	Pyrite	
1R-3, 132-135	346.62	3		D	Dark seam	12	270	96	64	S		
1R-4, 18-20	346.98	4		B	Bedding	3	90	72	9	S		
1R-CC	348.3	NIL										
2R-1, 88-89	352.78	1		B	Bedding	5	90	310	8	N		
2R-1, 102-103	352.92	2		B	Bedding	12	90	45	17	E		
2R-1, 109-110	352.99	3		B	Bedding	29	270	175	29	W		
2R-2, 9-16	353.49	4		B	Bedding	49	270	174	49	W		
2R-2, 86-88	354.26	5		B	Bedding	24	270	165	25	W		
2R-3	354.9	NIL										
2R-CC	356.4	NIL										
6R-1	390.4	NIL										
6R-2, 26-30	393.16			D	Dark seam	22	90	159	23	W	First	
6R-2, 26-30	393.16			D	Dark seam	34	90	347	35	E	Second	
6R-3	393.4	NIL										
6R-4	394.9	NIL										
6R-CC	396.4	NIL										
7R-1	400.1	NIL										
7R-2, 89-90	402.49	1		D	Dark seam	6	90	53	10	S		
7R-3	403.1	NIL										
7R-CC	404.6	NIL										
8R-1	409.8	NIL										
8R-CC	411.3	NIL										
9R-1, 46-47	419.86	1		D	Dark seam	4	90	4	24	E		
9R-1, 46-47	419.86	1		D	Dark seam	66	90	66	26	S		
9R-1, 93-96	420.33	2		D	Dark seam	70	90	342	71	E		
9R-1, 104-105	420.44	3		D	Dark seam	27	270	142	33	W		
9R-1, 104-105	420.44	3		D	Dark seam	46	270	150	50	W		
9R-1, 104-105	420.44	3		D	Dark seam	19	270	124	32	S		
9R-2, 12-13	421.02	4		D	Dark seam	28	270	224	36	W		
9R-2, 12-13	421.02	4		D	Dark seam	32	270	203	34	W		
9R-2, 12-13	421.02	4		D	Dark seam	24	270	211	27	W		
9R-3, 67-69	423.07	5		D	Dark seam	16	90	296	34	N		
9R-CC, 8-8	423.9	6		D	Dark seam						With angular breccia	
10R-1, 47-51	429.57	1		D	Dark seam	1	270	95	12	S	Pyrite	
10R-1, 47-51	429.57	2		D	Dark seam	2	270	104	8	S		
10R-1, 47-51	429.57	3		B	Bedding	3	270	96	25	S		
10R-CC	430.6	NIL										
11R-1	438.8	NIL										

Table 8 (continued).

Core, section, interval (cm)	Depth (mbsf)	X-ref hand sheets	Photo?	ID	Identifier	Thickness (cm)	Core face orientation		Corrected core ref. frame			Comments
							App dip	Direction	Strike	Dip	Dir.	
141-861D-(Cont)												
11R-2, 114-121	441.44	1		D	Dark seam		12	270	240	23	N	Dark seam zone
11R-CC	441.8	NIL										
12R-1, 71-71	449.21	1		D	Dark seam		30	270	218	36	W	
12R-1, 90-93	449.4	2		B	Bedding		26	270	217	31	W	
12R-2	450	NIL										
12R-3	451.5	NIL										
12R-CC	453	NIL										
13R-1, 101-106	459.11	1		D	Dark seam		23	270	151	26	W	
13R-2, 14-16	459.74	2		B	Bedding		9	90	58	16	S	
13R-2, 32-33	459.92	3		D	Dark seam		2	90	81	12	S	First
13R-2, 32-33	459.92	4		D	Dark seam		32	90	61	52	S	Second
13R-2, 52-54	460.12	5		D	Dark seam		3	270	250	9	N	
13R-3, 80-80	461.9	6		B	Bedding		2	90	277	16	S	
13R-3, 115-116	462.25	7		B	Bedding		6	270	114	14	S	
13R-CC	462.6	NIL										
14R-1, 53-63	468.23	1		D	Dark seam		4	270	231	6	N	First, second, and third seams
14R-1, 71-78	468.41	2		D	Dark seam							
14R-1, 93-98	468.63	3		D	Dark seam		81	270	199	81	W	First
14R-1, 93-98	468.63	3		D	Dark seam		16	90	350	16	E	Second
14R-CC	469.2	NIL										
15R-1, 26-33	476.56	1		D	Dark seam		40	90	15	41	E	First
15R-1, 26-33	476.56	1		D	Dark seam		74	90	353	74	E	Second
15R-2, 58-63	478.38	2		B	Bedding		83	90	2	83	E	Fold
15R-2, 72-270	478.52	3		D	Dark seam		72	270	186	72	W	
15R-CC	479.3	NIL										
16R-1, 40-43	486.4	1		D	Dark seam		5	270	141	6	W	
16R-1, 50-50	486.5	2		B	Bedding		16	90	283	52	N	
16R-1, 51-52	486.51	3		D	Dark seam		40	90	308	54	N	
16R-1, 102-110	487.02	4		D	Dark seam		43	90	64	65	S	Second
16R-1, 102-110	487.02	4		D	Dark seam		5	90	338	5	E	First
16R-2, 20-26	487.75	5		D	Dark seam		43	270	189	43	W	First
16R-2, 20-26	487.75	5		D	Dark seam		9	270	249	23	N	Second, reverse fault
16R-2, 27-31	487.77	6		D	Dark seam		35	90	298	56	N	Domain boundary, not seen
16R-2, 40-46	487.9	7		D	Dark seam		81	270	228	84	N	First
16R-2, 40-46	487.9	7		D	Dark seam		33	270	230	45	N	Second, reverse fault
16R-2, 40-46	487.9	7		D	Dark seam		1	270	268	32	N	Domain boundary
16R-2, 40-46	487.9	7		D	Dark seam		10	90	42	13	E	
16R-2, 40-46	487.9	7		D	Dark seam		15	270	244	32	N	
16R-2, 40-46	487.9	7		B	Bedding		68	270	181	68	W	Not overturned
16R-2, 45-50	487.95	8		D	Dark seam		10	90	48	15	S	First
16R-2, 45-50	487.95	8		D	Dark seam		29	90	75	65	S	Second, reverse fault
16R-2, 45-50	487.95	8		D	Dark seam		41	270	135	51	W	Third, normal fault
16R-2, 45-50	487.95	8		D	Dark seam		70	270				Third, high angle reverse fault
16R-3, 7-16	489.07	9		D	Dark seam		30	90	65	54	S	First
16R-3, 7-16	489.07	9		D	Dark seam		76	90	333	77	E	Second, normal fault
16R-3, 18-23	489.18	10		D	Dark seam		25	90	2	25	E	Domain boundary, cut by n.f.
16R-3, 22-36	489.22	11		D	Dark seam		28	90	51	40	S	
16R-3, 22-36	489.22	11		D	Dark seam		88	270	198	88	W	
16R-3, 22-36	489.22	11		B	Bedding		14	90	274	74	N	
16R-CC	490.5	NIL										

The deformation bands developed in Sections 141-861D-16R-2, 20 cm, through -16R-3, 40 cm, described above, show remarkable lithologic control upon their development. These deformation bands are developed in claystones but become less important in coarser sediments. Figure 28 shows deformation bands dying out in coarser sediment in the upper sheared unit. Figure 29 shows the shallow anastomosing set of deformation bands becoming significantly less developed in a 1-cm-thick subvertical sand body. Higher up in Core 141-861D-16R, sands predominate and no deformation bands are observed. It seems likely that coarser sandy units have accommodated deformation by bulk shape change, probably by a particulate flow mechanism (Borradaile, 1981), whereas finer lithologies accommodate deformation by a variety of mechanisms in discrete deformation bands. Microstructural observations of specimens from Sections 141-861D-16R-2, 20 cm, through -16R-3, 40 cm, are required to further constrain these hypotheses.

ORGANIC GEOCHEMISTRY

Shipboard organic geochemical analyses of sediments from Holes 861A, 861B, 861C, and 861D included inorganic carbon,

total organic matter, volatile hydrocarbon and nonhydrocarbon gases, organic matter fluorescence estimation, total hexane soluble lipid/bitumen analysis, and Rock-Eval analysis. The instrumentation, operating conditions, and procedures are summarized in the Explanatory Notes chapter (this volume).

Volatile Gases from Sediments

Volatile gases (hydrocarbons, CO₂, H₂S, N₂, CS₂, O₂) released by the sediments recovered at Holes 861A through 861D were continuously measured by gas chromatography as part of the shipboard safety and pollution monitoring program. We used the headspace technique, in which a sediment plug is heated in a sealed vial to drive off gases (Emeis and Kvenvolden, 1986). The results are listed in Table 9 and Figure 32. The methane concentrations in the headspace volumes range between 8 and 119143 ppm (v/v). In the uppermost part of the sequence methane increased steeply from 8 ppm at 1.5 mbsf to over 10000 ppm at 16.9 mbsf. Beyond this depth methane content in recovered sediments remains high and the measured levels are most probably controlled by lithology, porosity, and degassing during core retrieval. Ethane and higher hydrocarbons up to C₇ (heptane) were also

detected at several intervals that are more clearly identifiable from the composition of gases retrieved from core-expansion voids (see below). The downhole profiles for headspace methane, ethane and propane plus heavier hydrocarbons are also shown in Figure 32. Ethane content increases significantly as indicated by the decrease in the C_1/C_2 ratio at about 200 mbsf from a ratio range of 1200/5000 to a range of 160/400 (Fig. 33). From about 450 mbsf to total depth a small increase in the C_1/C_2 ratio was observed. The overall gas content of these sediments as determined by headspace analysis was found to range up to 0.794 cm³ of methane per cubic centimeter of sediment, with the predominant gas being methane.

Thus, by headspace gas analysis, two general zones with different gas characteristics were observed: an upper zone (1.5 to about 200 mbsf) where the gases consist predominantly of methane with small amounts of ethane and a general composition consistent with a biogenic origin; and a lower zone where, in addition to methane and ethane, small amounts of heavier hydrocarbons (C_3+) were observed, that suggest a contribution of thermogenic hydrocarbons.

Methanogenic bacteria are generally active after complete sulfate depletion by sulfate-reducing bacteria (Claypool and Kaplan, 1974). The sulfate content in interstitial waters throughout Hole 861B is relatively low, with almost complete sulfate depletion observed below 7.45 mbsf (see Inorganic Geochemistry section, this chapter). Therefore, environmental conditions for methanogenesis via CO_2 reduction, the major process by which microbial methane is produced in deep-sea sediments, were probably favorable for biogenic methane generation in the sedimentary column.

Organic matter maturation in the lower zone indicates that local thermal maturity would be too low to generate the observed thermogenic hydrocarbons. These are most likely of migrational origin from deeper sources in the accretionary prism (see below).

Carbon dioxide was present at concentrations up to 4385 ppm in gases desorbed from the sediments by the headspace method (Table 9), with somewhat lower CO_2 levels found in the deeper section of Site 861. Even higher amounts of free CO_2 could have been present in the sediments and pore waters prior to the depressurization that occurs during core retrieval. Large fluctuations in CO_2 concentration were observed throughout the sequence of recovered sediments, suggesting possible alterations due to drilling fluid contamination (seawater), degassing during depressurization and core sectioning, and air contamination at sample introduction in headspace containers. No H_2S was detected in Site 861 gases.

Fluorescence

The bitumen extract colors (n-hexane/methanol-soluble organic matter) progressed from intense yellow to pale yellow and finally to nearly colorless with increasing depth in the hole. The concentrations of extractable organic matter are low, based on the color and fluorescence intensities of the extracts as well as the relative intensities of chromatograms of extractable organic matter (see below). The fluorescence of the extracts went from orange-red to yellow-orange in the upper 75.4 mbsf, turning to yellow and pale yellow in the 110.7- to 282.7-mbsf interval, finally reaching a white to blue-white fluorescence in the 285.6- to 487.4-mbsf interval. Yellow fluorescence is interpreted to indicate incipient thermal maturation of bitumen to the early mature stage, and white (or blue-white) fluorescence has been associated with mature and overmature bitumen, enriched in polynuclear aromatic hydrocarbons (PAH) (Shipboard Scientific Party, 1982).

Gas in Core Expansion Voids

After core retrieval on deck, gas expansion voids were observed in the coreliner-contained core. The gas was sampled

directly from the gas voids by piercing the core liner with a sampling needle and collecting the gases in pre-evacuated vacuum containers. Upon chromatographic analysis the expansion void gases (EVG) were found to contain hydrocarbons in the C_1 to C_7 range and a composition somewhat different from the gases isolated by headspace analysis (Table 10 and Fig. 34).

EVG hydrocarbon contents (up to 974313 ppm; 97.4% vol.) were found to reach significantly higher concentration levels than headspace gas and presented different C_1/C_2 gas ratios for equivalent depths (Fig. 35). Due to higher gas concentrations EVG gas allows a better detection of heavier hydrocarbons (C_3+), but headspace analysis gives lower C_1/C_2 ratios. Thus, for Site 861, gas analyses gave C_1/C_2 ratios from 131,625 to 550 for the EVG gas, whereas C_1/C_2 levels of only 5027 to 156 were obtained for the same interval by the headspace analyses. This difference is most likely due to different gas fugacities and degassing processes occurring during core retrieval, and the inevitable air exposure of headspace samples that causes a preferential loss of methane and results in a decrease of the C_1/C_2 ratio in the headspace gases. Simultaneously, the gas released in the core is enriched in methane and will give consistently higher C_1/C_2 ratios. As indicated in reports for Sites 859 and 860 these differences are important, because the drilling safety criteria based on C_1/C_2 or C_1/C_3 ratios, as analyzed on board, are method-dependent. Different safety limits should therefore be considered for data based on headspace and core-liner gas analysis.

Distinct gas zones can be observed. A shallow upper layer down to about 25.6 mbsf contains a predominantly biogenic gas composed of methane with no ethane, and trace concentrations of C_3 to C_6 (4 to 58 ppm). Below 34.5 mbsf ethane was detected; it increases with depth to a relative maximum of 1593 ppm at 258.7 mbsf (Table 10). The C_1/C_2 ratio (Fig. 33) decreases to a relative minimum of 550 at 258.7 mbsf, below which it increases again with depth. Different intervals (about 21.2 to 61.1 mbsf; a single sample at 149.9 mbsf; and 215.2 to 488.2 mbsf) have small but significant amounts of C_3 -plus compounds (up to 91 ppm v/v), with the heavier hydrocarbons extending up to C_7 (heptane), well within the natural gasoline range. The origin of these compounds is currently unknown but is most likely associated with a deeper thermogenic source. In both headspace and expansion-void gas analysis the carbon range cutoff is at C_7 , and is determined by the chromatographic conditions and the volatility of the heavier hydrocarbons during sampling and handling.

The presence of heavier hydrocarbons was confirmed by organic extraction analysis (see below). At Site 861 the pressure coring system (PCS) was deployed and recovered pressurized gases at subhydrostatic pressure on two occasions (Cores 141-861C-26P and 141-861C-30P). The gases were analyzed (Table 10) and found to be of similar composition as expansion-void gases from equivalent core intervals (Table 10 and Fig. 35). For description of PCS deployments see Inorganic Geochemistry section, this chapter.

Bitumen Analyses and Organic Matter Characterization

The hexane extracts (500 mL) of the samples from the fluorescence assessment were concentrated under a stream of helium to about 25–400 μ L. These concentrates were analyzed by high-resolution gas chromatography, and examples of traces are shown in Figure 36. The dominant compound series in the total extracts are hydrocarbons ranging from n- C_{15} to n- C_{36} with some samples where pristane ($C_{19}H_{40}$) and phytane are the major isoprenoid alkanes identifiable on board. As a general trend the n-alkanes $>C_{26}$ have a significant predominance of homologues with odd carbon numbers and carbon preference indexes (CPI) > 1.0 (Table 11), typical for immature hydrocarbons that originate from terres-

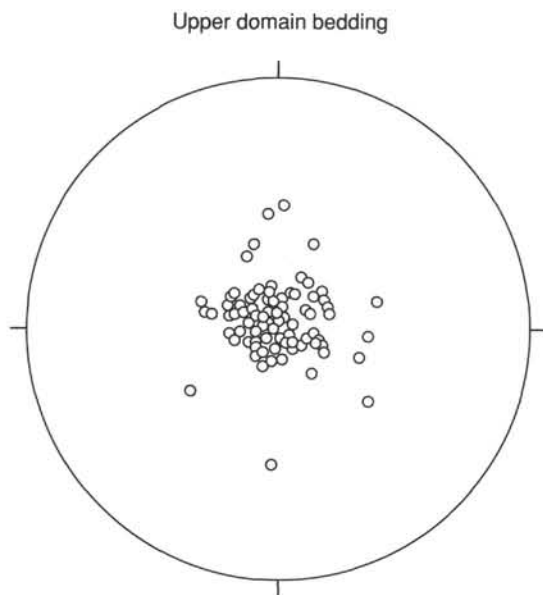


Figure 23. Stereographic projection of poles to bedding in the core reference frame for the upper domain at Site 861.

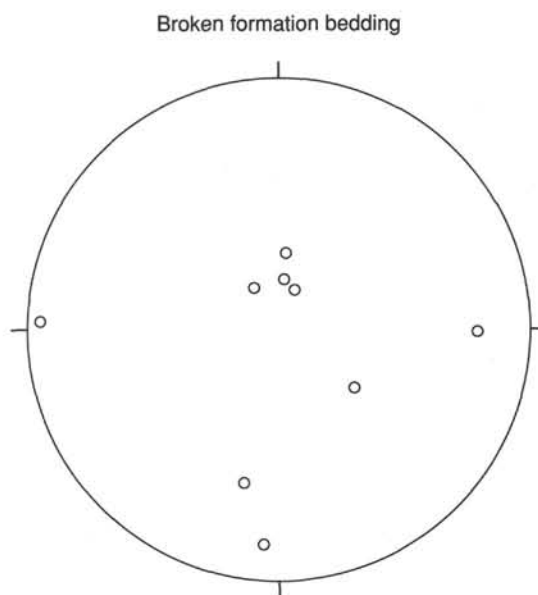


Figure 25. Stereographic projection of poles to bedding in the core reference frame for the broken formation at Site 861.

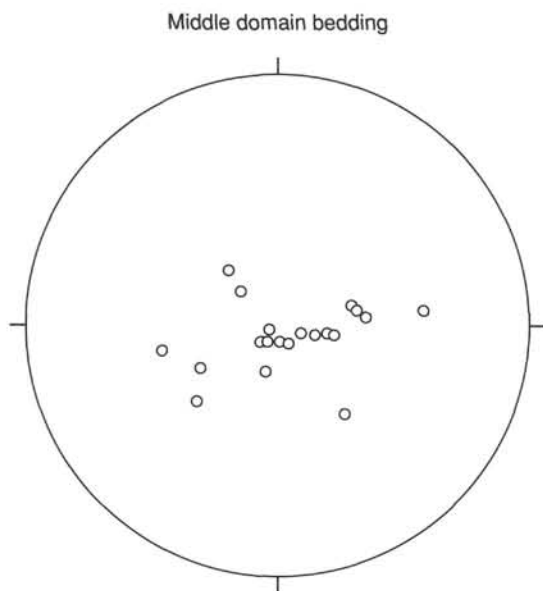


Figure 24. Stereographic projection of poles to bedding in the core reference frame for the middle domain at Site 861.

trial higher plants (Simoneit, 1977, 1978). The contribution of bitumen of marine origin, derived from alteration of microbial lipids of marine origin (<C₂₄; maxima about C₂₀), is more significant in the upper section of Site 861 (1.5 to 110.7 mbsf), whereas the organic matter from the lower section (133.2 to 487.4 mbsf) has a predominantly terrigenous origin.

The value of the carbon preference index decreases with geothermal maturation approaching values of CPI ≈ 1 for crude oils and mature organic matter. The CPI had to be calculated for the

range C₂₆–C₃₅ because in some samples *n*-C₂₅ co-elutes with a contaminant that is more abundant in samples taken from split cores, and is therefore most likely associated with plastic-derived contaminants originating from core-liner fragments incorporated during core splitting.

For Site 861 the organic matter extracted from the sediments has an overall CPI trend that shows a low degree of geothermal maturity with higher CPI values in the upper part of the drilled section and a moderate CPI decrease with depth consistent with a gradual increase in maturation (Table 11). Superimposed on this general low-maturational background some significant anomalies were observed at 214.7, 326.2, and 450 mbsf, which show the presence of significantly more mature hydrocarbons (with CPI around 1) emplaced in sediments of a lower degree of maturation (CPI > 2), as for Samples 141-861C-25X-4 (CPI = 1.01), 141-861C-39X-2 (CPI = 0.87), and 141-861D-12R-1 (CPI = 1.06) (Table 11 and Fig. 36).

No significant trend was observed in the isoprenoid to normal hydrocarbon ratios (Pr/*n*-C₁₇ and Ph/*n*-C₁₈), and the pristane to phytane ratios (Pr/Ph) show no evident depth-related variations (Table 11). Whereas pristane to phytane ratios are highly formation dependent (Farrington et al., 1988), they have been reported to be an indicator responding to maturation (Simoneit et al., 1981), as well as an indicator of anoxic conditions of sedimentation (Didyk et al., 1978).

Analysis of gases released in the core liner, as well as gases released from sediments by headspace analysis, indicated the presence of hydrocarbons up to C₇, which is the upper limit of detection under the chromatographic conditions and calibration of the natural gas analyzer, and suggested the possible presence of higher gasoline-range hydrocarbons. The presence of C₇+ gasoline-range hydrocarbons was also corroborated by the extraction analyses, which show that hydrocarbons up to C₁₂, well in the carbon atom range for natural gasoline, can be observed on the tailing side of the solvent elution peak when contrasted with the solvent extraction blank. The relative amount of gasoline-range hydrocarbons increases with depth and is indicative of an

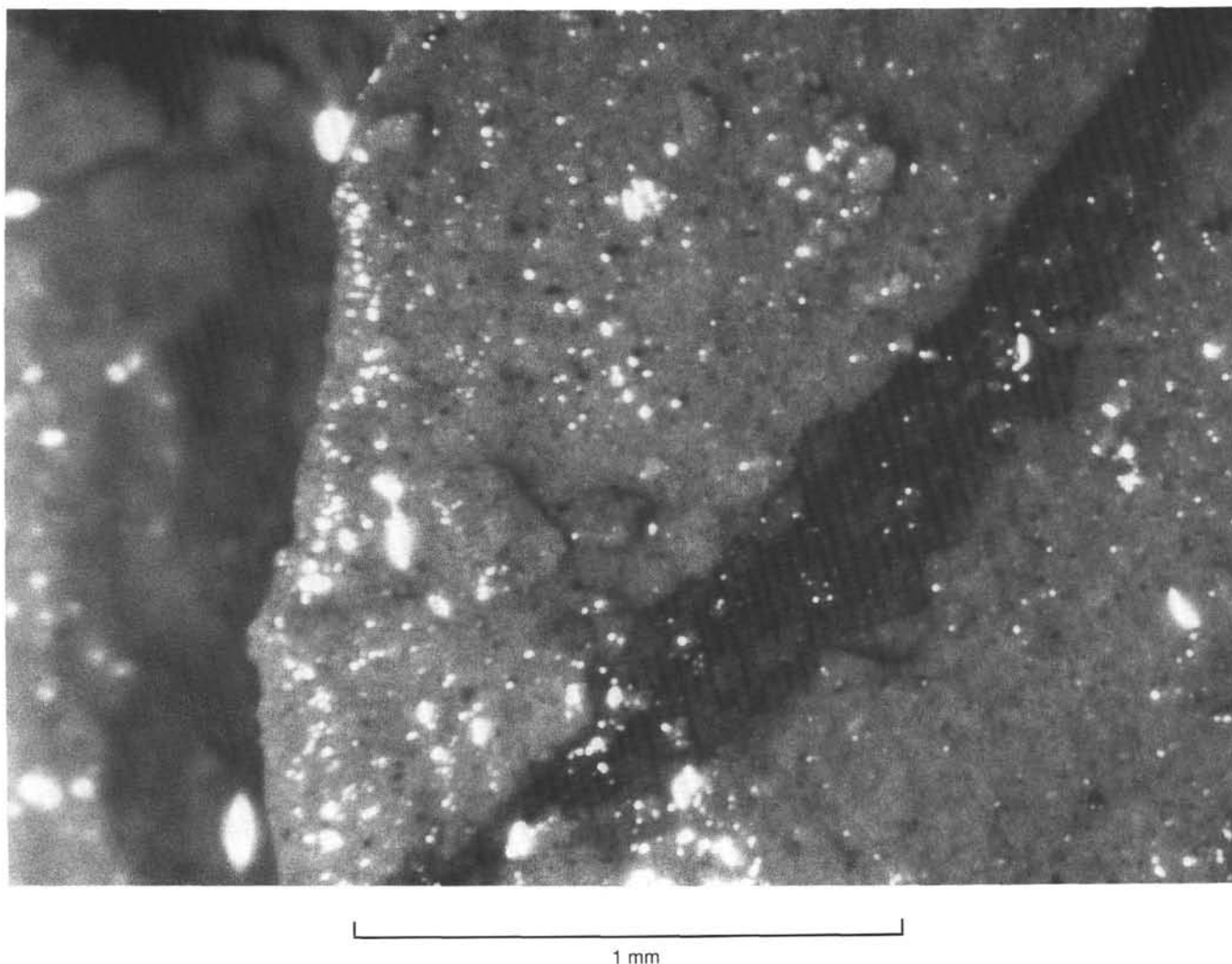


Figure 26. Photomicrograph (binocular microscope) of a thin deformation band that is surrounded by a 0.3-mm-thick zone of breccia (141-861C-32X-1, 105–106 cm).

increased thermal stress and/or the existence of a more deeply located source of thermogenic hydrocarbons.

This deeper source of thermogenic hydrocarbons may be a conventional slowly-matured hydrocarbon source located deeper in the sedimentary sequence. Alternatively, the thermogenic hydrocarbons could be generated by a high-temperature energy source (Simoneit et al., 1981) and/or by petroleum hydrocarbon generation by action of hydrothermal fluids upon immature sedimentary organic matter (Didyk and Simoneit, 1989).

Organic Content and Type of Organic Matter

Because the NCS analyzer was inoperable during Site 861 analysis, the total organic carbon content (TOC) of the sediments was measured by means of the Rock-Eval pyrolysis technique (Epistalié et al., 1977). TOC was found to be relatively low except in the uppermost sediments (0 to 1 mbsf) that have higher values (1.39%). Otherwise TOC values of most samples range from 0.15% to 0.5% and show no trend related to depth (Table 12 and Fig. 37). The decrease of TOC within the uppermost sediments suggests decomposition of organic matter by microbial metabolism occurs in the near-surface sediments.

Rock-Eval pyrolysis of the organic matter indicated the presence of an immature kerogen with T_{max} ranging from 376° to 414°C (for samples with $S_2 > 0.5$ mg HC/g sediment), which can be tentatively associated with vitrinite reflectance levels of not higher than about 0.5%. Pyrolyzable organic matter content (S_2) is also low, and T_{max} values for samples with S_2 contents of less than 0.5 mg hydrocarbons/per gram of sediment are often inaccurate and were rejected.

The kerogen for Site 861 is relatively homogeneous and shows no trends related to depth, and has low hydrogen indexes ($HI < 200$ mg HC/g TOC) together with high oxygen indexes ($OI > 100$ mg CO_2 /g TOC) characteristic of Type III, gas-prone kerogen of terrigenous origin (Fig. 38). However, for clay rich sediments containing less than 0.5% of TOC, the measured HI is likely to be too low due to adsorption of pyrolytic organic compounds onto the mineral matrix, which suggests that the actual HI values can be higher but still well within the Type III, gas-prone kerogen zone (Fig. 38). Significantly, the high levels of OI are suggestive of oxidative alteration of the organic matter during sedimentation and early diagenesis and/or long-range transport processes that contributed to the oxidation of the organic matter.

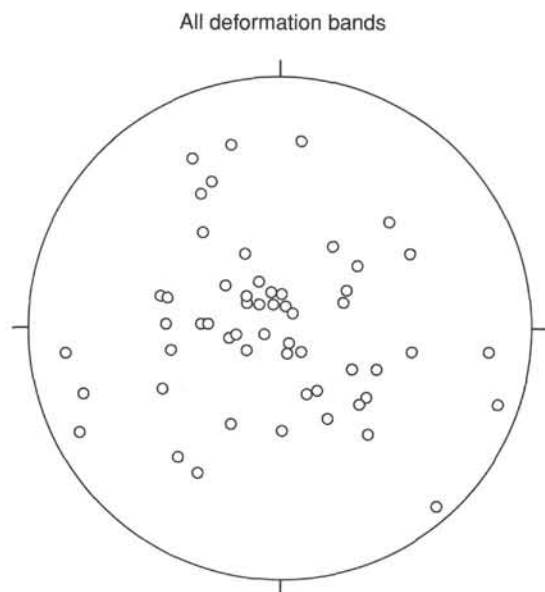


Figure 27. Stereographic projection of poles to deformation bands at Site 861 in the core reference frame, showing that their orientations lack a pattern.

Conclusions

Biogenic gas composed mainly of methane and ethane was detected in the upper zone of the sedimentary section of Site 860 (down to around 200 mbsf). Thermogenic hydrocarbons extending into the gasoline range are present in the lower section (around 200 mbsf to total penetration depth). The organic matter of the sediments corresponds to a Type III, gas prone, kerogen with a low degree of maturation. Localized maturational and organic anomalies suggest the occurrence of migrational processes and a deeper source of thermogenic hydrocarbons.

INORGANIC GEOCHEMISTRY

The primary purposes of the pore-water program at Site 861 were (1) to determine if methane hydrates are present above a prominent BSR at ~200 mbsf, (2) to evaluate whether pore-fluid compositions provide information about vertical diffusional gradients above continental basement or potential fluid sources and migration pathways during deformation, and (3) to contrast diagenesis in a more benign thermal regime with that at hydrothermally active Sites 859 and 863. Fluids were obtained from squeezing whole rounds of APC, XCB, and PCS cores, and from the water sampler temperature probe (WSTP), all of which were analyzed for sodium, calcium, magnesium, potassium, strontium, ammonia, salinity, chloride, sulfate, pH, alkalinity, boron, silica, lithium, and fluoride. The whole-round squeezed interstitial water data are presented in Table 13 and Figure 39.

The WSTP was deployed four times in the water-plus-temperature configuration. On our first attempt we failed to collect fluids due to malfunction of a valve. In the subsequent three deployments we collected samples in both the titanium coil and the overflow chamber. The results of the sample analyses are presented in Table 14 and Figure 40. WSTP results from 31.5 mbsf are consistent with those obtained by squeezing. The following two deployments, however, show deviations in the composition of the in-situ samples from fluids obtained by squeezing, suggesting contamination of the samples with drilling fluid. In all cases, the amount of sample recovered in the titanium coil was less than 6 mL, suggesting a gas phase separation inside the coils during

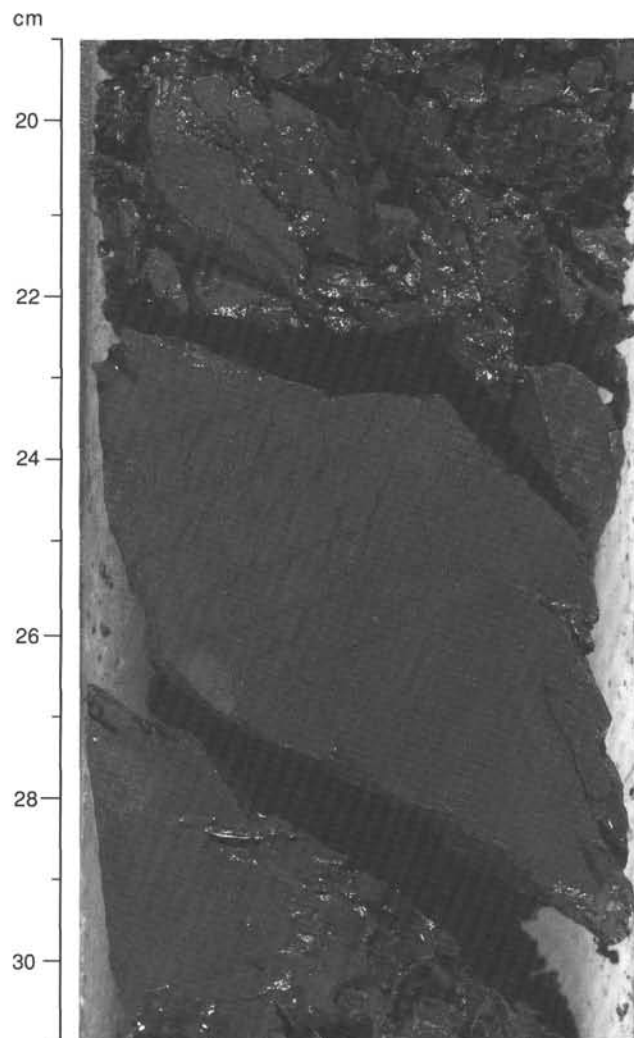


Figure 28. Core photograph, steep set of anastomosing deformation bands cut by shallow set of planar deformation bands with reverse separations (Section 141-861D-16R, 19-31 cm). Deformation bands die out in coarser material to the right of the picture.

recovery. The fluids were collected with a syringe and the headspace analyzed. The gas compositions are given in Table 15. The C_1/C_2 ratios in the titanium "headspace" correspond to those measured in Vacutainer samples (Fig. 41).

The pressure core sampler (PCS) was run four times in Hole 861C. In Core 141-861C-9P (PCS #9: 69.5–71.0 mbsf) it actuated but failed to retain pressure due to ball-valve link-pin failure. Comparison of the PCS gas compositions with vacutainer data are contained in the Organic Geochemistry section, this chapter (see Table 10 and Fig. 35). Recovery was about 23 cm, all of which had clearly been shoved to the top of the core barrel and washed out from the bottom. The PCS did not actuate in Core 141-861C-20P (PCS #10: 168.2–169.7 mbsf) and thus retained no pressure and recovered no core. In Core 141-861C-26P (PCS #11: 218.6–220.1 mbsf) the PCS actuated successfully but for unknown reasons retained only 1050 kPa on deck. This PCS core barrel was transferred to the water bath, equilibrated at 12°C, and the trapped pressure expanded into a gas cylinder. During expansion of the gas pressure through a water trap into the gas manifold, a 4.8-mL fluid sample was recovered from the headspace above the core

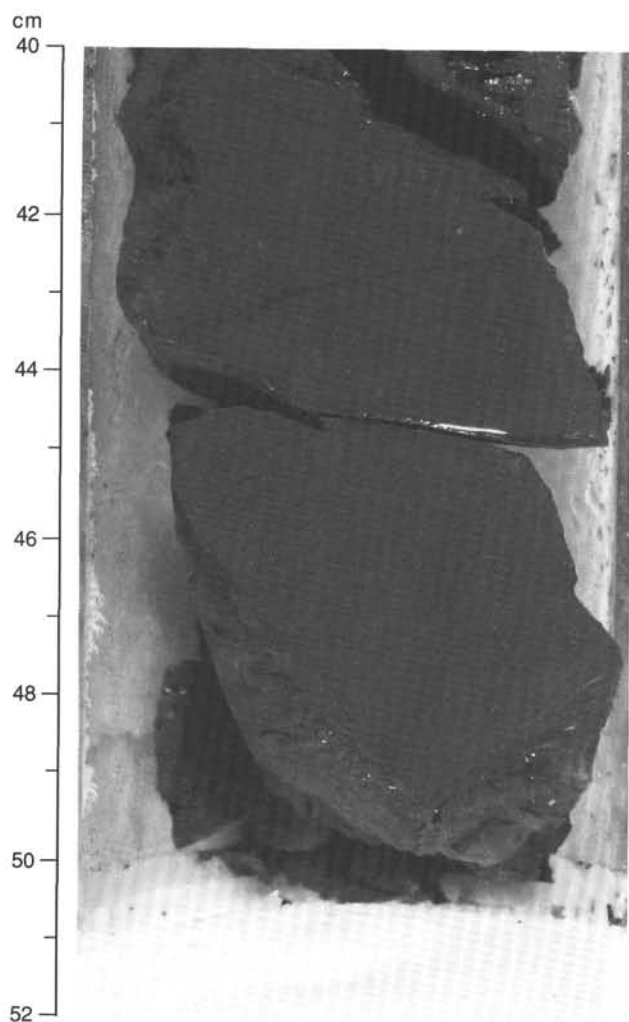


Figure 29. Core photograph, thick planar deformation band or fault separating an interval of few deformation bands from an interval of closely spaced anastomosing bands (Section 141-861D-16R-2, 40–52 cm). Deformation bands are much less developed in subvertical sand at the right of picture.

(see Table 14: Sample 141-861C-26P-PCS.PO). Chemical analyses of this sample suggest that it is composed of a mixture of formation waters and drilling fluids. One meter of core was recovered, and the interval from 40–60 cm was submitted to routine shipboard squeezing to recover pore fluids (Table 13 and Fig. 39). It is clear that the PCS pore-fluid sample provides an interstitial composition that is consistent with the other squeezed whole rounds. Core 141-861C-30P (PCS #12: 247.3–248.3 mbsf) actuated but retained only 1300 kPa pressure on deck, again for unknown reasons. It was equilibrated in the water bath at 12°C and the trapped pressure expanded into a gas cylinder. The remaining gas in these cylinders was retained for isotopic analyses. No fluids were recovered from the water trap after these transfers, suggesting that this PCS run had trapped a gas headspace pressure in situ. Core recovery was a full barrel (100 cm), but the sediment was very stiff and the core material was too disturbed after extrusion to warrant further work.

Re-evaluation of thermal gradients at Site 861 from downhole WSTP and ADARA temperature measurements suggest that methane hydrates are stable down to about 270 mbsf (see tem-

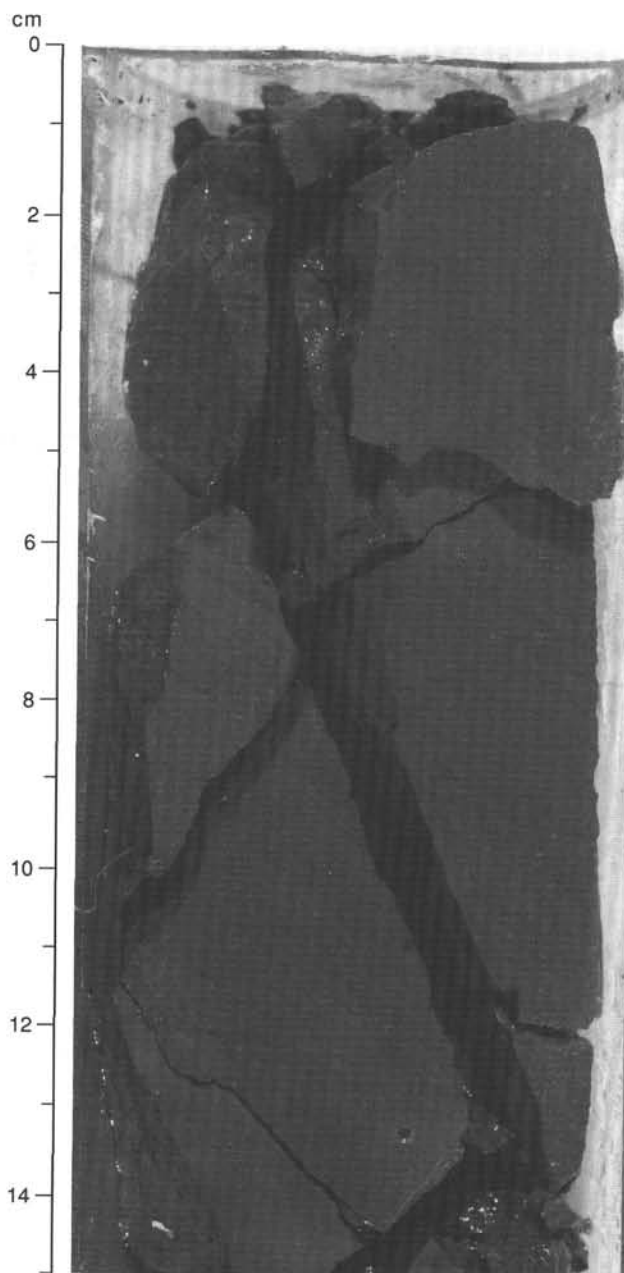


Figure 30. Core photograph, closely spaced shallowly dipping anastomosing deformation bands that persist for more than 20 cm below the deformation band or fault shown in Figure 29 (Section 141-861D-16R-3, 0–15 cm).

perature discussion in WSTP-ADARA Temperature Measurements section, this chapter). This is deeper than the depth of the BSR in this area (~200 mbsf). As there are no chemical indications for the presence of hydrates at Site 861 (see below), we conclude that there are no hydrates at this site and that the BSR is associated with a different phenomenon. No hydrates were recovered, logging was not attempted, and gas expansion of cores was minor.

The interstitial water chemistry profiles at Site 861 (Fig. 39) are indicative of a number of complex processes. Sulfate is depleted below the topmost interval, indicating the presence of methanogenesis below about 10 mbsf, consistent with the presence of methane throughout the section (see Organic Geochemis-

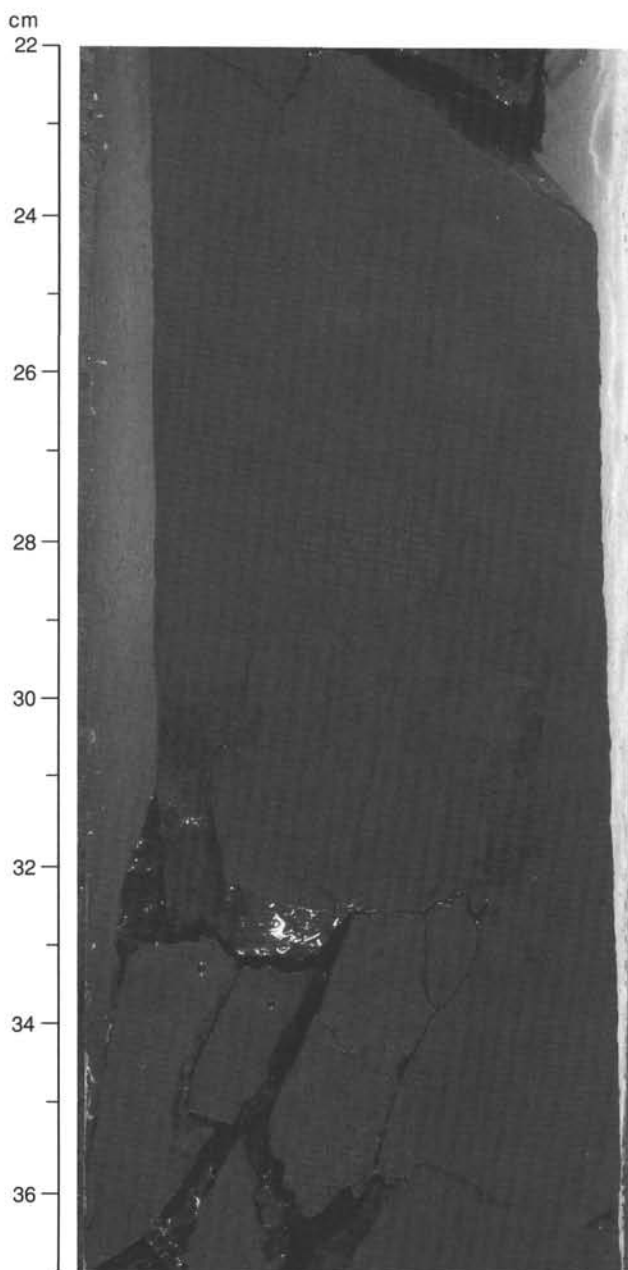


Figure 31. Core photograph, orthogonal set consisting of a few widely spaced deformation bands (Section 141-861D-16R-3, 22–37 cm).

try section, this chapter). Sulfate concentrations remain at less than 1 mM until ~200 mbsf, below which sporadic occurrences of sulfate (<4 mM) indicate either slight contamination of the squeezed samples with drill fluid or deep penetration of seawater into the deformed strata (210–390 mbsf) and broken formation (390–496 mbsf) (see Structural Geology section, this chapter).

Sodium and chloride concentrations increase downhole from bottom-water values to levels about 10%–15% above bottom water. There is no evidence for the existence of hydrates (no low-salinity hydrate-dissociation zones). The downward-increasing salt gradient at Site 861 contrasts with that at Sites 859 and 860. At Site 859, high salinities were encountered throughout the section (except in the hydrate decomposition layer in the upper

100 m) and were attributed to diffusional spreading of salt down-section from long-term steady-state hydrate formation in the uppermost section. At Site 860, salinities lower than seawater throughout the drilled section could be interpreted as the mirror image process (i.e., decomposition of a preexisting hydrate layer might have “freshened” the entire sediment column after being underthrust). The source of salt below the deepest sediment recovered at Site 861 is problematic, but could be due to (1) upward diffusion of saline basement waters from a continental slab (see discussion below); (2) clay membrane filtration, also at great depth; or (3) penetration via lateral processes of hydrate-induced salt-enriched fluids at an updip or along-strike location in communication with the section below recovery (not likely considering the dominantly conductive nature of the thermal structure at this site).

Calcium, magnesium, alkalinity, strontium, and fluoride profiles in the upper 190 m indicate a series of competing diagenetic reactions, presumably associated with uptake and release into/from authigenic phases such as calcite, Mg-smectites, dolomites, carbonate, and fluorapatite, and/or alteration of ash, which is observed both as glass disseminated throughout the section, and in discrete intervals as a high green glauconitic (but X-ray amorphous) sand. All these constituents display prominent extrema at two diagnostic depths: (1) at about 65 mbsf (Ca-, Mg-, Alkalinity, F-, and Sr-maxima), and (2) at about 200 mbsf (clear inflections in the gradients of Ca, Mg, Alkalinity, Sr, F, and perhaps K and B). The depth of 210 mbsf corresponds closely to a lithologic boundary (see Lithostratigraphy section, this chapter) and a structural boundary (see Structural Geology section, this chapter), while 65 mbsf is the depth of a 23-cm-thick tuffaceous ash layer in Section 141-861C-8H-5 (see Lithostratigraphy section, this chapter). There is also a thin diagenetic “green-sand” (altered volcanic glass?) interval at about 170 mbsf and a limestone stringer at about 190 mbsf (see Lithostratigraphy section, this chapter). The latter could act both as a diagenetic front as well as a potential barrier to ion diffusion and also provide a reflector that we misidentified as a BSR. Whether the diagenetic reactions occur preferentially on these horizons for lithologic reasons, or the inflections in the profiles reveal lateral processes localized at these depths, is not clear.

Site 861 is underlain by (seismic) continental crust (much older accreted material), and thus might be expected to exhibit basement chemical-exchange characteristics different from Sites 859 and 863. In general, the pore-water profiles at Sites 860 and 861 are similar to each other and distinct from Sites 859 and 863. For example, the alkalinity, pH, SO₄, Mg, B, F, Li, NH₄, and Si profiles at Sites 860 and 861 are very similar, and likely reflect parallel in-situ diffusion-reaction processes associated with diagenesis of organic matter and clay minerals. However, the vertical gradients at Site 860 are more subdued than at Site 861 (the lateral “communication depths” are deeper at Site 860 than at Site 861). As Site 861 material accumulated faster than Site 860 (equivalent ages are deeper at Site 861 than at Site 860), this offset in age vs. diagenetic horizons between the two sites must reflect a closer source of Site 861 to the material undergoing reaction (higher influx of organic matter and continentally-derived minerals).

However, the dramatic downward-increasing Na-, Cl-, and Ca-profiles and downward-decreasing K- and Mg- gradients in the lower 100 m of Site 861 (gradients that are weak or nonexistent at Site 860) suggest the possibility of alkaline sericitization of plagioclase feldspar, mineral hydration reactions, and biotite chloritization in continental basement at elevated temperatures, perhaps comingled with upward diffusion of relict continental saline groundwaters, all far below recovery.

Table 9. Composition of headspace gases for sediments from Holes 861A, 861B, 861C and 861D.

Core, section, interval (cm)	Depth (mbsf)	Hydrocarbon concentration (ppm)								CO ₂	C ₁ (cm ³ /cm ³)	C ₁ /C ₂
		C ₁	C ₂	C ₃	<i>i</i> -C ₄	<i>n</i> -C ₄	<i>i</i> -C ₅	<i>n</i> -C ₅	C ₆₊			
141-861A- 1H-3, 147-150	4.5	10,032	0	0	0	0	0	0	0	1033	0.067	
141-861B- 1H-3, 137-140	4.4	15,885	0	0	0	0	0	0	0	201	0.106	
141-861C- 1H-1, 147-150	1.5	8	0	0	0	0	0	0	0	659	0.000	
2H-3, 137-140	7.4	40	0	0	0	0	0	0	0	1007	0.000	
3H-3, 142-145	16.9	12,835	0	0	0	0	0	0	0	3487	0.086	
4H-5, 137-140	29.4	38,942	0	0	0	0	0	0	0	4385	0.260	
5H-5, 142-145	37.9	24,879	0	0	0	0	0	0	0	2694	0.166	
6H-3, 137-140	45.4	4,022	0	0	0	0	1	0	0	3602	0.027	
7H-3, 137-140	54.9	12,043	0	0	0	1	0	0	1	3240	0.080	
8H-3, 132-135	64.3	12,295	0	0	0	0	0	0	0	2418	0.082	
10H-3, 137-140	75.4	12,074	0	0	0	0	0	0	0	1784	0.080	
12X-1, 132-135	91.4	9,377	tr	0	0	0	0	0	0	2163	0.063	
13X-1, 112-115	100.9	16,818	tr	0	0	0	0	0	0	3206	0.112	
14X-1, 132-135	110.7	10,053	2	0	0	0	0	0	0	1238	0.067	5027
15X-3, 137-140	123.4	13,292	5	0	0	0	0	0	2	3205	0.089	2658
16X-3, 132-135	133.2	13,649	5	0	0	0	0	0	0	4156	0.091	2730
17X-1, 137-140	140.1	10,089	5	0	0	2	0	0	0	nd	0.067	2018
18X-3, 132-135	152.8	6,234	5	0	0	0	0	0	0	3072	0.042	1247
19X-1, 67-71	159.0	5,737	4	0	0	0	0	0	0	1441	0.038	1434
21X-1, 120-125	171.5	7,752	6	0	0	0	0	0	0	1667	0.052	1292
22X-4, 137-140	185.8	10,882	13	0	0	0	0	0	0	1082	0.073	837
25X-4, 132-135	214.7	19,225	62	0	0	0	0	0	0	1178	0.128	310
27X-3, 77-80	223.9	14,646	73	0	0	0	0	0	0	307	0.098	201
28X-4, 96-99	233.6	9,826	63	0	0	0	0	0	0	275	0.066	156
29X-2, 14-17	239.4	5,604	14	0	0	0	0	0	0	nd	0.037	400
31X-2, 132-135	251.1	4,837	24	0	0	0	0	0	0	64	0.032	202
32X-1, 57-60	257.6	17,940	87	0	0	1	0	0	0	1543	0.120	206
33X-2, 0-3	268.1	13,431	70	0	0	0	0	0	0	2415	0.090	192
34X-5, 137-140	282.7	8,050	50	0	0	0	0	0	0	3289	0.054	161
35X-1, 50-53	286.5	12,295	68	0	0	0	0	0	0	1194	0.082	181
36X-2, 132-135	298.5	15,460	77	0	0	0	0	0	0	750	0.103	201
37X-1, 137-140	306.3	17,999	91	0	0	0	0	0	0	1216	0.120	198
39X-2, 44-47	326.2	26,485	65	0	0	0	0	0	0	181	0.177	407
40X-4, 45-48	338.9	8,767	48	1	0	0	0	0	0	75	0.058	183
41X-1, 132-135	344.7	13,395	60	0	0	0	0	0	0	186	0.089	223
141-861D- 1R-2, 137-140	345.2	13,027	59	0	0	0	0	0	0	252	0.087	221
2R-1, 132-135	353.2	8,011	43	0	0	0	0	0	0	63	0.053	186
6R-1, 74-77	391.2	27,758	79	0	0	0	1	0	0	30	0.185	351
7R-2, 122-125	402.8	119,143	150	0	0	0	14	0	0	286	0.794	794
8R-1, 110-112	410.9	16,433	60	0	2	0	0	0	0	129	0.110	274
9R-1, 127-130	420.7	19,559	60	0	0	0	0	0	0	216	0.130	326
10R-1, 147-150	430.6	20,547	59	0	0	0	0	0	0	357	0.137	348
11R-1, 102-105	439.8	13,202	21	0	0	0	0	0	0	323	0.088	629
12R-1, 147-150	450.0	20,827	41	0	0	0	0	0	0	nd	0.139	508
13R-2, 75-78	460.4	85,785	61	0	0	0	0	0	0	nd	0.572	1406
14R-1, 103-106	468.7	15,721	29	0	0	0	0	0	0	819	0.105	542
15R-1, 10-13	476.4	29,896	32	0	0	0	0	0	0	938	0.199	934
16R-1, 137-140	487.4	64,129	53	0	0	0	0	0	0	939	0.428	1210

PHYSICAL PROPERTIES

General

At Site 861, useful physical properties were obtained virtually exclusively by the collection and analysis of selected or routine sediment samples. Except for the interval from 0 to 10 mbsf, no useable information was gathered by the multisensor track (MST) scanning of whole-round cores for bulk density or acoustic velocity.

APC and XCB coring at Hole 861C recovered nearly-intact to slightly disrupted material to a depth of about 150 mbsf (Core 141-861C-18X). Core disturbance above this depth was caused chiefly by gas expansion, which effectively blanked the sensors of the *P*-wave logger (PWL) and gamma-ray attenuation porosity evaluator (GRAPE) of the MST. At greater depths, XCB coring fragmented semilithified sediments, and, along certain core sections, fluidized less-competent material. Rotary-cone drilling at Hole 861D (from 342.3 to 496.3 mbsf) usually fragmented the

sediment cores. Despite disruption, small pieces of intact core sediment could be selectively sampled for the determination of in-situ values for porosity, grain density, bulk density, and water content. However, core disturbance hampered measurement of acoustic velocity (either by the Hamilton Frame or digital sound velocimeter) and thermal conductivity.

Site 861 physical properties are described below under the headings of (1) index properties (grain density, porosity, water content, and bulk density), (2) acoustic (V_p) velocity, and (3) thermal conductivity. Because reliable GRAPE bulk density and PWL acoustic information is limited to the upper few meters of sediment, these data are not treated separately but, where useful, integrated into discussions and descriptions of other results. Based on changes in the index properties, three physical property units were identified (see Fig. 42): Unit A between 0-70 mbsf, Unit B between 70-200 mbsf, and Unit C below 200 mbsf. The boundaries of the physical property units correspond closely to lithologic breaks (see Lithostratigraphy chapter, this section).

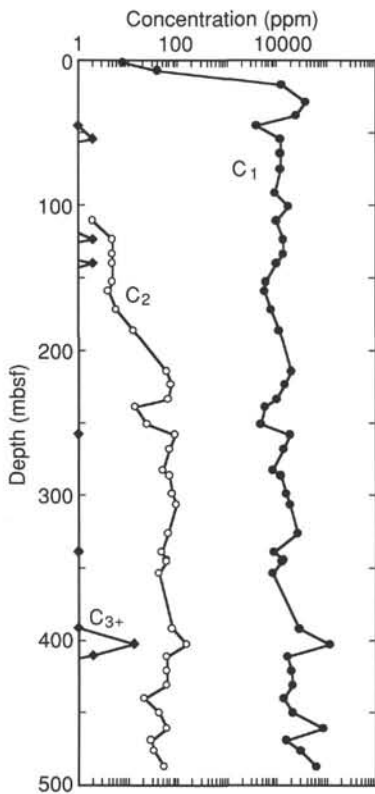


Figure 32. Composition of headspace gases vs. depth for sediments from Holes 861C and 861D.

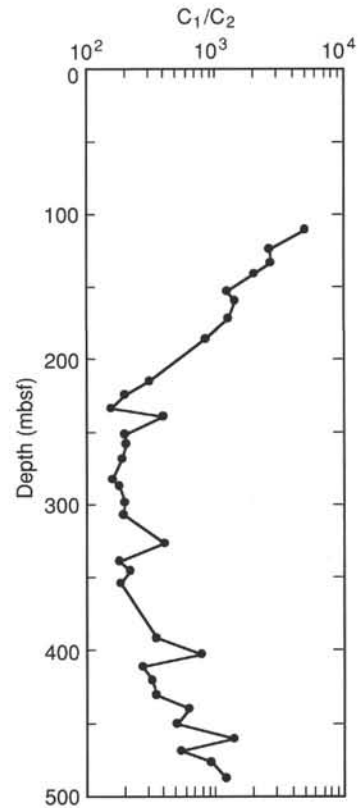


Figure 33. Methane/ethane ratios (C_1/C_2) vs. depth of gases from sediments of Holes 861C and 861D.

Index Properties

Index properties measured at Site 861 are listed in Table 16. Porosity, water content, grain density, and bulk density are displayed in Figure 42.

Porosity and Water Content

In Units A and B, the sedimentary column is undergoing compactive dewatering and the loss of pore space typical of accumulating depositional sequences. Lower porosity and water content characterize relatively thin (2–6 cm) limestone beds (denoted by “LS” on the porosity and water content graphs). Presumably these uncommon but dense layers reflect stratigraphically-localized concentrations of calcite deposition. Considerable variation in porosity and water content (typically 5%–10%, but as much as 15%–25%) exists across the stratigraphic thickness typically recovered within single cores, as a result of variations in the texture and granularity of interbedded clayey silt and silty clay, and the common occurrence of sandy units.

Although surface sediment exhibits a porosity of nearly 75%, at a depth of only 20 mbsf porosity falls to about 55%, and to about 50% at 50 mbsf. Below about 200 mbsf and coincident with the top of Unit C, the trend of downsection decrease in porosity and water content is reduced to a gradient of only 2.5%/100 m. Unit C consists of relatively lithified or “stoney” claystone and siltstone, whereas sediment above is much less consolidated.

Bulk Density

Because little downsection change occurs in grain density, wet-sediment bulk density increases with depth congruent with the downward decrease in volume of interstitial pore space. Sev-

eral small offsets to lower porosity occur in Unit C. These are presumably lithology-related because of the lack of any significant structures above 400 mbsf. Below 400 mbsf the development of broken formation (see Structural Geology section, this chapter) does, however, indicate significant deformation.

Grain Density

The variability in sediment grain density is typically 0.15 g/cm³, but is as high as 0.25 g/cm³, where limestone layers were recovered (Fig. 42). Grain density variability mainly reflects the contrasting textural parameters of interbedded material; for example, sandy layers containing heavy mineral debris extend the spread to values as high as 3.1 g/cm³. No change in average grain density occurs downsection, although the spread of values at specific stratigraphic levels appears to be somewhat higher for Unit C sediment (from about 200 to 500 mbsf). The mean grain density for Site 861 sediment is close to 2.75 g/cm³.

Sonic (V_p) Velocity

As at Sites 859 and 860, the upper 250 mbsf of Site 861 sediments were either mechanically too weak or too gas-disrupted to permit V_p measurements by either the Hamilton Frame (HF) or the digital sound velocimeter. An effort was made to avoid sediment crumpling caused by the slight load imposed by the HF transducers by confining the sediment sample within a small plastic box, which was carefully inserted into the open face of the working half of the split core. The four V_p values listed in Table 17 and plotted in Figure 42 for depths less than 72 mbsf are boxed measurements. Because all are under 1600 m/s, and little change is recorded with depth, the relation of these measurements to

Table 10. Domposition of gases from core expansion voids of sediments from Holes 861A, 861C, and 861D, and gases from pressure coring system Cores 141-861C-26P and -30P.

Core, section, interval (cm)	Depth (mbsf)	Hydrocarbon concentration (ppm)									CO ₂	C ₁ /C ₂	C ₁ /C ₃	C ₁ /n-C ₄	Pressure (psi)
		C ₁	C ₂	C ₃	i-C ₄	n-C ₄	i-C ₅	n-C ₅	C ₆₊						
141-861A-1H-6	8.7	67,077	0	0	0	2	0	0	2	973			33,539	2	
141-861C-3H-6	21.2	445,484	0	6	2	30	0	0	20	704		74,247	14,849	12	
4H-3	25.6	621,209	0	2	2	2	3	0	2	nd		310,605	310,605	21	
5H-3	34.5	921,372	7	3	1	3	2	0	2	nd	131625	307,124	307,124	22	
6H-2	43.3	933,214	11	2	1	19	0	0	12	nd	84838	466,607	49,117	14	
7H-3	54.3	661,711	10	2	2	47	2	0	26	387	66171	330,856	14,079	8	
8H-2	61.1	895,437	15	6	2	39	0	0	22	287	59696	149,240		18	
10H-1	71.7	957,627	26	2	0	0	0	0	0	nd	36832	478,814		4	
12X-2	92.2	898,750	65	5	1	0	0	0	0	345	13827	179,750		2	
4X-2	111.4	935,396	118	0	0	0	0	0	0	191	7927			4	
15X-2	120.7	929,217	167	4	0	0	2	0	0	nd	5564	232,304		0	
16X-3	132.9	974,313	259	5	0	0	2	0	0	373	3762	194,863		2	
17X-2	140.3	966,546	287	2	0	2	0	0	3	488	3368	483,273	483,273	0	
18X-1	149.9	789,152	284	3	2	52	2	2	30	665	2779	263,051	15,176	0	
21X-1	171.4	924,548	573	0	0	0	0	0	0	nd	1614			0	
22X-3	183.2	962,059	723	0	0	0	0	0	0	nd	1331			0	
25X-5	215.2	925,918	1404	8	2	42	1	1	22	nd	659	115,740	22,046	6	
27X-4	225.6	834,965	1276	5	0	0	0	0	0	978	654	166,993		4	
32X-2	258.7	876,737	1593	8	2	2	0	0	3	850	550	109,592	438,369	0	
34X-6	283.9	810,364	1300	8	2	0	0	0	0	888	623	101,296		0	
35X-3	288.3	828,978	1381	9	2	2	1	0	4	989	600	92,109	414,489	0	
36X-3	299.7	908,085	1503	10	2	1	0	0	0	nd	604	90,809	908,085	0	
37X-1	306.2	926,816	1533	12	3	0	1	0	0	862	605	77,235		0	
141-861D-6R-3	392.4	949,058	1340	6	3	2	4	0	0	nd	708	158,176	474,529	0	
7R-2	402.4	856,824	1066	4	2	2	3	0	1	nd	804	214,206	428,412	0	
12R-2	450.0	924,212	716	3	0	2	3	0	2	nd	1291	308,071	462,106	0	
16R-2	488.2	172,652	66	0	0	3	0	0	6	774	2616		57,551	0	
141-861C-26P-PCS#11		390,218	520	tr	tr	0	0	0	0	nd	750				
30P-PCS#12		902,348	1200	5	1	0	0	0	0	749	752	180,470			

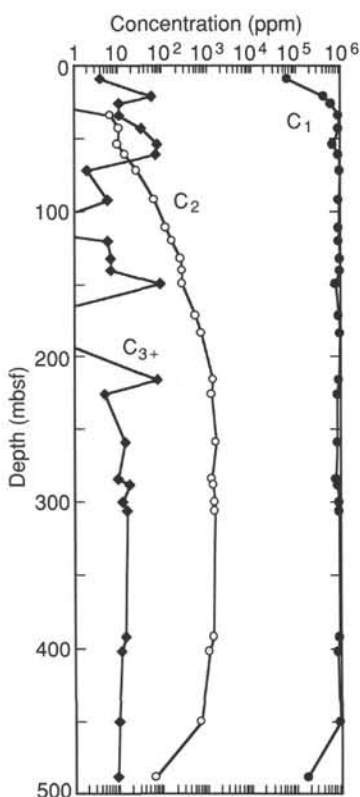


Figure 34. Composition of core expansion void gases vs. depth for Holes 861A, 861C, and 861D.

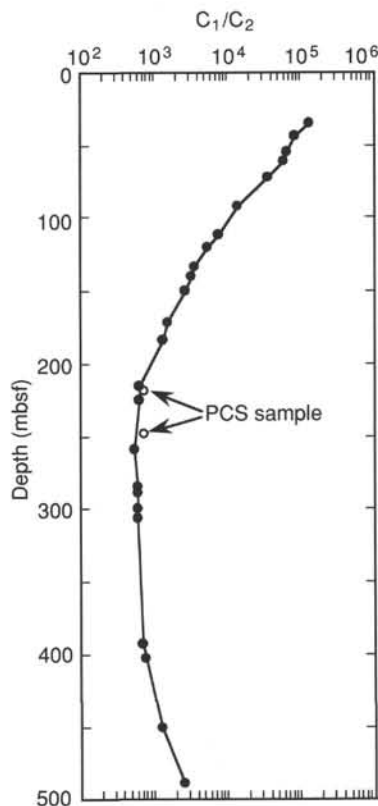


Figure 35. Methane/ethane ratios (C₁/C₂) vs. depth of gases from core expansion voids from cores of Holes 861A, 861C, 861D, and PCS gases from deployments 141-861C-26P and -30P.

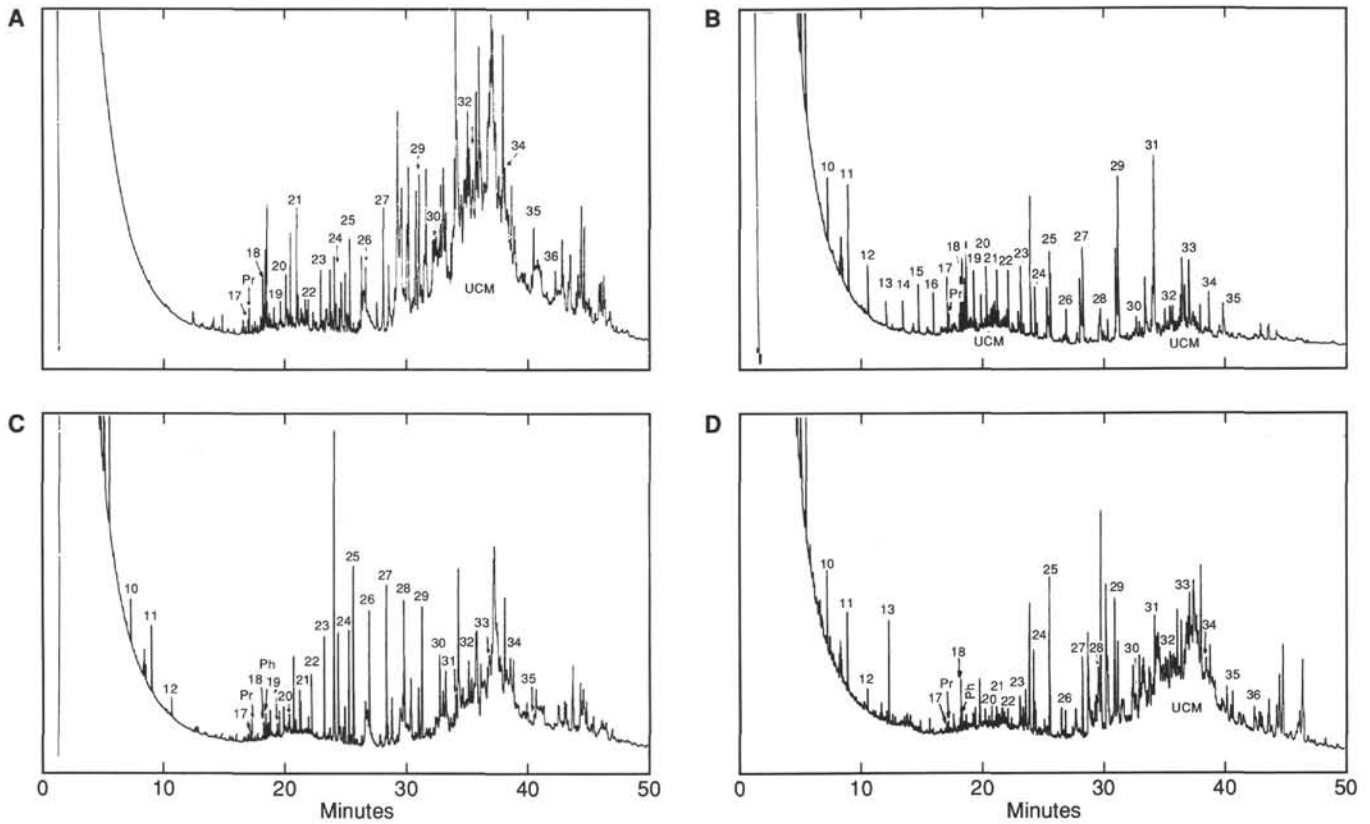


Figure 36. Gas chromatographic traces of the bitumen (hexane soluble matter) of sediments from Holes 861C and 861D: (A) Sample 141-861C-6H-3, (B) Sample 141-861C-14X-1, (C) Sample 141-861C-25X-4, (D) Sample 141-861C-6R-1. Numbers refer to carbon chain length of n-alkanes, Pr = pristane, Ph = phytane, UCM = unresolved complex mixture of branched and cyclic compounds).

Table 11. Extractable bitumen of sediments from Holes 861C and 861D.

Core, section, interval (cm)	Depth (mbsf)	C _{max}	C _{range} C _i -C _f	Pr/Ph	Pr/n-C ₁₇	Ph/n-C ₁₈	CPI	Organic matter type
141-861C-								
1H-1	1.5	18;31	10-38	0.26	1.20	3.67	1.88	Mar = Terr
6H-3	45.4	21;31	13-36	0.92	1.83	0.50	3.48	Mar < Terr
14X-1	110.7	21;31	10-36	0.26	0.33	2.33	3.23	Mar = Terr
16X-3	133.2	21;31	10-36	0.89	4.00	3.60	1.71	Mar < Terr
21X-1	171.5	21;31	15-36	1.85	3.43	3.33	2.07	Mar < Terr
25X-4	214.7	25	10-36	0.67	2.00	3.33	1.01	Mar < Terr
34X-5	282.7	19;33	10-36	1.25	2.50	1.00	3.33	Mar < Terr
39X-2	326.2	25	10-36	0.29	0.50	0.37	0.87	Mar < Terr
141-861D-								
1R-2	345.3	33	16-36	1.14	2.67	1.75	2.91	Mar < Terr
6R-1	391.1	25	10-36	0.69	1.38	5.93	2.61	Mar < Terr
9R-1	420.7	25	10-36	0.29	1.00	2.33	1.44	Mar < Terr
12R-1	450	25	10-36	0.29	0.25	0.39	1.06	Mar < Terr
16R-1	487.4	27	16-37	0.67	1.33	3.90	2.21	Mar < Terr

Mar = marine; Terr = terrestrial.

in-situ values is questioned. However, the most reliable PWL velocity readings in the upper 10 mbsf of section are similarly between 1500 and 1600 m/s.

Below a depth of 200 mbsf, and within the more lithified deposits of Unit C, good V_p measurements were obtained on core fragments sufficiently rigid to withstand the cutting of smooth faces and transducer interfacing (Table 17). With the exception of a highly calcareous layer (indicated by "LS" on velocity chart in Fig. 42), HF- V_p velocity measurements roughly define a trend of V_p increasing downward by about 400 m/s for each 100 m depth. At a depth of 488 mbsf, near the base of Hole 861D, claystone beds attain a velocity of approximately 2700 m/s.

Thermal Conductivity

Thermal conductivity (TC) measurements are presented in Table 18 and displayed in Figure 42. In APC-cored sediment (0-10 mbsf) at Holes 861A, 861B, and 861C, TC ranges from 1.08 to 1.56 W/m·K. This spread of values corresponds to the wide range of porosity (73% - 57%) and bulk density (1.55-1.80 g/cm³) determined for surface sediment. At depths below about 20 mbsf (Section 141-861C-3H-4) gas disruption of the sedimentary fabric of APC cores introduced an equally broad scatter of TC values. A spread of thermal conductivity measurements is especially noticeable below a depth of about 100 mbsf where XCB

Table 12. Rock-Eval data and total organic carbon (TOC) of sediments from Holes 861C and 861D.

Core, section, interval (cm)	Depth (mbsf)	T _{max} (°C)	S ₁ (mg/g)	S ₂ (mg/g)	S ₃ (mg/g)	TOC (%)	HI	OI	PI	S ₂ /S ₃
141-861C-										
1H-1, 97-99	1.0	414	0.56	2.44	3.54	1.36	179	260	0.19	0.69
1H-2, 98-100	2.5	408	0.20	0.71	1.86	0.59	120	315	0.22	0.38
2H-1, 96-98	4.0	402	0.11	0.39	1.07	0.45	87	238	0.22	0.36
2H-4, 99-101	8.5	414	0.19	0.77	1.34	0.64	120	209	0.20	0.57
3H-3, 112-114	16.6	408	0.18	0.71	2.14	0.66	108	324	0.20	0.33
4H-1, 81-83	22.8	405	0.13	0.41	1.52	0.50	82	304	0.24	0.27
6H-1, 64-66	41.6	391	0.11	0.39	1.93	0.41	95	471	0.22	0.20
8H-3, 40-42	63.4	384	0.09	0.30	1.91	0.43	70	444	0.23	0.16
10H-2, 103-105	73.5	464	0.08	0.32	0.78	0.30	107	260	0.20	0.41
12X-2, 19-21	91.8	581	0.05	0.22	0.75	0.23	96	326	0.19	0.29
14X-1, 50-52	109.9	570	0.08	0.33	0.88	0.29	114	303	0.20	0.38
16X-1, 57-59	129.5	407	0.13	0.74	1.39	0.61	121	228	0.15	0.53
18X-1, 76-78	149.3	545	0.10	0.48	1.00	0.39	123	256	0.17	0.48
21X-1, 14-16	170.3	411	0.16	0.58	1.22	0.46	126	265	0.22	0.48
22X-1, 44-46	180.3	409	0.14	0.56	1.55	0.54	104	287	0.20	0.36
24X-CC, 12-14	199.3	397	0.12	0.48	1.62	0.42	114	386	0.20	0.30
25X-3, 110-112	210.0	464	0.07	0.38	1.37	0.43	88	319	0.16	0.28
27X-1, 83-85	220.9	385	0.13	0.71	1.52	0.50	142	304	0.15	0.47
29X-1, 94-96	238.6	403	0.08	0.42	0.65	0.29	145	224	0.16	0.65
34X-4, 26-28	281.0	410	0.09	0.41	0.88	0.40	103	220	0.18	0.47
36X-1, 16-18	295.8	376	0.07	0.32	0.33	0.15	213	220	0.18	0.97
37X-1, 16-18	305.1	399	0.09	0.48	0.71	0.43	112	165	0.16	0.68
39X-2, 39-41	326.1	411	0.13	0.53	0.86	0.43	123	200	0.20	0.62
41X-1, 75-77	344.2	413	0.08	0.38	1.08	0.43	88	251	0.17	0.35
141-861D-										
2R-2, 8-10	353.5	541	0.13	0.31	0.31	0.31	100	100	0.30	1.00
6R-1, 50-52	390.9	389	0.12	0.46	1.20	0.38	121	316	0.21	0.38
10R-1, 28-30	429.4	473	0.04	0.23	0.40	0.28	82	143	0.15	0.58
12R-2, 0-11	450.1	407	0.04	0.18	0.81	0.32	56	253	0.18	0.22
14R-1, 106-116	468.8	414	0.07	0.36	0.73	0.58	62	126	0.16	0.49
16R-1, 140-150	487.5	411	0.03	0.15	0.37	0.30	50	123	0.17	0.41

Note: T_{max} values for samples with S₂ contents less than 0.5 mg HC/g sediment are inaccurate and should be rejected.

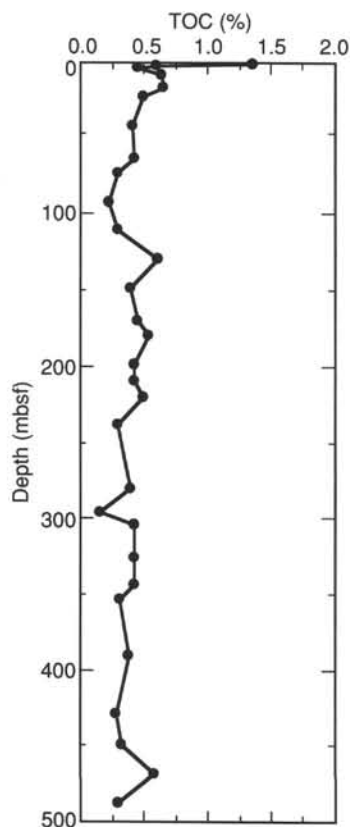


Figure 37. Total organic carbon content (Rock-Eval) vs. depth of sediments from Holes 861C and 861D.

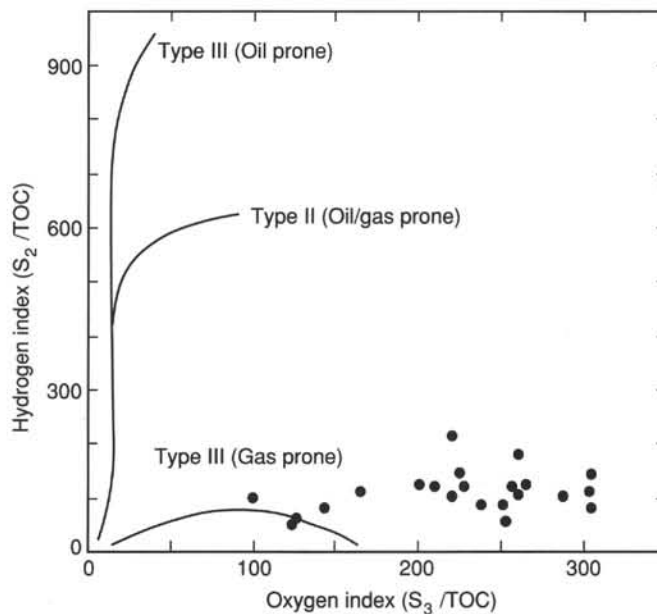


Figure 38. Hydrogen index vs. oxygen index diagram (Rock-Eval) of organic matter of sediments from Holes 861C and 861D.

coring was carried out. XCB cores were partly or greatly disrupted, which created fluid or air pockets that undermined the accurate determination of in-situ thermal conductivity.

With increasing depth below 250 mbsf, fewer and fewer core fragments were found that would not split during probe insertion (with or without the drilling of a small pilot or guide hole). As a consequence, the number of TC measurements sharply falls off

Table 13. Interstitial water data obtained from squeezing whole rounds in titanium squeezers for Site 861.

Core, section, interval (cm)	Depth (mbsf)	IW vol. (mL)	pH	Alk (mM) (Gran)	Sal (Refr)	Cl (mM) (Tit'n)	SO ₄ (mM) (BaSO ₄)	NH ₄ (μM) (Spec)	Si (μM) (Spec)	Mg (mM) (Tit'n)	Ca (mM) (Tit'n)	K (mM) (AES)	Sr (μM) (AAS)	F (μM) (ISE)	B (mM) (Spec)	Na (mM) (AES)	Li (μM) (AES)
141-861B-1H-3, 145-150	4.45	38	7.86	18.12	34.0	554	11.60	6,000	550	45.50	4.08	11.50	70	56.1	0.57	462	22
141-861C-																	
2H-3, 145-150	7.45	19	8.12	28.28	33.0	560	0.30		476	43.64	1.43	11.70	59	51.8	0.62	455	14
3H-3, 145-150	16.95	43	7.96	39.48	34.0	571	0.30		600	46.41	1.19	12.40	59	59.0	0.70	480	21
4H-5, 145-150	26.45	31	7.98	48.15	34.0	560	0.20		632	50.38	1.45	12.30	61	60.7	0.70	484	26
5H-5, 145-150	37.75	22	7.86	52.54	35.0	559	0.20		665	51.60	2.09	12.20	66	60.5	0.72	477	
6H-3, 145-150	45.45	8			37.0	562	0.30		578	54.17	2.62	12.20	67	61.9	0.72	461	27
7H-3, 140-150	54.90	17	7.87		37.0	562	0.30		537	55.00	2.99	11.80	68	67.0	0.71	467	27
8H-3, 140-150	64.40	45	7.83	62.41	38.0	566	0.30	25,000	667	53.88	2.76	12.50	68	67.8	0.71	470	28
10H-3, 140-150	75.40	32	7.93	61.72	38.0	571	0.20		635	53.64	2.60	12.50	68	62.9	0.74	478	32
12X-1, 140-150	91.50	37	8.00	55.55	35.5	565	0.30		579	49.99	2.38	12.40	66	58.3	0.69	480	33
14X-1, 140-150	110.80	22	7.89	50.93	36.0	565	0.70		602	48.50	2.62	11.50	65	55.4	0.67	474	31
15X-3, 140-150	123.40	45	7.94	44.93	36.0	568	1.10		667	45.62	2.85	11.30	63	52.4	0.68	477	32
16X-3, 140-150	133.30	11	8.16	40.69	34.5	570	1.30		595	43.31	2.79	11.90	63	55.0	0.67	475	35
17X-1, 140-150	140.10	34	8.13	40.64	34.5	566	0.30		735	42.78	2.52	11.30	58	51.8	0.72	477	34
18X-3, 140-150	152.90	29	8.04	34.86	34.5	575	0.40		654	40.19	2.01	11.80	58	52.0	0.66	477	35
21X-1, 140-150	171.60	26	8.06		34.5	572	0.30		721	36.31	1.11	12.00	58	50.8	0.68	493	33
22X-4, 140-150	185.80	18	8.09		34.0	578	0.40		779	32.88	1.00	11.60	55	47.6	0.70	510	33
25X-4, 140-150	214.80	8			34.0	573	3.20		591	34.12	2.29	11.10	59	41.8	0.60	512	36
26P-1, 40-60	219.00	26	8.00	20.97	34.0	585	1.10		706	33.69	1.74	10.90	56	40.0	0.60	510	38
27X-3, 80-90	223.41	20	8.18	22.00	34.0	585	0.40	26,000	744	31.93	1.68	10.90	56	37.4	0.61	508	38
28X-4, 104-114	233.64	5			33.5	582	2.40		793	32.51	2.07	10.20	56	39.4	0.59	493	42
32X-1, 60-70	257.60	19	8.25	18.35	34.0	581	2.20		755	31.02	2.83	10.30	60	40.6	0.51	500	50
33X-1, 140-150	268.00	8			34.0	592	0.70		1161	30.04	3.03	9.90	63	41.0	0.54	501	54
34X-5, 140-150	281.17	3			34.0	588	1.40		638	29.74	3.52	9.30	63	34.8	0.45	514	52
35X-1, 53-63	286.43	18	8.31		34.0	590	1.80			29.00	3.22	11.40	59	33.2	0.44	520	52
36X-2, 140-150	298.50	7			34.0	587	2.60		660	28.39	3.54	10.90	66	32.9	0.45	519	53
7X-1, 140-150	306.30	16	8.12	15.40	35.0	587	1.20		666	28.23	3.71	10.40	67	33.7	0.44	509	48
39X-2, 52-62	326.22	15	8.26	14.70	34.5	593	1.90	24,000	644	27.13	4.38	10.60	71	35.1	0.34	525	52
40X-4, 48-58	338.88	3			35.0	598	3.50			4.85	10.60	76	35.7	0.33	546	59	
41X-1, 140-150	344.80	14	8.37	12.58	34.5	600	1.70		650	25.31	4.49	10.90	74	35.7	0.32	519	57
141-861D-																	
1R-2, 140-150	345.20	6			34.5	602	1.40			24.56	4.44	10.90	74	38.8	0.28	532	59
6R-1-1, 77-87	391.17	4			34.0	599	2.70			24.72	7.22	9.10	90	35.8	0.26	526	55
7R-2, 125-135	402.85	8			35.0	621	2.30	22,000		23.98	7.18	10.20	94	33.5	0.25	545	59
9R-1, 134-145	420.74	3			35.0	618	1.20			23.11	8.20	9.60	98	32.9	0.22	549	60
12R-2, 0-10	450.00	1			36.0	627	3.20					10.40		35.2		554	
13R-2, 83-93	460.43	3			36.0	634	1.00			20.93	13.59	7.70	104	36.4	0.10	561	66
14R-1, 106-116	468.76	4			36.0	640	0.60			20.09	14.32	7.60	99	33.3	0.12	542	55
15R-1, 0-10	476.30	6			36.0	619	3.80	16,000		23.46	16.36	7.30	95	35.5	0.13	548	47
16R-1, 140-150	487.00	1			38.0	650	3.40							0.14			

Note: Sample 26P (Core 141-861C-26P; 219.0 mbsf) was obtained by squeezing 20 cm of the core recovered by the pressure core sampler (PCS).

below 270 mbsf and no geologically meaningful measurements were possible below 350 mbsf. Half-space measurement techniques could not be used owing to the small size of the recovered material. Despite the spread and wide spacing of data points, a trend of downward-increasing thermal conductivity can arguably be discerned beginning below 200 mbsf, which is coincident with the top of the lithified deposits of Unit C.

Discussion and Overview

The rapid subsurface loss of intergranular space exhibited by the uppermost part of Unit A is similar to, but not as pronounced as, that displayed by the surficial deposits at Sites 860 and 859. At Site 861, porosity, water content, and bulk density data (Fig. 42) identify a roughly 150-m-thick section from about 70 to 200 mbsf (Unit B) of higher porosity and lower bulk density than predicted by the compaction profile established in overlying deposits. This apparently underconsolidated material corresponds closely to the stratigraphic limits of lithologic Subunit IIA (see Lithostratigraphy section, this chapter), which includes sand and coarser grained beds that should contribute to a reduction rather than an increase in porosity. Presumably, the "increased" volume of pore space reflects rigidity to compaction imparted by the coarse detritus, which in turn bestows an unusually high grain density to the beds of lithologic Subunit IIA (Fig. 42).

At Site 861, incipient lithification or cementation processes rigidify sediment below 200 mbsf. Even though hard to the touch, siltstone and claystone fragments of Unit C are nonetheless brittle and easily broken with finger pressure. At the base of Hole 861D (496.3 mbsf), siltstone of Core 141-861D-16R could not be disaggregated by wet-grinding or pulverizing in a dispersive agent

(Calgon). However, disaggregation was largely accomplished by digestion of the pulverized sediment in 10% HCl (room temperature). Digestion releases only a small amount of clay-size residue. Evidently, an important lithification process is intergranular deposition of micritic carbonate.

Between 50 and 500 mbsf, additional downsection loss of porosity is surprisingly little, only about 15% (reduction from 53%–38%). The average gradient of porosity loss is thus also small, only 3.3%/100 m.

WSTP AND ADARA TEMPERATURE MEASUREMENTS

Site 861 is situated in a mid- to upper-slope position in a slope basin. A lower geothermal gradient was expected at Site 861 than at either Sites 859 or 860 because of its greater distance from the oceanic spreading center. A moderately clear BSR also occurs on seismic reflection sections at approximately 220–250 mbsf near this site, suggesting a gas hydrate layer was locally developed. The principal objectives of the temperature measurement program at Site 861 were as follows:

1. To determine the principal mechanism of heat transport,
2. To establish the geothermal gradient, and
3. To determine the temperature at the depth of the BSR observed on seismic reflection sections.

At Site 861, the WSTP tools were deployed 10 times, four of which produced usable results. The ADARA tool was deployed six times, and we obtained usable results from five of the runs.

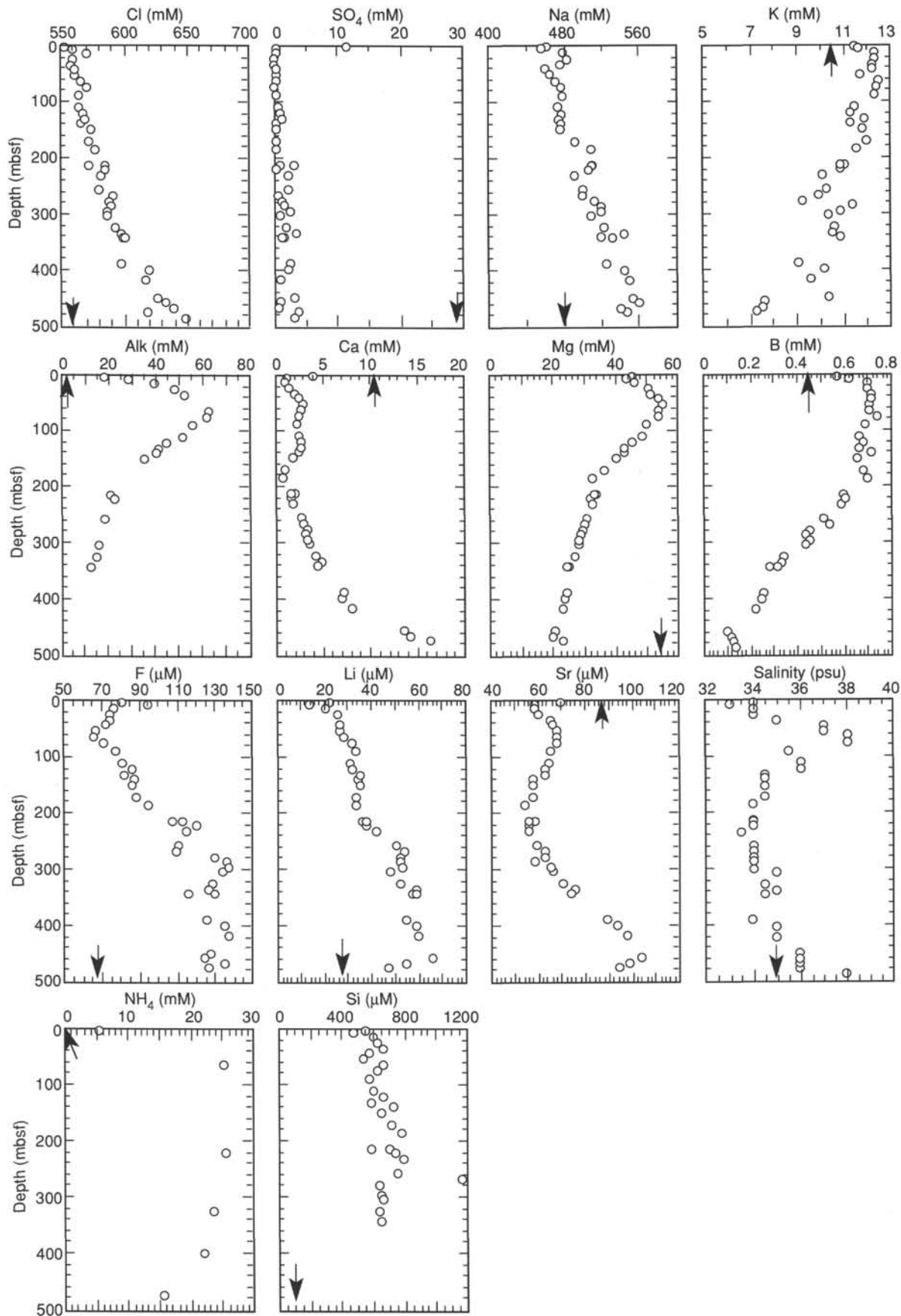


Figure 39. Interstitial water compositions vs. depth for Site 861. All data are from squeezed whole rounds of APC, XCB, or PCS cores. Arrows on axes indicate seawater concentrations for each constituent, where appropriate.

Table 14. Interstitial water data obtained from WSTP runs for Site 861.

Core	Depth (mbsf)	Designation	Vol. (mL)	Sal. (Refr)	Cl (mM)	SO ₄ (mM)	Mg (mM)	Ca (mM)	F (μM)	B (mM)
141-861C-7H	50.5	WT	3.5	35	579	0.9	58.03	3.79	67.6	0.6
7H		WO	62	14	232	7.7	22.38	3.32	181.6	0.23
12X		WT	4	31.5	548	11.8	52.78	5.39	66	0.54
12X	90	WO	98	18	304	10.7	29.58	4.12	101.7	0.27
15X		WT	5	32	533	16.5	52.77	6	10834	0.4
15X	119	WO	83	11	195	7.3	18.12	2.5	129.1	0.17
141-861C-26P		219	PO	4.8		544		50.79	9.71	72

Note: Sample 26P.PO is a headspace fluid sample obtained from PCS #11 (Core 141-861C-26P).
 WT - titanium coil; WO - overflow chamber; PO - pressure core sampler supernatant fluid.

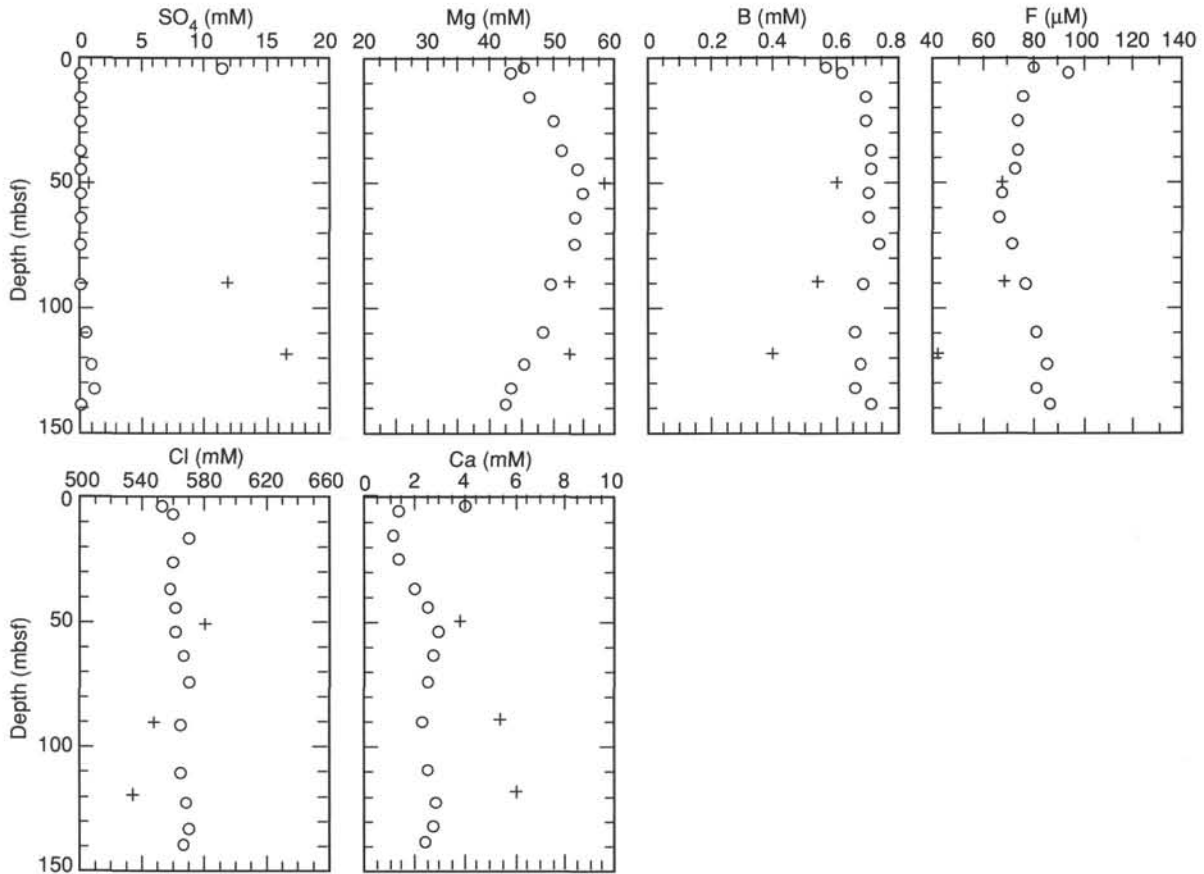


Figure 40. Comparison of interstitial water (IW) data from squeezed whole rounds (open circles) and from the WSTP (crosses).

Table 15. Composition of gas trapped inside the WSTP titanium coils as a result of gas expansion.

Core	Depth (mbsf)	C ₁ (ppm)	C ₂ (ppm)	C ₁ /C ₂
141-861B-7H	50.5	7.72×10 ⁵	8.64	89308
12X	90	6.40×10 ⁵	30.01	21324
15X	119	1.74×10 ⁵	13.07	13325

WSTP Results

Repeated tool disturbance and cracking of the formation caused considerable problems for the two WSTP tools. Despite these problems, the WSTP tools obtained critical measurements relatively deep in the hole that constrain the temperature profile. The successful deployments of the WSTP tool were at 50.5, 90.1, 189.6, and 228.1 mbsf.

Data from the deployment at 50.5 mbsf (with the newer WSTP tool) is badly disturbed and looks unusable on initial appearance (Fig. 43). In 1/t space, however, we can clearly separate out three points of disturbance with intervening periods where fairly linear cooling trends become established (X, Y, and Z, Fig. 43). When these three trends are extrapolated, they all give relatively similar

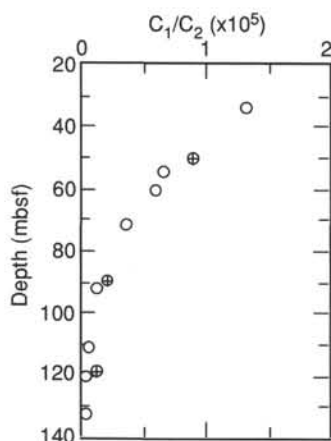


Figure 41. Comparison of methane to ethane ratios obtained from standard vacuiner sampling (open circles) with those obtained from headspace gases of the WSTP titanium coil (crossed circles).

temperatures of $6.61^\circ \pm 0.02^\circ\text{C}$. The pronounced temperature spike on the final extraction of the probe from the formation (Fig. 43B), and the consistency of the results in $1/t$ space suggests that the tool remained in the formation and that a new cooling trend was established after each interference.

The early part of the deployment of the older WSTP tool at 90.1 mbsf was normal in all respects other than at the end of the equilibration period, 11 min after formation penetration, when the temperature started falling slightly to form the characteristic data "hook" commonly developed at longer time intervals in the WSTP data (Fig. 44). The $1/t$ extrapolation to the early main linear trend of the data indicates a formation temperature of $8.47^\circ \pm 0.03^\circ\text{C}$. The deployment of the older WSTP tool at 189.6 mbsf provided

a very good temperature record (with a temperature spike at both the penetration and extraction of the tool) that indicates a formation temperature of $14.48^\circ \pm 0.03^\circ\text{C}$ at this depth (Fig. 45). Once again, however, toward the end of the equilibration period (after approximately 9 min) a temperature anomaly interferes with the reading.

In the case of the final deployment of the older WSTP tool, at 228.1 mbsf, the penetration record looks good (Fig. 46). In $1/t$ space, however, only the first 7 min of data fall on the linear extrapolation to a formation temperature of 16.25°C . Note that the data hook at small $1/t$ values looks pronounced only because of the greatly expanded temperature scale. We do not know why the data hook trends to slightly higher temperatures in this particular case, but in any event the error in this reading is unlikely to be greater than 0.01°C .

The WSTP deployments at 90.1 and 189.6 mbsf are considered to be generally more reliable than those at 50.5 and 228.1 mbsf. The WSTP temperature data set as a whole, however, has a great degree of internal consistency when plotted against sub-bottom depth.

ADARA Temperature Measurements

The quality of the ADARA measurements at this site is variable but we had a high proportion of deployments that produced usable data. Successful deployments were made at 22, 31.5, 41, 50.5, and 60 mbsf. The latter two deployments produced particularly good thermal decay curves.

Commonly, ADARA temperature decay profiles are disturbed by tool movement. Where possible we have fitted the best two portions of the decay profile with the shipboard APCTFIT program. In addition, due to the spread in the values of the measured thermal conductivity data in the upper part of Site 861 (see Physical Properties section, this chapter), we decided to use two thermal conductivities (1.1 and 1.2 W/m-K) for each analysis to

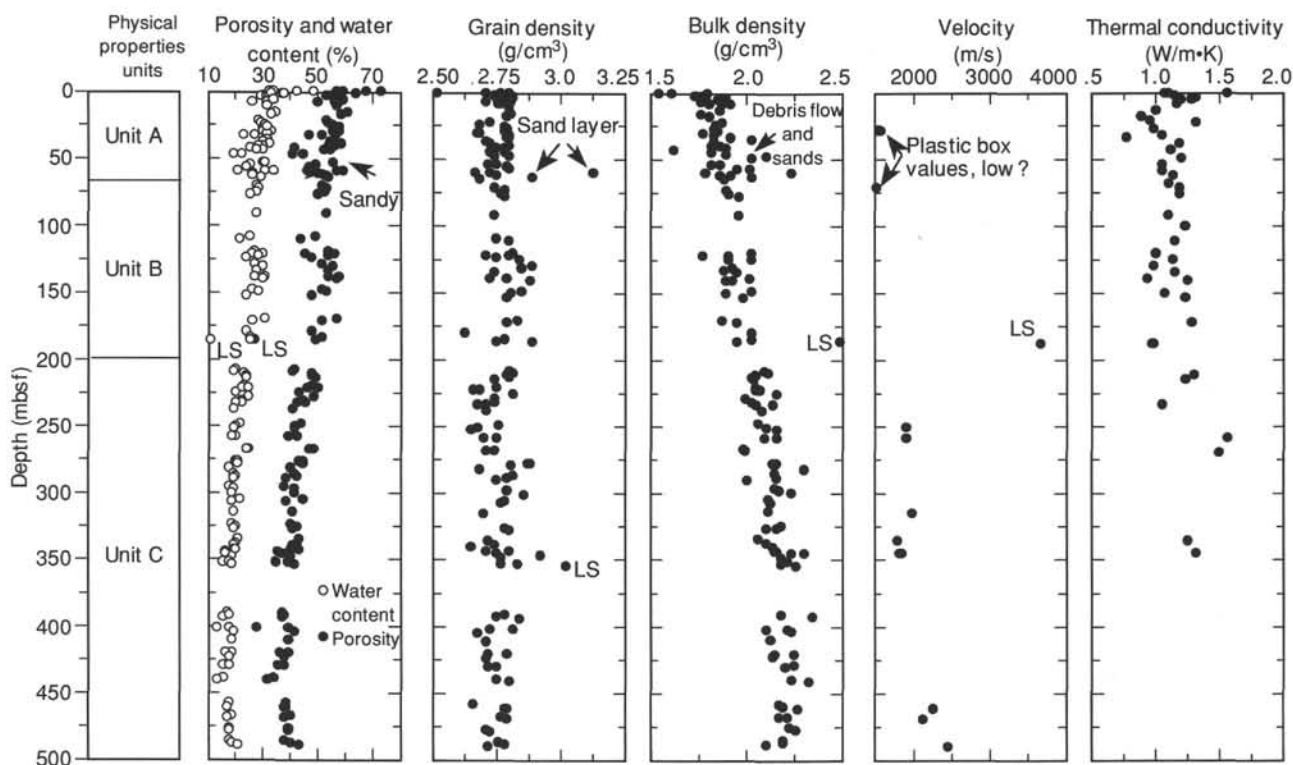


Figure 42. Sediment index properties; V_p and thermal conductivity vs. depth for all holes at Site 861. LS indicates a limestone bed.

Table 16. Index physical properties for Site 861.

Core, section, interval (cm)	Depth (mbsf)	Wet-bulk density (g/cm ³)	Dry-bulk density (g/cm ³)	Grain density (g/cm ³)	Wet porosity (%)	Dry porosity (%)	Wet-water content (%)	Dry-water content (%)	Wet void ratio	Dry void ratio
141-861A-										
1H-1, 69	0.69	1.80	1.22	2.77	57.0	56.8	32.4	48.0	1.33	1.30
1H-1, 145	1.45	1.78	1.17	2.80	59.4	59.0	34.2	52.1	1.46	1.42
1H-2, 100	2.50	1.79	1.20	2.81	57.7	57.8	33.1	49.4	1.36	1.35
1H-3, 98	3.98	1.86	1.29	2.77	54.9	54.3	30.3	43.5	1.22	1.18
1H-5, 100	7.00	1.87	1.28	2.81	58.0	56.3	31.8	46.6	1.38	1.28
1H-6, 100	8.50	1.81	1.23	2.76	56.7	56.2	32.0	47.1	1.31	1.27
141-861B-										
1H-1, 100	1.00	1.62	0.92	2.71	67.8	66.8	42.9	75.3	2.10	1.99
1H-2, 100	2.50	1.74	1.09	2.75	63.6	61.8	37.4	59.7	1.75	1.60
1H-2, 100	4.00	1.90	1.32	2.82	56.4	54.9	30.4	43.8	1.29	1.21
1H-2, 100	5.50	1.85	1.26	2.78	56.9	55.8	31.5	46.1	1.32	1.25
1H-2, 102	7.02	1.80	1.19	2.76	59.6	58.2	33.9	51.3	1.48	1.38
1H-2, 99	8.49	1.92	1.40	2.76	50.5	50.1	27.0	36.9	1.02	0.99
141-861C-										
1H-1, 100	1.00	1.55	0.80	2.52	73.3	70.2	48.5	94.4	2.75	2.32
1H-2, 100	2.50	1.73	1.07	2.74	63.9	62.2	37.9	61.0	1.77	1.63
2H-1, 100	4.00	1.87	1.32	2.75	53.6	53.1	29.4	41.7	1.16	1.12
2H-3, 100	7.00	1.77	1.16	2.71	59.6	58.4	34.4	52.5	1.48	1.39
2H-4, 100	8.50	1.87	1.28	2.77	57.7	55.8	31.6	46.3	1.36	1.25
2H-7, 40	12.40	1.86	1.27	2.80	57.4	56.1	31.6	46.3	1.35	1.26
3H-3, 110	16.60	1.77	1.15	2.81	60.7	59.9	35.0	53.9	1.54	1.48
3H-4, 100	18.00	1.81	1.21	2.79	58.7	57.7	33.2	49.7	1.42	1.35
4H-1, 82	22.82	1.87	1.33	2.73	53.4	52.6	29.2	41.2	1.14	1.10
4H-2, 82	24.32	1.84	1.29	2.69	53.9	53.1	29.9	42.7	1.17	1.12
4H-3, 82	25.82	1.84	1.27	2.78	55.9	55.3	31.1	45.2	1.27	1.23
4H-4, 92	27.42	1.83	1.25	2.79	57.5	56.5	32.1	47.3	1.35	1.29
4H-5, 93	28.93	1.85	1.29	2.78	55.3	54.7	30.6	44.0	1.24	1.19
4H-6, 93	30.43	1.78	1.19	2.68	57.6	56.7	33.1	49.5	1.36	1.29
5H-1, 29	31.79	1.83	1.27	2.69	55.2	54.2	30.8	44.6	1.23	1.17
5H-2, 72	32.52	1.83	1.25	2.80	57.1	56.4	31.9	46.9	1.33	1.28
5H-3, 80	34.10	1.92	1.39	2.80	51.5	51.1	27.5	37.9	1.06	1.04
5H-4, 16	34.96	2.03	1.55	2.79	47.2	46.2	23.8	31.3	0.89	0.85
5H-5, 84	37.14	1.83	1.25	2.71	56.5	55.3	31.7	46.4	1.30	1.22
5H-6, 122	39.02	1.86	1.29	2.73	55.0	53.9	30.3	43.5	1.22	1.16
5H-7, 106	40.36	1.82	1.22	2.80	58.7	57.6	32.9	49.1	1.42	1.34
5H-8, 71	41.51	1.89	1.31	2.78	56.1	54.5	30.5	43.8	1.28	1.19
6H-1, 68	41.68	1.89	1.34	2.75	53.7	52.7	29.1	41.1	1.16	1.10
6H-2, 68	43.18	1.63	1.20	2.74	41.5	48.8	26.1	35.4	0.71	0.94
6H-3, 69	44.69	1.82	1.26	2.73	54.7	54.5	30.7	44.4	1.21	1.18
6H-4, 19	45.69	1.90	1.36	2.78	52.6	52.0	28.3	39.5	1.11	1.07
6H-6, 5	48.55	2.02	1.56	2.80	45.2	45.1	23.0	29.8	0.83	0.81
6H-5, 104	48.04	2.10	1.67	2.74	41.2	40.5	20.1	25.2	0.70	0.67
7H-3, 100	54.50	1.86	1.29	2.75	55.4	54.4	30.5	43.9	1.24	1.18
7H-3, 60	54.10	1.82	1.25	2.72	55.4	54.9	31.2	45.4	1.24	1.21
7H-4, 140	56.40	1.95	1.45	2.79	49.6	49.2	26.0	35.1	0.98	0.96
7H-5, 60	57.10	2.01	1.53	2.80	47.1	46.6	24.0	31.6	0.89	0.87
7H-7, 100	60.50	1.79	1.18	2.73	59.6	58.2	34.1	51.8	1.48	1.38
7H-8, 10	61.10	1.86	1.28	2.67	57.3	54.8	31.5	46.0	1.34	1.20
8H-1, 27	60.27	2.23	1.75	3.13	46.3	45.4	21.3	27.0	0.86	0.83
8H-2, 110	62.60	1.92	1.40	2.75	50.5	50.0	27.0	36.9	1.02	0.99
8H-3, 41	63.41	2.02	1.48	2.89	52.4	50.8	26.6	36.2	1.10	1.02
8H-4, 100	65.50	1.88	1.33	2.69	54.1	52.6	29.5	41.8	1.18	1.10
10H-1, 106	72.06	1.89	1.36	2.74	51.8	51.4	28.1	39.1	1.07	1.05
10H-2, 100	73.50	1.89	1.34	2.78	53.1	52.6	28.8	40.5	1.13	1.10
10H-4, 119	76.69	1.91	1.37	2.77	52.5	51.8	28.2	39.3	1.11	1.06
10H-5, 91	77.91	1.96	1.45	2.78	50.2	49.3	26.2	35.6	1.01	0.96
12X-2, 16	91.76	1.96	1.41	2.74	53.5	51.2	28.0	38.8	1.15	1.04
14X-1, 54	109.94	1.97	1.46	2.75	49.7	48.6	25.8	34.8	0.99	0.94
14X-2, 31	111.21	2.07	1.61	2.80	44.0	43.5	21.8	27.9	0.79	0.76
15X-1, 116	120.16	2.02	1.47	2.82	54.1	51.2	27.4	37.7	1.18	1.04
15X-2, 100	121.50	1.78	1.31	2.80	45.6	49.6	26.3	35.7	0.84	0.98
15X-3, 38	122.38	1.91	1.33	2.71	56.4	53.7	30.2	43.4	1.29	1.15
15X-4, 64	124.14	1.91	1.36	2.75	53.7	52.3	28.8	40.4	1.16	1.09
15X-5, 56	125.56	2.02	1.52	2.84	48.2	47.5	24.5	32.4	0.93	0.90
16X-3, 10	132.00	1.88	1.31	2.85	55.5	54.9	30.2	43.3	1.25	1.21
16X-2, 9	130.49	1.93	1.40	2.89	52.1	52.0	27.6	38.1	1.09	1.07
16X-4, 53	133.93	1.95	1.40	2.74	53.7	51.5	28.2	39.3	1.16	1.05
17X-1, 72	139.42	2.01	1.46	2.73	53.8	50.5	27.5	37.9	1.16	1.01
17X-1, 128	139.98	1.90	1.31	2.79	57.6	55.4	31.1	45.1	1.36	1.23
17X-CC, 3	141.16	1.93	1.35	2.88	57.1	55.3	30.3	43.4	1.33	1.22
18X-1, 73	149.23	2.02	1.49	2.85	52.0	50.1	26.4	35.8	1.08	1.00
18X-2, 30	150.30	1.89	1.34	2.81	53.6	53.1	29.0	40.9	1.15	1.12
18X-4, 70	153.70	1.98	1.49	2.79	47.8	47.4	24.7	32.8	0.92	0.89
21X-1, 12	170.32	1.87	1.29	2.83	56.8	55.8	31.1	45.2	1.32	1.25
21X-2, 90	172.60	1.95	1.42	2.79	51.4	50.5	27.0	37.1	1.06	1.01
22X-1, 46	180.36	2.02	1.53	2.63	47.6	45.3	24.2	31.9	0.91	0.82

Table 16 (continued).

Core, section, interval (cm)	Depth (mbsf)	Wet-bulk density (g/cm ³)	Dry-bulk density (g/cm ³)	Grain density (g/cm ³)	Wet porosity (%)	Dry porosity (%)	Wet-water content (%)	Dry-water content (%)	Wet void ratio	Dry void ratio
141-861C- (cont.)										
22X-5, -40	186.30	1.95	1.44	2.75	49.4	48.7	26.0	35.0	0.98	0.94
22X-5, 54	186.44	2.48	2.20	2.89	27.2	27.2	11.2	12.7	0.37	0.36
22X-3, 125	184.15	2.02	1.49	2.78	51.6	49.3	26.2	35.4	1.07	0.96
24X-1, 58	209.00	2.09	1.66	2.80	42.1	41.7	20.6	25.9	0.73	0.71
25X-1, 58	209.48	2.11	1.69	2.82	40.8	40.7	19.8	24.7	0.69	0.68
25X-2, 79	211.19	2.05	1.56	2.79	47.8	46.3	23.9	31.4	0.92	0.85
25X-3, 108	212.98	2.03	1.54	2.80	47.7	46.6	24.1	31.7	0.91	0.86
27X-1, 79	220.89	2.05	1.56	2.75	47.8	45.9	23.9	31.4	0.92	0.84
27X-2, 22	221.82	2.07	1.60	2.69	46.3	44.0	22.9	29.7	0.86	0.78
27X-3, 36	222.97	2.05	1.53	2.66	50.0	46.7	25.0	33.4	1.00	0.87
27X-5, 80	225.81	2.15	1.71	2.82	43.7	42.1	20.8	26.2	0.78	0.72
28X-1, 97	229.07	1.99	1.49	2.74	48.4	47.3	24.9	33.2	0.94	0.89
28X-3, 64	231.74	2.03	1.57	2.74	45.1	44.2	22.7	29.4	0.82	0.79
28X-4, 64	233.24	2.05	1.58	2.68	46.0	44.1	23.0	29.9	0.85	0.78
28X-5, 44	234.18	2.13	1.69	2.71	42.6	40.7	20.5	25.8	0.74	0.68
29X-1, 66	238.36	2.08	1.66	2.71	41.0	40.3	20.1	25.2	0.69	0.67
31X-1, 15	248.45	2.06	1.61	2.76	43.8	43.1	21.8	27.9	0.78	0.75
31X-2, 100	250.80	2.10	1.66	2.68	42.1	40.6	20.6	25.9	0.73	0.68
31X-3, 67	251.97	2.15	1.72	2.65	41.6	39.3	19.9	24.8	0.71	0.64
32X-1, 108	258.08	2.09	1.65	2.70	42.5	41.2	20.8	26.3	0.74	0.69
32X-2, 58	259.08	2.15	1.74	2.75	39.9	38.8	19.0	23.5	0.66	0.63
33X-1, 82	267.42	1.98	1.48	2.74	48.4	47.4	25.1	33.4	0.94	0.89
33X-2, 54	268.64	1.99	1.51	2.71	47.2	46.2	24.3	32.1	0.89	0.85
34X-2, 50	276.95	2.13	1.69	2.87	43.2	42.6	20.8	26.3	0.76	0.74
34X-3, 78	278.23	2.15	1.69	2.88	44.7	43.5	21.3	27.1	0.81	0.76
34X-4, 24	278.51	2.14	1.68	2.81	45.0	43.2	21.5	27.5	0.82	0.75
34X-6, 108	282.35	2.29	1.88	2.69	40.1	36.7	17.9	21.8	0.67	0.57
35X-1, 30	286.20	2.14	1.71	2.82	41.7	40.9	20.0	25.0	0.72	0.69
35X-3, 67	288.70	2.15	1.72	2.79	42.6	41.1	20.3	25.4	0.74	0.69
35X-4, 52	290.05	2.00	1.61	2.75	38.7	40.1	19.8	24.7	0.63	0.66
36X-1, 24	295.84	2.14	1.74	2.53	38.3	35.9	18.4	22.5	0.62	0.56
36X-2, 90	298.00	2.17	1.75	2.79	41.7	40.2	19.6	24.5	0.71	0.67
36X-4, 24	300.34	2.23	1.80	2.86	42.0	40.2	19.3	23.9	0.72	0.67
37X-1, 12	305.02	2.11	1.65	2.78	44.6	43.1	21.7	27.7	0.80	0.75
37X-2, 65	307.05	2.12	1.72	2.77	38.9	38.7	18.8	23.2	0.64	0.63
38X-CC, 15	314.65	2.11	1.69	2.70	41.3	39.9	20.0	25.0	0.70	0.66
25X-4, 52	213.92	2.04	1.53	2.74	49.1	46.9	24.7	32.8	0.96	0.88
39X-1, 41	324.61	2.18	1.76	4.09	40.6	48.7	19.1	23.6	0.68	0.94
39X-2, 36	326.06	2.10	1.66	2.78	42.5	41.8	20.8	26.2	0.74	0.71
39X-3, 60	326.92	2.15	1.73	2.80	41.4	40.4	19.7	24.6	0.71	0.67
40X-1, 100	334.90	2.06	1.62	2.72	43.1	42.2	21.4	27.3	0.76	0.72
40X-3, 100	337.90	2.10	1.66	2.74	42.7	41.5	20.8	26.3	0.74	0.70
40X-6, 100	340.42	2.13	1.70	2.65	41.4	39.4	20.0	24.9	0.71	0.65
41X-1, 72	344.12	2.14	1.73	2.71	40.7	39.1	19.4	24.1	0.69	0.64
41X-2, 60	345.50	2.23	1.87	2.75	35.7	34.6	16.4	19.6	0.55	0.53
41X-4, 30	348.20	2.18	1.77	2.77	40.1	38.8	18.8	23.2	0.67	0.63
41-861D-										
1R-2, 32	344.12	2.15	1.71	2.80	43.5	41.9	20.7	26.1	0.77	0.71
1R-3, 50	345.80	2.30	1.92	2.92	37.6	36.7	16.8	20.1	0.60	0.57
2R-1, 17	352.07	2.21	1.85	2.83	35.1	35.1	16.3	19.4	0.54	0.54
2R-2, 88	354.28	2.25	1.82	3.02	41.9	41.2	19.1	23.6	0.72	0.70
2R-2, 12	353.52	2.18	1.78	2.77	39.6	38.3	18.6	22.8	0.66	0.62
6R-1, 50	390.90	2.18	1.79	2.78	37.5	37.0	17.6	21.4	0.60	0.58
6R-3, 130	393.20	2.34	1.96	2.84	37.1	35.2	16.3	19.4	0.59	0.54
6R-2, 40	391.67	2.18	1.79	2.75	38.0	37.1	17.9	21.8	0.61	0.58
7R-1, 132	401.42	2.10	1.81	2.82	28.3	30.8	13.8	16.0	0.40	0.44
7R-2, 50	402.10	2.21	1.81	2.73	39.5	37.5	18.3	22.3	0.65	0.60
7R-3, 104	403.99	2.23	1.80	2.68	42.2	38.8	19.4	24.1	0.73	0.63
8R-1, 66	410.46	2.12	1.71	2.71	39.9	39.0	19.3	23.9	0.66	0.63
9R-1, 104	420.44	2.14	1.74	2.72	39.9	38.7	19.1	23.6	0.66	0.63
9R-2, 11	420.96	2.24	1.86	2.79	36.9	35.8	16.9	20.3	0.59	0.55
9R-3, 43	422.78	2.13	1.74	2.71	38.2	37.4	18.3	22.4	0.62	0.59
10R-1, 25	429.35	2.24	1.87	2.75	35.5	34.4	16.2	19.4	0.55	0.52
10R-1, 125	430.35	2.20	1.81	2.72	38.3	36.9	17.9	21.8	0.62	0.58
11R-1, 49	439.29	2.23	1.88	2.75	34.0	33.4	15.6	18.5	0.52	0.50
11R-2, 100	441.00	2.32	2.00	2.80	31.8	31.0	14.0	16.3	0.47	0.45
13R-12, 10	458.20	2.16	1.77	2.66	38.6	37.0	18.3	22.4	0.63	0.58
13R-2, 66	460.26	2.19	1.80	2.78	38.2	37.2	17.8	21.7	0.62	0.59
13R-3, 90	461.43	2.26	1.86	2.79	38.5	36.8	17.5	21.1	0.63	0.58
14R-1, 2	467.72	2.16	1.75	2.77	40.0	38.9	18.9	23.4	0.67	0.63
14R-CC, 1	468.87	2.21	1.82	2.79	37.8	36.8	17.5	21.2	0.61	0.58
15R-1, 27	476.57	2.22	1.82	2.71	39.8	37.5	18.3	22.5	0.66	0.59
15R-2, 66	477.96	2.25	1.85	2.73	39.5	37.1	18.0	21.9	0.65	0.59
16R-1, 17	486.17	2.19	1.80	2.76	38.3	37.2	17.9	21.8	0.62	0.59
16R-2, 44	487.94	2.19	1.78	2.78	40.5	39.0	18.9	23.3	0.68	0.63
16R-3, 63	488.78	2.10	1.66	2.72	43.3	41.7	21.1	26.8	0.76	0.71

Table 17. Acoustic velocity (V_p) of discrete sediment samples from Holes 861C and 861D measured with the Hamilton Frame velocimeter.

Core, section, interval (cm)	Depth (mbsf)	Velocity (m/s)
141-861C-		
4H-2, 116-120	24.70	1570
4H-5, 107-112	29.07	1550
84H-5, 108-112	29.08	1577
10H-1, 47-52	71.47	1526
22X-5, 55-56	186.45	3650
31X-2, 60-64	250.40	1909
32X-1, 106-108	258.06	1914
38X-CC, 10-12	314.60	2004
40X-1, 92-93	334.82	1792
41X-2, 17-19	345.07	1816
141-861D-		
1R-1, 133-134	343.63	1870
13R-3, 88-90	461.41	2281
14R-1, 34-36	468.04	2140
16R-3, 30-32	488.45	2450

Note: The four determinations for samples above 72 mbsf were measured on easily crumbled sediment confined in a small plastic box. The velocity determined for each sample appears to be lower than the likely in-situ value.

Table 18. Thermal conductivity measurements for Holes 861A, 861B, 861C, and 861D.

Core, section, interval (cm)	Depth (mbsf)	Thermal conductivity (W/m-K)
141-861A-		
1H-1, 95	0.95	1.56
1H-4, 43	4.93	1.29
141-861B-		
1H-1, 97	0.97	1.11
1H-4, 97	5.47	1.21
141-861C-		
1H-1, 100	1.00	1.08
1H-2, 100	2.50	1.15
2H-1, 100	4.00	1.32
2H-4, 100	8.50	1.18
3H-1, 100	13.50	1.01
3H-4, 100	18.00	0.90
3H-6, 100	21.00	0.97
4H-1, 100	23.00	1.31
4H-4, 100	27.50	0.99
4H-7, 15	31.15	1.06
5H-2, 100	32.80	0.79
5H-6, 100	38.80	1.18
6H-2, 70	43.20	1.12
6H-6, 70	49.20	1.20
7H-2, 123	53.23	1.07
7H-6, 90	58.90	1.07
8H-2, 100	62.50	1.14
8H-6, 100	68.50	1.12
10H-1, 92	71.92	1.19
10H-4, 100	76.50	1.19
12X-1, 100	91.10	1.11
13X-1, 57	100.37	1.25
14X-1, 100	110.40	1.16
15X-1, 75	119.75	1.01
15X-4, 100	124.50	1.13
16X-1, 100	129.90	0.99
16X-4, 100	134.40	1.16
17X-1, 75	139.45	0.95
17X-2, 50	140.70	1.26
18X-1, 100	149.50	1.07
18X-4, 75	153.75	1.24
21X-2, 80	172.50	1.30
22X-6, 38	187.78	1.00
22X-CC, 10	188.47	0.99
25X-2, 63	211.03	1.30
25X-4, 48	213.88	1.24
28X-4, 60	233.20	1.06
32X-2, 15	258.65	1.56
33X-CC, 17	269.61	1.50
40X-2, 80	336.20	1.26
141-861D-		
1R-3, 13	345.43	1.32

assess the consequences of the conductivity variations on the accuracy of our temperature determinations. Where applicable for a particular point, we have averaged the various temperature estimates for an individual ADARA run obtained using the two thermal conductivities and the different sections of the temperature decay curves. The error estimate given in Table 19 is then the greatest observed departure above and below this average temperature.

The ADARA deployment at 22 mbsf is characterized by an initially noisy penetration record but has a relatively good subsequent temperature decay curve (Fig. 47). The decay curve is split into two regions by a minor period of tool disturbance. We used the APCTFIT program to analyze the two sections marked *X* and *Y* in Figure 47. The extrapolated formation temperatures for section *X* are then 4.84° and 4.99°C using 1.1 and 1.2 W/m-K, respectively. For section *Y*, the formation temperatures are 5.68° and 5.72°C using 1.1 and 1.2 W/m-K, respectively. The average estimated formation temperature at this depth is then 5.31°±0.41°C. As we can see, the error introduced by the different thermal conductivities is generally much less than the error arising from fitting the different portions of the temperature decay curve.

The ADARA measurement at 31.5 mbsf is noisy (Fig. 48), and we fit only one portion of the temperature decay curve. The extrapolated temperatures are then 5.68° and 5.71°C using 1.1 and 1.2 W/m-K, respectively. This gives an average temperature of 5.70°±0.02°C. Note that, as the data are fitted over a short interval, we consider this measurement to be of only moderate quality, despite having a relatively low apparent error estimate.

The ADARA measurement at 41 mbsf is again noisy, and we fit two portions of the temperature decay curve, marked *X* and *Y* in Figure 49. From portion *X*, the extrapolated temperatures are 6.91° and 7.00°C using 1.1 and 1.2 W/m-K, respectively. From portion *Y*, the extrapolated temperatures are 7.17° and 7.21°C using 1.1 and 1.2 W/m-K, respectively. This gives an average formation temperature of 7.07°±0.14°C for this depth, but because of tool disturbance this point is considered to be of only moderate quality.

The ADARA deployment at 60 mbsf has a good decay profile with an initial temperature spike and an extraction spike (Fig. 50). The extrapolated temperatures are 7.63° and 7.62°C using thermal conductivities of 1.1 and 1.2 W/m-K, respectively. This gives an average formation temperature of 7.625°±0.005°C for this depth.

The ADARA deployment at 80.5 mbsf (Fig. 51) again has a good decay profile (with some minor noise at the end of the decay sequence). The extrapolated temperatures are 8.61° and 8.50°C using thermal conductivities of 1.1 and 1.2 W/m-K, respectively. This gives an average formation temperature of 8.55°±0.05°C.

In general, we consider the reliability of the temperature estimates from the three upper ADARA deployments to be relatively low because they have noisy, disturbed temperature decay profiles. In contrast, the ADARA deployments at 60 and 80.5 mbsf are good, and we expect the errors to be low and their reliability to be high.

Discussion

All the results for the WSTP and ADARA deployments are summarized in Table 19 and the most reliable are plotted against sub-bottom depth on Figure 52. The thermal gradient appears to be almost linear through much of the upper 250 m of the hole with the exception of the section from 0 to 60 mbsf where there is a higher gradient. This is consistent with a conductive mechanism being the dominant mode of heat transport at this site.

The ADARA and WSTP temperature measurements appear to be slightly shifted from each other in the subsurface portion of the hole. For example, the two well-constrained ADARA measure-

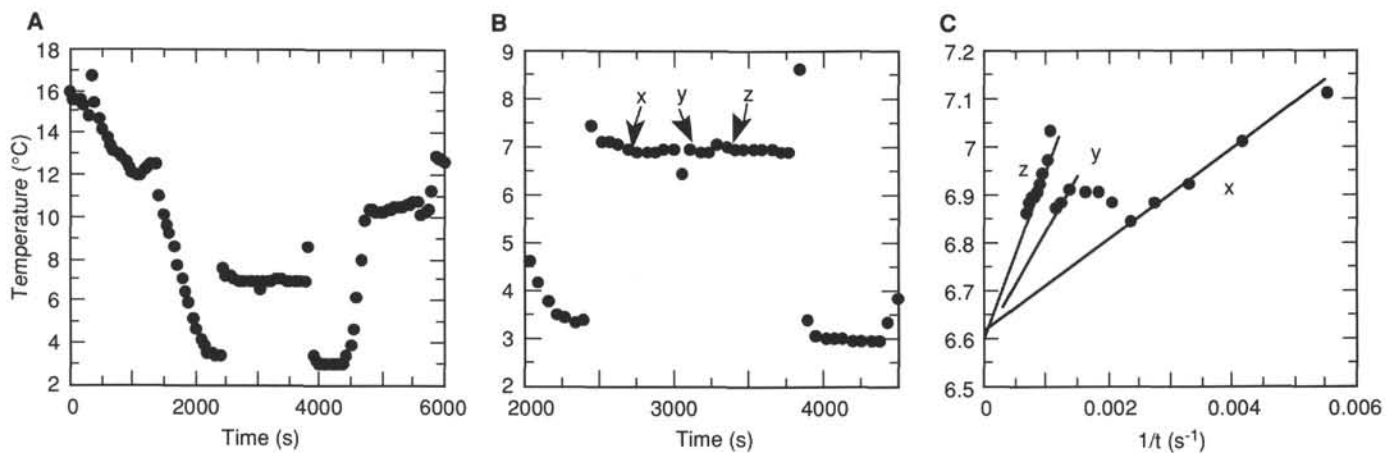


Figure 43. Results from WSTP deployment (new probe) at 50.5 mbsf. The penetration record (A and B) is noisy, but when plotted in $1/t$ space (C) several linear trends from the disturbed sections (X, Y, and Z, in B) extrapolate to close to the same temperature, $6.61^{\circ}\pm 0.02^{\circ}\text{C}$.

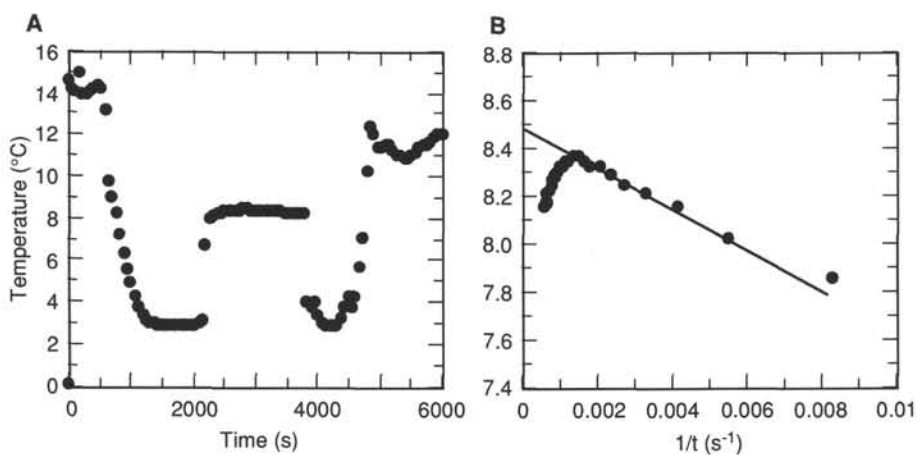


Figure 44. Results from WSTP deployment (old probe) at 90.1 mbsf (A). There is a pronounced data hook at low $1/t$ values (B). The linear trend extrapolates to $8.47^{\circ}\pm 0.03^{\circ}\text{C}$.

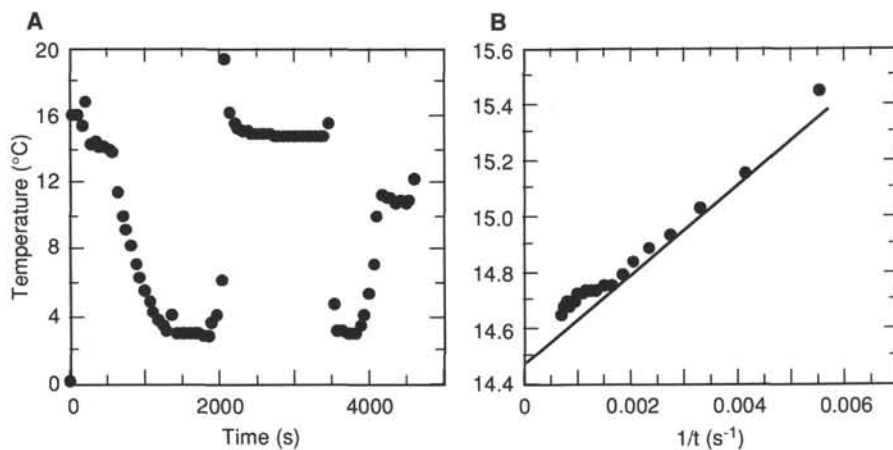


Figure 45. Results from WSTP deployment (old probe) at 189.6 mbsf (A). There is a small data hook at low $1/t$ values (B). The linear trend extrapolates to $14.48^{\circ}\pm 0.03^{\circ}\text{C}$.

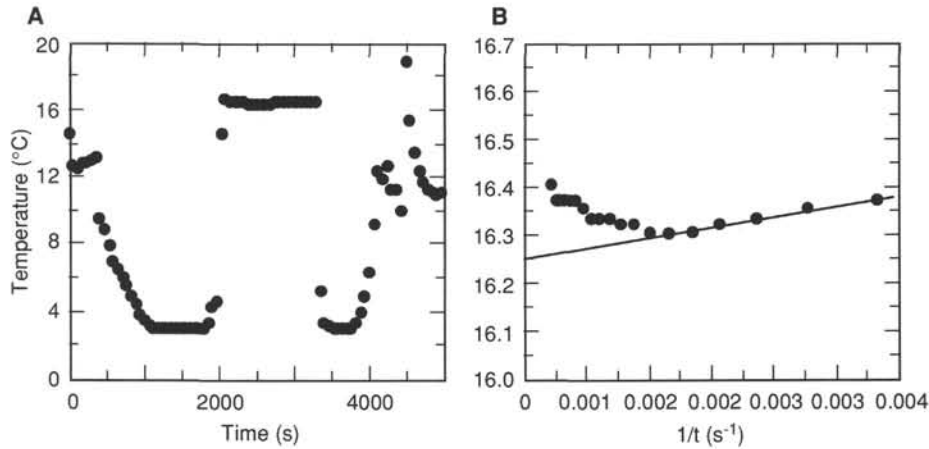


Figure 46. Results from WSTP deployment (old probe) at 228.1 mbsf (A). There is a pronounced data hook at low $1/t$ values (B). The linear trend extrapolates to $16.25 \pm 0.01^\circ\text{C}$.

Table 19. Temperature data for Site 861.

Depth (mbsf)	Adara temperature (°C)	WSTP temperature (°C)	Error (±)
0.0	2.40	2.70	
22.0	5.31		0.41*
31.5	6.027		0.06*
41.0	7.073		0.25*
50.5		6.61	0.02*
60.0	7.622		0.005
80.5	8.55		0.06
90.1		8.47	0.03
189.6		14.48	0.03
228.1		16.25	0.01

*Poor quality data

Measurements at 60 and 80 mbsf are 0.3° to 0.5°C higher than expected temperatures from the local WSTP determinations (Fig. 52). This causes a slight problem in determining the exact geothermal gradient. The two tools read similar bottom-water temperatures (with the ADARA tool actually recording slightly cooler temperatures than the WSTP tool) and thus it is not a basic calibration problem. We suspect the simplified geometrical basis for the theoretical decay functions used in the APCTFIT program may not be correctly simulating the relatively complex geometry of the

ADARA tool, leading to a slight ($<0.5^\circ\text{C}$) overestimate of the formation temperature.

The upper, poorer-quality ADARA measurements between 0 and 60 mbsf are only used to estimate where the near-surface inflection point is. The lower geothermal gradient at Site 861 is $56^\circ\text{C}/\text{km}$, increasing to approximately $110^\circ\text{C}/\text{km}$ in the near-surface (Fig. 52). The poor-quality measurements near the surface are all on the warmer side of the linear extrapolation, the significance of which is not fully understood at this point. Using these observed temperatures and the latest Claypool (G.E. Claypool, pers comm., 1992) equation for the methane hydrate stability field, the theoretical position of any methane-hydrate-related BSR at this site should be close to 265 mbsf. The local BSR on the seismic reflection section is approximately at 225 mbsf if we assume an average seismic velocity of 1.8 km/s for the upper-slope sediment section. Thus, we have a significant discordance between the theoretical position of the BSR and the observed position on seismic reflection sections. Indeed, for the observed BSR position and the theoretical position of the BSR to match, the average seismic velocity of the slope sediments would have to be in the region of 2.1 km/s, which is unreasonably high for this shallow depth interval. As the determined temperatures clearly constrain the geothermal gradient to be less than $56^\circ\text{C}/\text{km}$, we are led to suggest that either the theoretical basis for the prediction of methane stability is slightly flawed, or that the BSR

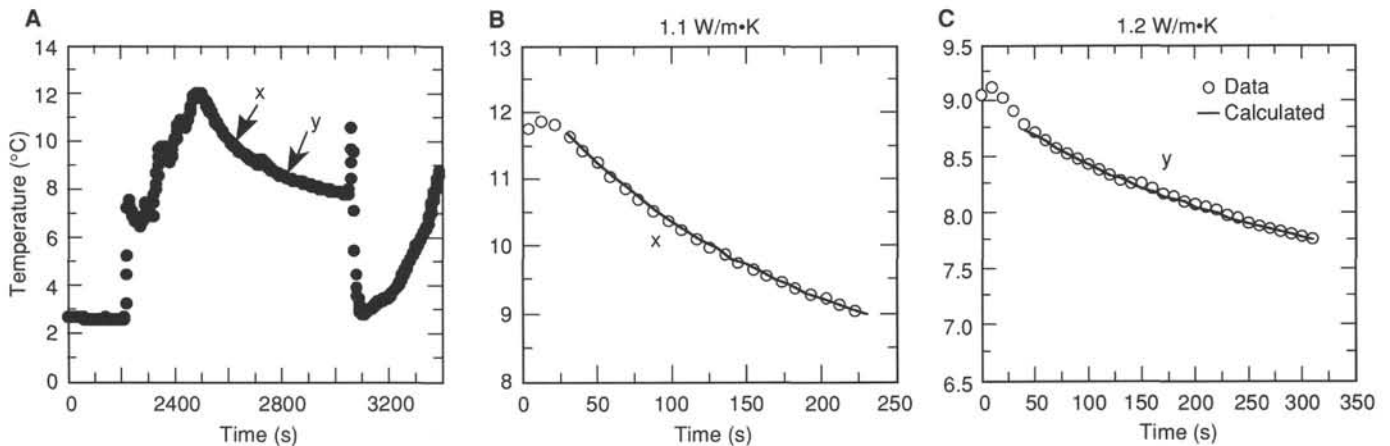


Figure 47. ADARA deployment at 22 mbsf has a slightly disturbed temperature decay profile (A). The two portions of the decay curve (X and Y) are shown fitted (B and C). Both portions of the curve were fitted using thermal conductivities of 1.1 and 1.2 $\text{W}/\text{m}\cdot\text{K}$.

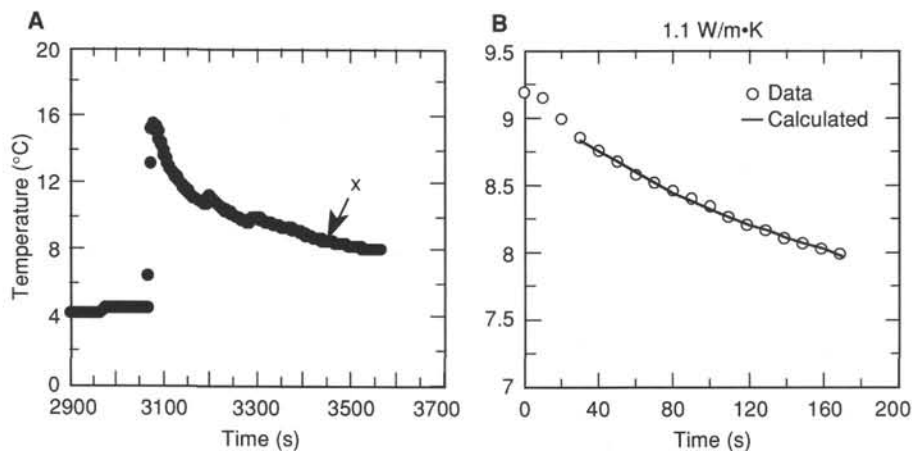


Figure 48. ADARA deployment at 31.5 mbsf has a moderately disturbed temperature decay profile (A). The lower portion of the decay curve (X) is shown fitted (B). The curve was fitted using thermal conductivities of 1.1 and 1.2 W/m·K.

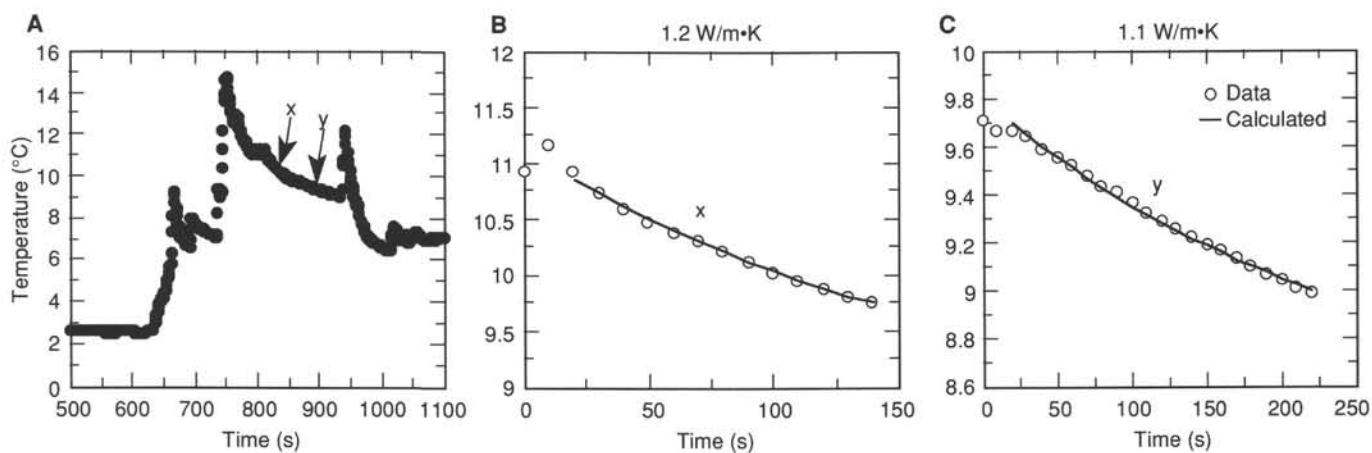


Figure 49. ADARA deployment at 41 mbsf has a moderately disturbed temperature decay profile (A). The two portions of the decay curve (X and Y) are shown fitted (B and C). Both portions of the curve were fitted using thermal conductivities of 1.1 and 1.2 W/m·K. Due to the disturbance, this point is only of moderate quality.

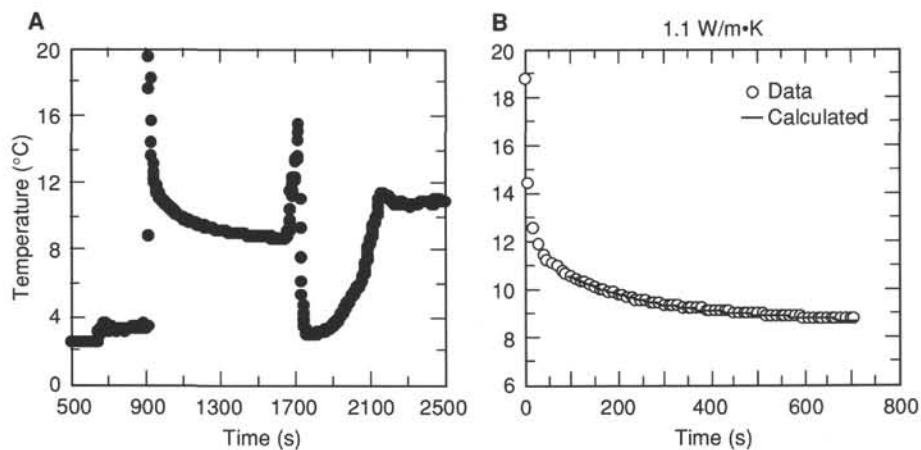


Figure 50. ADARA deployment at 60 mbsf has good temperature decay profile (A). The decay curve was fitted using thermal conductivities of 1.1 and 1.2 W/m·K (B).

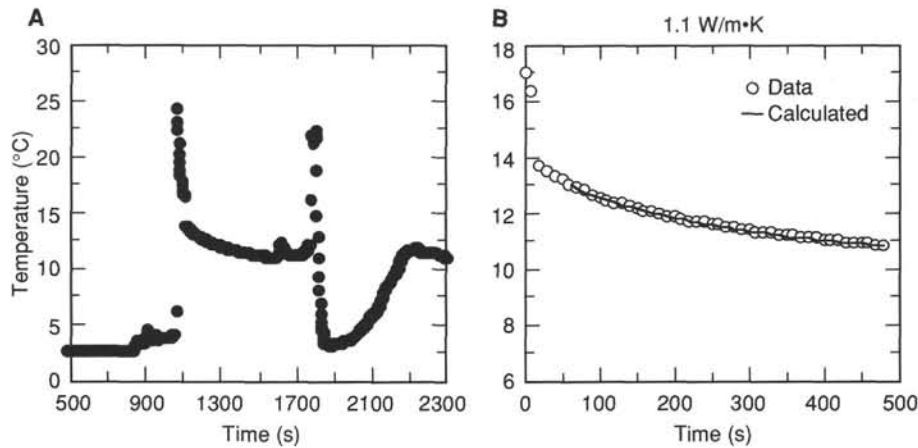


Figure 51. ADARA deployment at 80.5 mbsf has good temperature decay profile (A). The decay curve was fitted using thermal conductivities of 1.1 and 1.2 W/m·K (B).

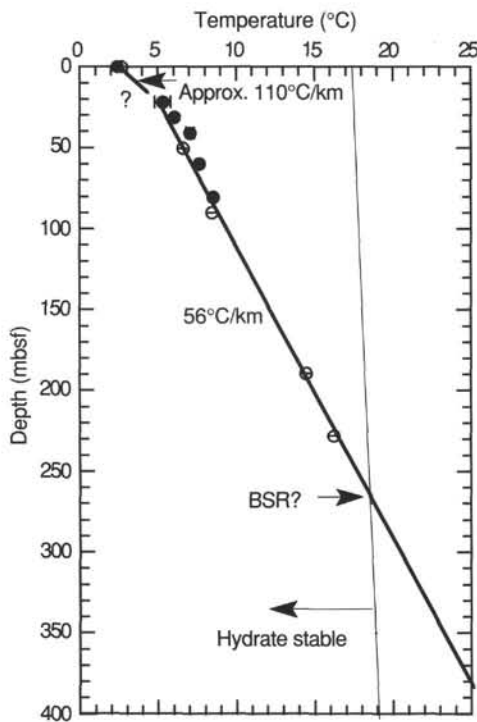


Figure 52. Temperature vs. depth at Site 861. Results from the WSTP (open circles) and ADARA (closed circles) are both shown. In general, the error bars are within the circles of the WSTP measurements. The linear geothermal gradient is drawn favoring the better-constrained WSTP measurements and the best two lower ADARA measurements (at 60 and 80 mbsf). The upper ADARA measurements are, however, used to estimate the approximate position of the near-surface inflection point in the profile. Only the most reliable data are used in the plot.

at this site relates to something other than the base of the pure methane plus seawater hydrate field at stable equilibrium position

SUMMARY AND CONCLUSIONS

Age and Lithology of Sediments

The biostratigraphic age of the sediments cored at Site 861 is Pleistocene to late Pliocene (Fig. 53). The Pliocene/Pleistocene boundary was located at about 168 mbsf. The upper 120 mbsf are

tentatively attributed to the upper Pleistocene, although some uncertainty remains about the exact location of the lower Pleistocene/upper Pleistocene boundary due to conflicting age evidence from diatom, radiolarian, foraminifer, and nannofossil chronostratigraphy. The lower Pleistocene ranges from 120 to 168 mbsf. A reliable correlation between biostratigraphic ages and magnetostratigraphic data based on polarity reversals cannot be made. From 168 mbsf to total depth (496.3 mbsf) there is an apparently continuous upper Pliocene biostratigraphic section.

The lithostratigraphic description of the sediment cored at Site 861 allows a division into three principal lithologic units (Fig. 54). Lithologic Unit I (0–43.8 mbsf) is composed of clayey silts and silty clays with some nannofossil content. Apart from the normal suite of clayey silts and silty clays, lithologic Unit II (43.8–351.9 mbsf) contains an abundance of coarser clastic sediments, notably graded and non-graded silts and sands, intercalations of intraformational gravels, and mud-supported conglomerates. Lithologic Unit II has been divided into Subunits IIA and IIB, mainly on the basis of different degrees of induration of the sediment. The boundary is somewhat gradational, but for the purpose of nomenclature it has been drawn at 208.9 mbsf. In the physical properties data the Subunit IIA/IIB boundary shows up only as a minor break in porosity and wet-water content (Fig. 42).

In the fluid and gas chemistry record, however, major changes are recorded across the Subunit IIA/IIB boundary. The contents of dissolved Ca and Sr show breaks or minima at about 200 mbsf.

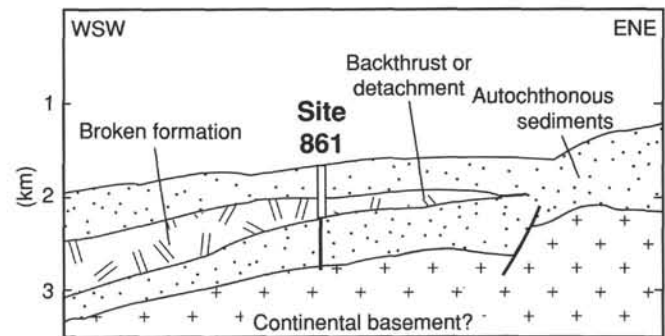


Figure 53. Interpretive tectonic cross section of the surroundings of Site 861, based on the information given in Figure 3. The tectonic contact at the base of the broken formation could have the nature of either a backthrust or a detachment.

Together with the observation that contents of these elements throughout most of the sequence are significantly lower than in seawater (Fig. 39), this can be interpreted as reflecting the removal of Ca and Sr from the interstitial fluid to build up intergranular cement of micritic calcite. A thin micritic limestone stringer found at about 190 mbsf might in part be the expression of a "diagenetic front" associated with this process, and explain the Ca and Sr minima at 200 mbsf. In Subunit IIB it was observed that part or all of the calcareous microfossils were recrystallized to form micritic calcite. It is also important to note that the hydrocarbon gases change composition at about 215 mbsf. There is a marked decrease in C_1/C_2 ratio here in both headspace and vacutainer analyses, which is interpreted to reflect a downward change from biogenic to more thermogenic gas source contributions. While not being an efficient cap rock for hydrocarbons, it is conceivable that the Subunit IIA/IIB boundary acts as a permeability barrier for the upward migrating thermogenic hydrocarbons. At first sight this is not in line with the notion of downward-increasing degree of cementation and reduction in pore space, but note that only below 210 mbsf are the rocks fractured (see Fig. 22), and so possess an associated fracture permeability that may be orders of magnitude higher than that of structurally intact mud or silt. Lithologic Unit III (351.9–496.3 mbsf) is a uniform suite of silty claystone to clayey siltstone with some intervals showing a very distal turbidite signature.

Depositional History and Paleobathymetry

As at Sites 859 and 860, the sediment at Site 861 is of glacial-marine origin. The composition suggests a mixed provenance of volcanic-arc-derived and crystalline-basement-derived materials. They were probably first deposited as gravitationally unstable deposits on or near the shelf edge (see discussion in the Lithostratigraphy section, this chapter), and then detached as slumps and slides and displaced oceanward as massive debris flows and other gravity flows. The proximal expression of this depositional environment is essentially one of conglomerates, sands, and silts. The distal expression is fine-grained turbidites and laminated silts and clays, formed from the caps of turbulently suspended sediment above the debris flows. According to this interpretation, Subunits IIB and IIA would represent proximal and intermediate facies, whereas Units I and III would be distal to extremely distal facies.

Summarizing the paleobathymetric estimates that can be inferred from benthic foraminifers found in cores at Site 861, it can be said that the section from 0 to 139 mbsf was deposited in the upper to middle bathyal depth range. The occurrence of *Boliviana costata* in this part of the section may be taken to indicate that the water depth was not in excess of 2000 m. Below 139 mbsf to terminal depth, deposition was in the middle bathyal to abyssal range with the abyssal water ecotype *Melonis ompilioides sphaeroides* occurring at 323 mbsf. It appears that an important phase of uplift is recorded by the lower Pleistocene sediment section around 140 mbsf.

Where is the Continental Basement?

One of the initial objectives of drilling at Site 861 was to verify the hypothesis that the landward region of the trench slope on the Site 859 to Site 861 transect was underlain by the Southern Andes continental basement. For the reasons outlined in the Operations section of this site chapter, this goal was not achieved. However, there are a few clues from the inorganic geochemical analysis of fluids and the gas geochemistry concerning the nature and possible depth of basement. It is one of the remarkable results of interstitial fluid analysis that the sodium and chloride concentrations are higher than seawater level throughout, and show a steady downhole increase to 115%–120% of seawater (see Fig. 39). The

undisturbed, approximately linear downhole temperature increase (see below) makes it unlikely that large amounts of fluid are transported through the section laterally, and the variations in the composition of the interstitial fluids are therefore probably best interpreted as representing vertical diffusion gradients on a scale larger than the depth of the borehole. Using such an interpretation, a source of high salinity must exist at depth to explain the downhole increases in Na and Cl. An evaporite or shabka source of such brines (cf. Suess, von Huene, et al., 1988), as inferred for the parts of the Peru continental margin drilled during Leg 112, is unlikely in this part of the Chile margin, so that metamorphic or magmatic rocks at depth and their associated hydrothermal systems (e.g., Roedder, 1972) are the likely source of the hypersaline fluid. There are linear downhole decreases in Mg and K (Fig. 39). If these distributions are also taken as diffusion profiles and extrapolated in a linear fashion, zero contents of Mg and K are expected at a depth of about 1000 mbsf at Site 861. This leads us to speculate that there may be a Mg and K sink at this depth. One possible scenario for crystalline basement reactions involving Mg and K uptake at temperatures of anchizonal (very low-grade) metamorphism (constrained by depth extrapolation of downhole temperatures at Site 861) is the sericitization of plagioclase feldspar and chloritization of biotite. Together with quartz these two minerals are the major constituents of the landward continental basement (e.g., Miller, 1970a, 1970b), and it is not unreasonable to infer from our observations that such basement extends as far seaward as Site 861.

On the other hand, the recognition of "broken formation" (see Structural Geology section, this chapter; Fig. 22) and its structural similarity to the broken formation found at Sites 859 and 860 clearly argues against there being a simple and autochthonous sequence of sediments at Site 861. Whereas the Pleistocene and upper Pliocene sediments down to a depth of 350 mbsf (lithologic Units I and II) can be interpreted as autochthonous cover deposited on an unstable upper to middle trench slope (initial sedimentation at lower bathyal, later at middle to upper bathyal, water depths) rather proximal to the sediment source, the broken formation is an abyssal to lower bathyal, distal hemipelagic deposit either sedimented on a lower trench slope or deposited seaward of the trench and scraped off oceanic crust. In view of this evidence, one possible tectonic model for the immediate vicinity of Site 861 includes an allochthonous broken formation floored by a backthrust, as part of the seaward-extending Pliocene accretionary prism (Fig. 54). The footwall of this thrust is made up of a Neogene and pre-Neogene autochthonous sediment cover and continental basement. Alternatively, a seaward movement of the broken formation on a detachment surface located at the same position as the backthrust is conceivable. In this scenario the broken formation at Site 861 would reflect deformation "en masse" of a large submarine slide detached during vigorous uplift of the part of the trench slope floored by continental basement.

The data discussed here can only be used to advance these hypotheses. Renewed and deeper drilling is needed, first to prove or disprove the existence of a backthrust or detachment at the base of the broken accretionary wedge strata, and second to verify the nature of the deep (800–1200 mbsf) seismic reflectors at Site 861.

Where are the Gas Hydrates?

Unlike Site 859, the part of the section with potentially stable gas hydrate at Site 861 does not show any anomaly of interstitial water and WSTP water chemistry that can be related to hydrate dissociation (see discussion in the Inorganic Chemistry section, this chapter, and Fig. 40). According to the downhole temperature profile (Fig. 52), methane hydrate should be stable at this site to a depth of 265 mbsf. Hydrates are probably not present in the

subsurface at Site 861, and the BSR that was identified at 200 mbsf (see Background and Objectives section, this chapter) has to be interpreted in an alternative fashion. The increase in degree of diagenesis identified at around 208 mbsf at the boundary of Subunits IIA and IIB (see discussion above) is a likely candidate for the acoustic impedance contrast shown in the seismic section at this depth. While there may be a gas-hydrate-related BSR farther updip and downdip (see Fig. 3), strong evidence exists from the drilling that gas hydrates do not occur in the sediment in the immediate vicinity of Site 861.

Thermal Structure of the Middle Trench Slope

Downhole temperature measurements with the WSTP and ADARA tools (Fig. 52) yielded a well-constrained linear geothermal gradient of 56°C/km for the section between 20 and 228.1 mbsf. Between the mudline and 20 mbsf the temperature gradient is 110°C/km. Based on the linear geothermal gradient of 56°C/km, a simple calculation yields a conductive heat-flow estimate of about 67 mW/m² for the interval from 20–228.1 mbsf. For the calculation a bulk thermal conductivity of 1.2 W/m·K was used (compare Fig. 42). Site 861 is at present underlain by subducting oceanic crust about 0.8 Ma old. Typically, oceanic crust of this age has mean heat flows between 150 mW/m² (East Pacific Rise) and 200 mW/m² (Galapagos spreading center; data from Anderson and Hobart, 1976). If the 67 mW/m² value is in any way representative for the conductive heat transport through the middle trench slope of the overriding South American Plate, then a major discrepancy exists between the amount of heat transferred through the oceanic crustal layer at depth and the amount of heat passing through the crust-ocean interface upslope in the accretionary wedge. We suspect that the difference between the two estimates represents the fraction of heat removed from the system by lateral advective fluid flow through the accretionary wedge.

The near-surface increase of the geothermal gradient is likely to be a disturbance caused by localized fluid flow. An inspection of Figure 39 shows small but distinct highs in Na and Cl, and lows in Ca and Sr at or around 20 mbsf. This is interpreted to relate to temperate water of elevated salinity escaping from the formation toward the seawater in a zone of enhanced fluid flow. Similar near-surface phenomena have been observed before at Sites 674 and 676 near the toe of the Barbados accretionary prism (see Mascle, Moore, et al., 1988, pp. 427, 531). In our case this observation can be taken as evidence of active fluid discharge from the upper-slope cover strata to the oceanic water column.

REFERENCES

- Anderson, J.B., 1983. Glacial-marine sediment in space and time. In Molnia, B.F. (Ed.), *Glacial-Marine Sedimentation*: New York (Plenum), 3–92.
- Anderson, R.N., and Hobart, M.A., 1976. The relation between heat flow, sediment thickness and age in the Eastern Pacific. *J. Geophys. Res.*, 81:2968–2989.
- Bé, A.W.H., and Tolderlund, D.S., 1971. Distribution and ecology of living planktonic foraminifera in surface waters of the Atlantic and Indian Oceans. In Funnell, B.M., and Riedel, W.R. (Eds.), *The Micropaleontology of Oceans*: Cambridge (Cambridge Univ. Press), 105–149.
- Boersma, A., 1984. *Handbook of Common Tertiary Uvigerina*: Stony Point, NY (Microclimate Press).
- Borradaile, G.J., 1981. Particulate flow of rock and the formation of cleavage. *Tectonophysics*, 72:305–321.
- Burckle, L.H., 1977. Pliocene and Pleistocene diatom datum levels from the equatorial Pacific. *Quat. Res.*, 7:330–340.
- Claypool, G.E., and Kaplan, I.R., 1974. The origin and distribution of methane in marine sediments. In Kaplan, I.R. (Ed.), *Natural Gases in Marine Sediments*: New York (Plenum), 99–139.
- Didyk, B.M., and Simoneit, B.R.T., 1989. Hydrothermal oil of Guaymas Basin and implications for petroleum formation mechanisms. *Nature*, 342:65–68.
- Didyk, B.M., Simoneit, B.R.T., Brassell, S.C., and Eglinton, G., 1978. Organic geochemical indicators of palaeoenvironmental conditions of sedimentation. *Nature*, 272:216–222.
- Drewry, D., 1986. *Glacial Geologic Processes*: London (Edward Arnold).
- Emeis, K.C., and Kvenvolden, K.A., 1986. Shipboard organic geochemistry on JOIDES Resolution. *ODP Tech. Note*, 7.
- Espitalié, J., Madec, M., Tissot, B., Menning, J.J., and Leplat, P., 1977. Source rock characterization method for petroleum exploration. *Proc. 9th Ann. Offshore Technol. Conf.*, 3:439–448.
- Farrington, J.W., Davis, A.C., Tarafa, M.E., McCaffery, M.A., Whelan, J.K., and Hunt, J.M., 1988. Bitumen molecular maturity parameters in the Ikpikpuk well, Alaskan North Slope. *Org. Geochem.*, 13:303–310.
- Mapa Geológico de Chile, 1980. *Carta Geol. Chile*, 52527 (scale 1:1,000,000).
- Mascle, A., Moore, J.C., et al., 1988. *Proc. ODP, Init. Repts.*, 110: College Station, TX (Ocean Drilling Program).
- Miall, A.D., 1983. Glaciomarine sedimentation in the Gowganda Formation (Huronian), northern Ontario. *J. Sediment. Petrol.*, 53:477–491.
- , 1985. Sedimentation on an early Proterozoic continental margin under glacial influence: the Gowganda Formation (Huronian), Elliott Lake area, Ontario, Canada. *Sedimentology*, 32:763–788.
- Miller, H., 1970a. Das Problem des hypothetischen “Pazifischen Kontinentes” gesehen von der chilenischen Pazifikküste. *Geol. Rundsch.*, 59:927–938.
- , 1970b. Vergleichende Studien an prämesozoischen Gesteinen Chiles unter besonderer Berücksichtigung ihrer Kleintektonik. *Geotekt. Forsch.*, 36:1–64.
- Molnia, B.F., 1983. Subarctic glacial-marine sedimentation: a model. In Molnia, B.F. (Ed.), *Glacial-Marine Sedimentation*: New York (Plenum), 95–144.
- Nigrini, C., 1991. Composition and biostratigraphy of radiolarian assemblages from an area of upwelling (northwestern Arabian Sea, Leg 117). In Prell, W.L., Niitsuma, N., et al., *Proc. ODP, Sci. Results*, 117: College Station, TX (Ocean Drilling Program), 89–126.
- Rabassa, J., and Clapperton, C.M., 1990. Quarternary glaciations of the southern Andes. *Quat. Sci. Rev.*, 9:153–174.
- Resig, J.M., 1990. Benthic foraminiferal stratigraphy and paleoenvironments off Peru. In Suess, E., von Huene, R. et al., *Proc. ODP, Sci. Results*, 112: College Station, TX (Ocean Drilling Program), 263–296.
- Roedder, E., 1972. Composition of fluid inclusions. *Data of Geochemistry*. Geol. Surv. Prof. Pap. U.S., 400-JJ.
- Rutland, R.W.R., 1971. Andean orogeny and ocean floor spreading. *Nature*, 233:252–255.
- Shipboard Scientific Party, 1982. Guaymas Basin: Sites 477, 478, and 481. In Curray, J.R., Moore, D.G., et al., *Init. Repts. DSDP*, 64 (Pt. 1): Washington (U.S. Govt. Printing Office), 210–415.
- Simoneit, B.R.T., 1977. Diterpenoid compounds and other lipids in deep-sea sediments and their geochemical significance. *Geochim. Cosmochim. Acta*, 41:463–476.
- , 1978. The organic chemistry of marine sediments. In Riley, J.P., and Chester, R. (Eds.), *Chemical Oceanography* (2nd ed.) (Vol. 7): New York (Academic Press), 233–311.
- Simoneit, B.R.T., Brenner, S., Peters, K.E., and Kaplan, I.R., 1981. Thermal alteration of Cretaceous black shale by basaltic intrusions in the eastern Atlantic. II: effects on bitumen and kerogen. *Geochim. Cosmochim. Acta*, 45:1581–1602.
- Suess, E., von Huene, R., et al., 1988. *Proc. ODP, Init. Repts.*, 112: College Station, TX (Ocean Drilling Program).
- van Morkhoven, F.P.C.M., Berggren, W.A., and Edwards, A.S., 1986. Cenozoic cosmopolitan deep-water benthic foraminifera. *Bull. Cent. Rech. Explor.-Prod. Elf-Aquitaine*, 11:1–421.

- Vinogradov, U.N., 1981. Glacier erosion and sedimentation in the volcanic regions of Kamchatka. *Ann. Glaciol.*, 2:164-169.
- von Huene, R., and Lallemand, S., 1990. Tectonic erosion along the Japan and Peru convergent margins. *Geol. Soc. Am. Bull.*, 102:704-720.
- von Huene, R., and Scholl, D.W., 1991. Observations at convergent margins concerning sediment subduction, subduction erosion, and the growth of continental crust. *Rev. Geophys.*, 29:279-316.
- Wright, R., and Anderson, J.B., 1982. The importance of sediment gravity flow to sediment transport and sorting in a glacial-marine environment: Weddell Sea, Antarctica. *Geol. Soc. Am. Bull.*, 93:951-963.
- Wright, R., Anderson, J.B., and Fisco, P.P., 1983. Glacial-marine sediment in space and time. In Molnia, B.F. (Ed.), *Glacial-Marine Sedimentation*: New York (Plenum), 3-92.

Ms 1411R-108

NOTE: For all sites drilled, core-description forms ("barrel sheets") and core photographs have been reproduced on coated paper and can be found in Section 3, beginning on page 449. Forms containing smear-slide data can be found in Section 4, beginning on page 665.

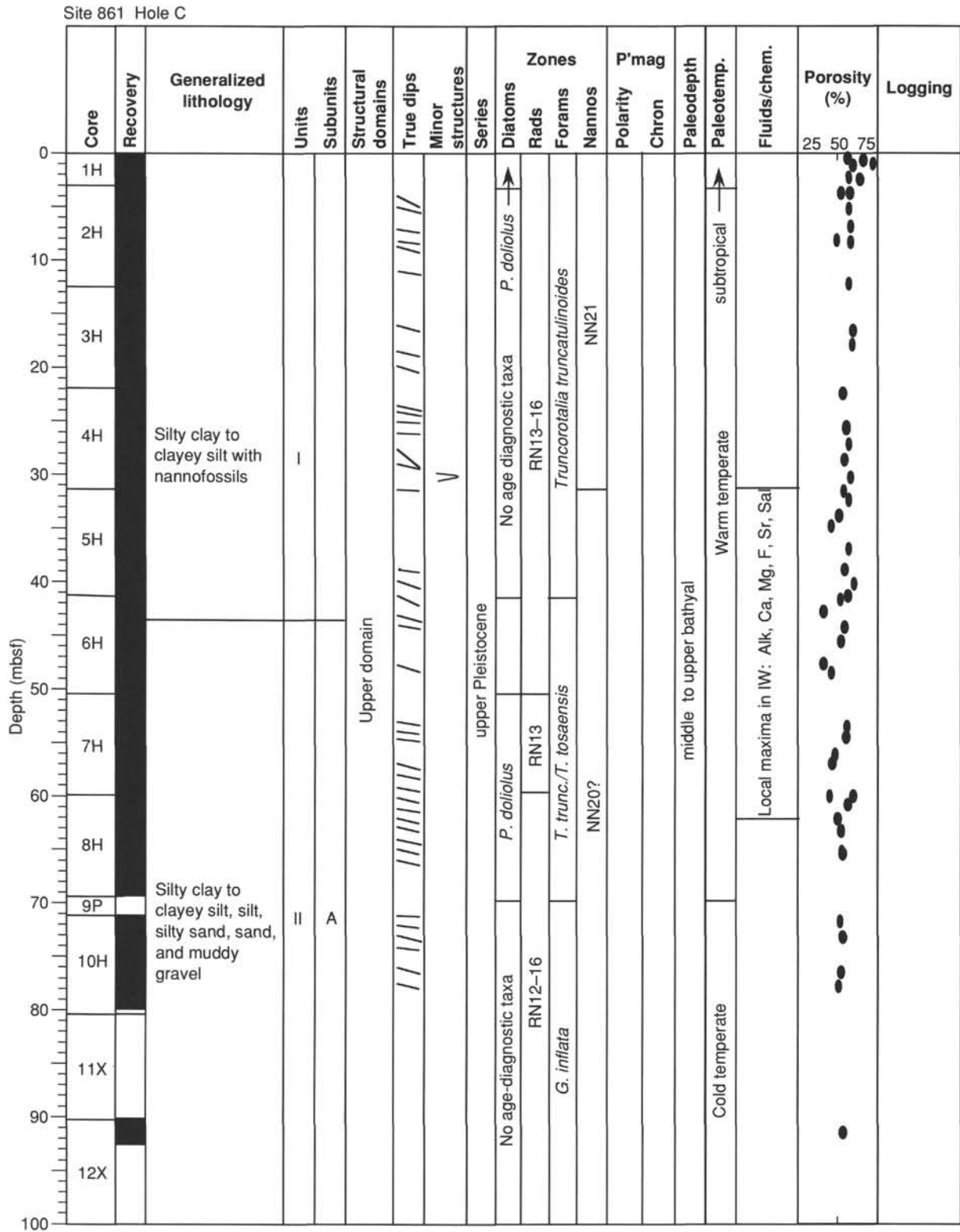


Figure 54. Master chart for Site 861.

Site 861 Hole C (continued)

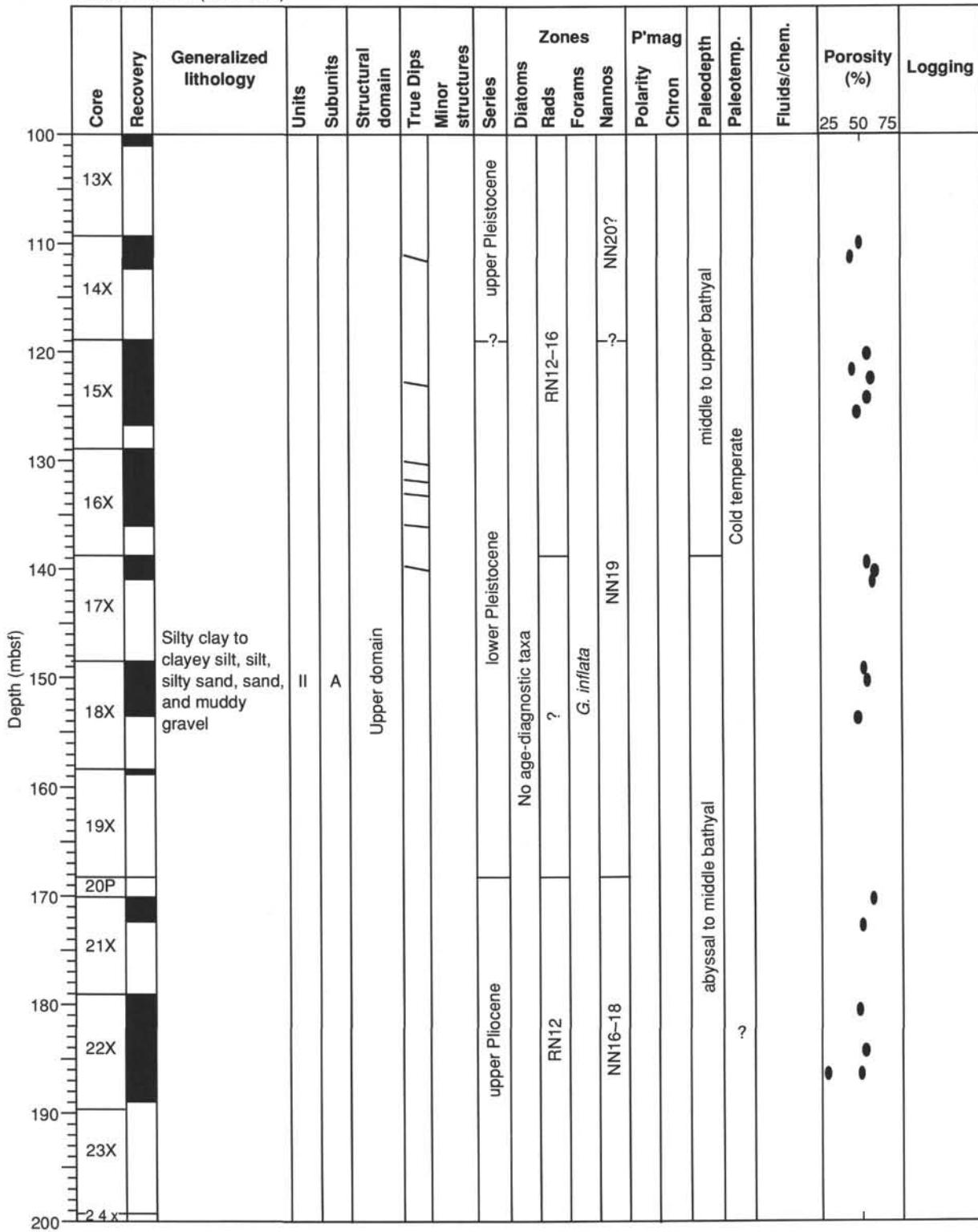


Figure 54. (Continued).

Site 861 Hole C (continued)

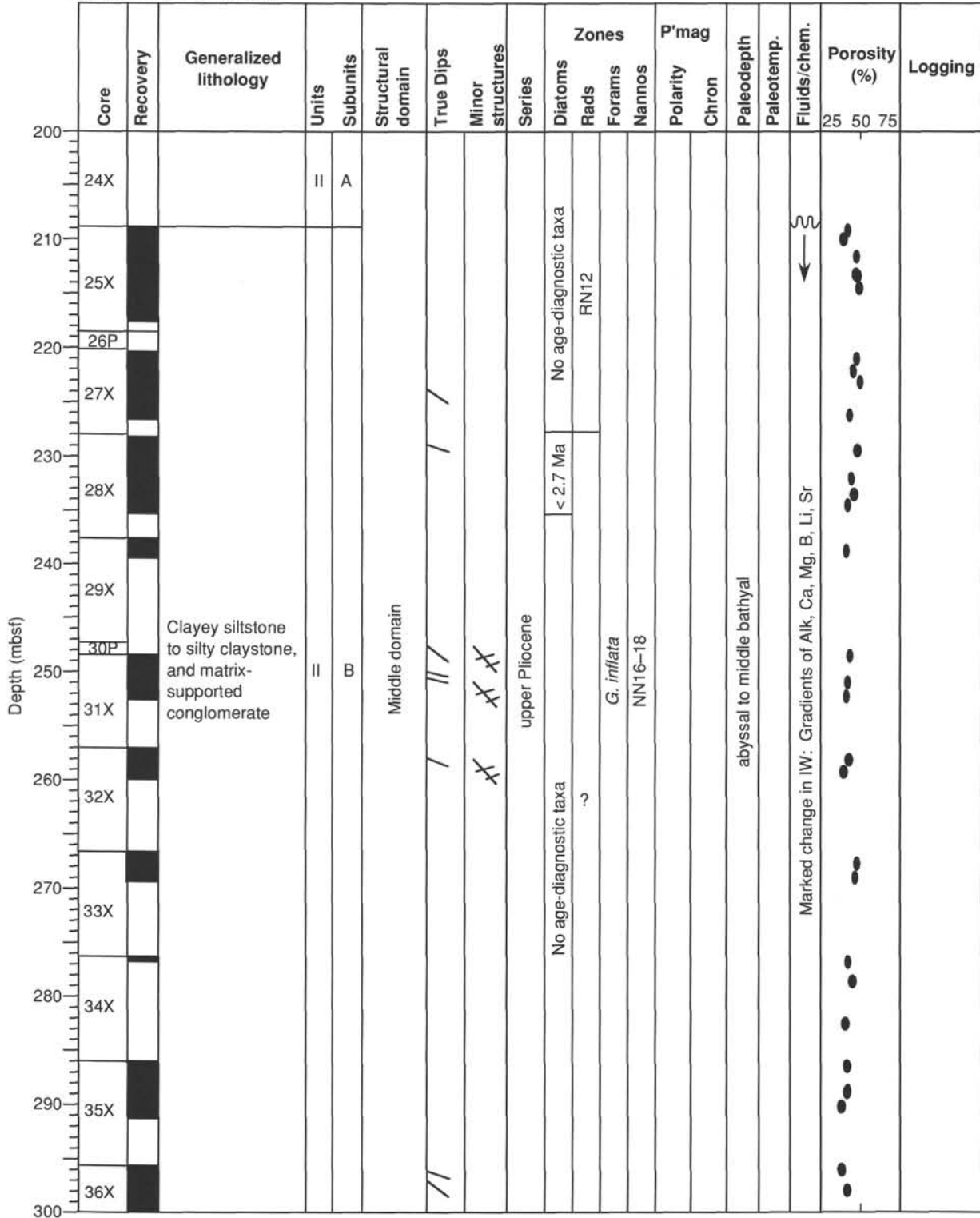
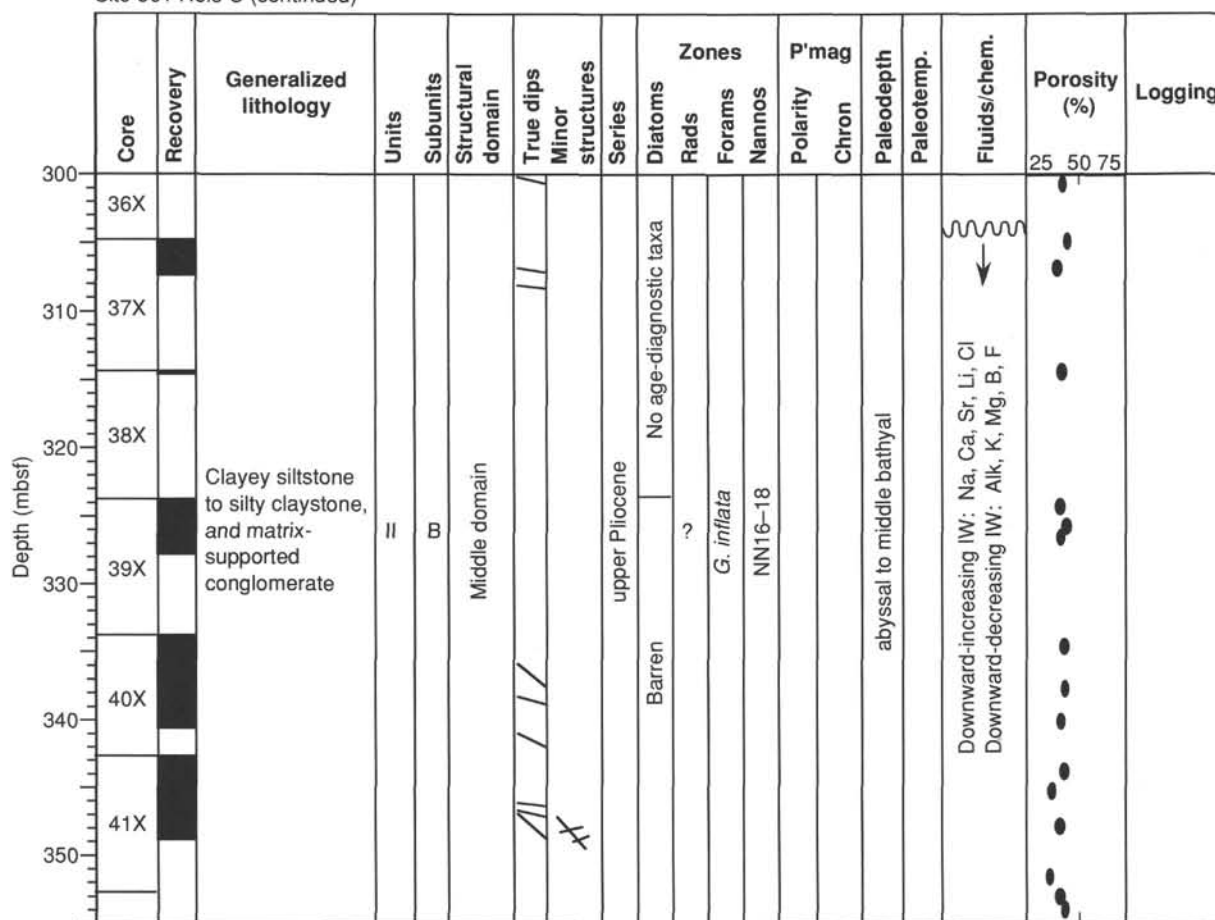


Figure 54. (Continued).

Site 861 Hole C (continued)



- Folds: drawn in orientation observed in core
- Clastic vein
- Fault/tectonic contact
- Normal fault
- Deformation bands in clays or claystones. True dips here refer to the deformation bands.
- Isolated deformation band in silt/siltstone or sand/sandstone.
- Deformation bands in silt/siltstone or sand/sandstone.
- Fracture cleavages: True dips refer to cleavage orientation
- Jointing
- Breccia
- Calcite veins

- B = Barren
- Tropical radiolarian zones (After Sanfilippo et al., 1985)
- RN16 = *Buccinosphaera invaginata*
- RN15 = *Collosphaera tuberosa*
- RN14 = *Amphirhopalum ypsilon*
- RN13 = *Anthocyrtdium angulare*
- RN12 = *Pterocanium prismatium*
- RN11 = *Spongaster pentas*
- RN10 = *Stichocorys peregrina*
- Paleomagnetic polarity
- Normal
- Mixed polarity
- Reversed
- No cryogenic measurement

Unless otherwise indicated, true dips refer to bedding

Figure 54. (Continued).

Site 861 Hole D

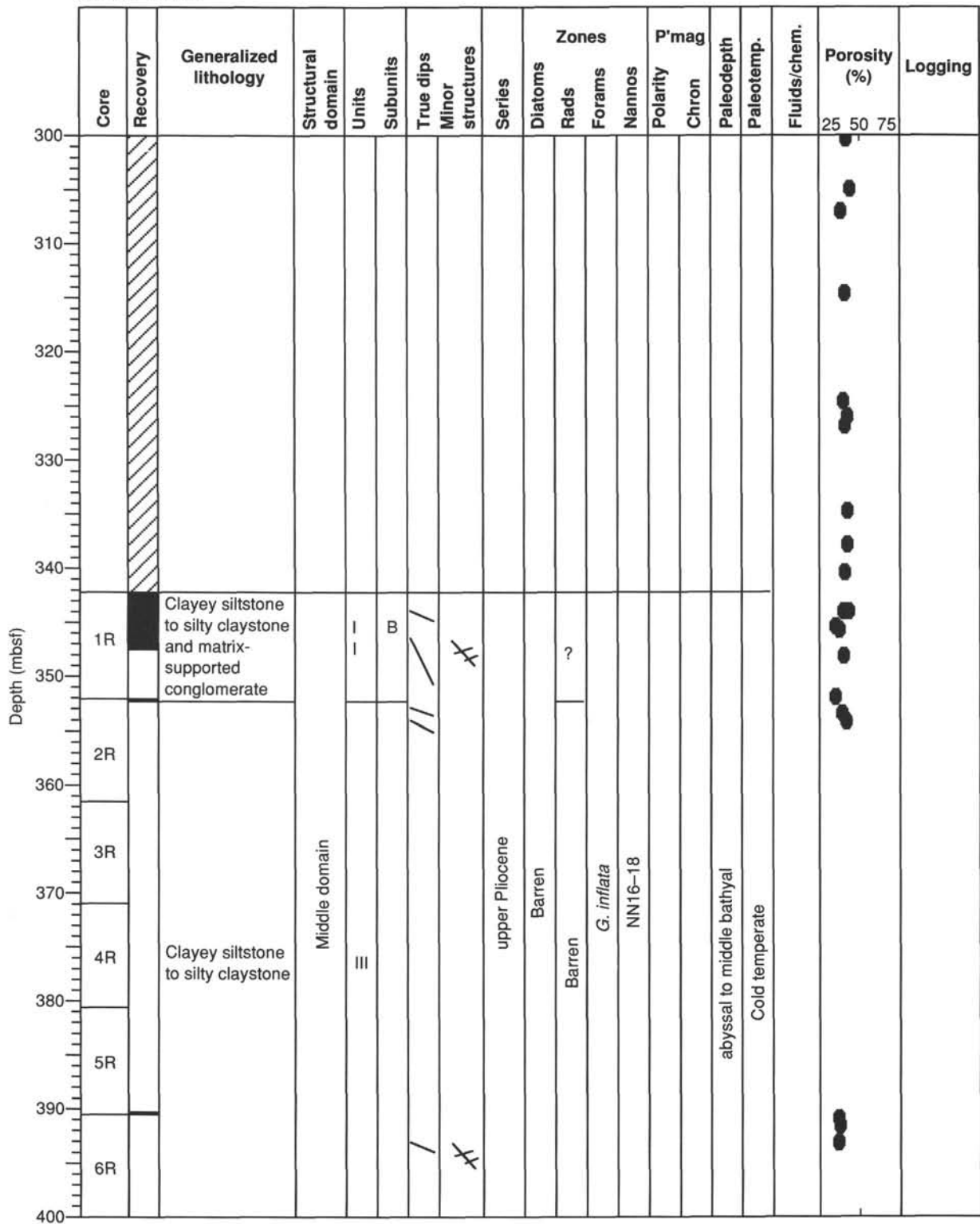


Figure 54. (Continued).

Site 861 Hole D (continued)

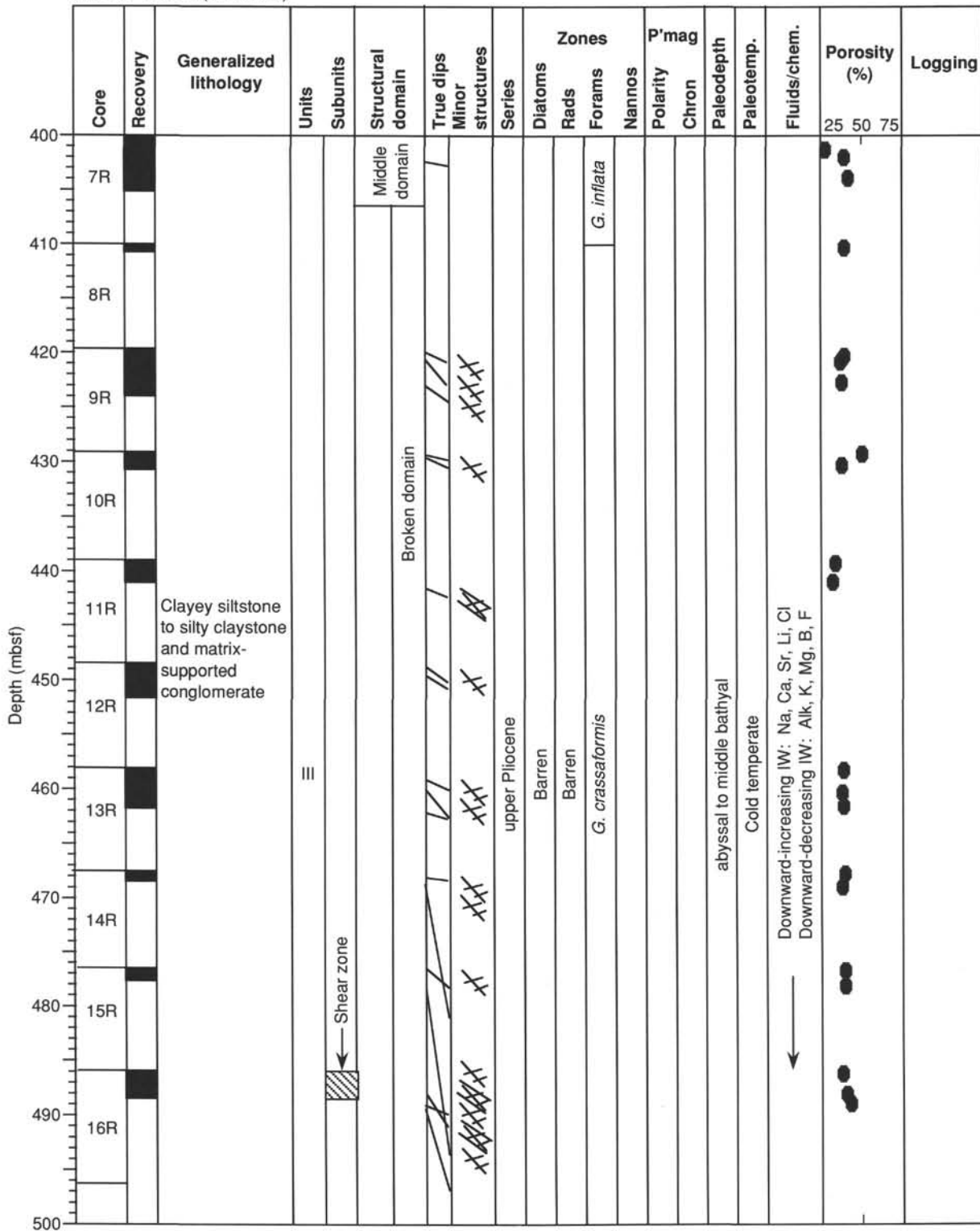


Figure 54. (Continued).